

**Upper Tropospheric Ozone Enhancement during the North
American Monsoon evaluated using the Weather Research
and Forecasting Model with Chemistry (WRF-Chem)**

by

J. Wong

M.S., University of Colorado, 2010

M.A., University of Arkansas, 2007

B.S., University of Arkansas, 2006

A thesis submitted to the

Faculty of the Graduate School of the

University of Colorado in partial fulfillment

of the requirements for the degree of

Doctor of Philosophy

Department of Atmospheric and Oceanic Sciences

2013

This thesis entitled:
Upper Tropospheric Ozone Enhancement during the North American Monsoon evaluated using
the Weather Research and Forecasting Model with Chemistry (WRF-Chem)
written by J. Wong
has been approved for the Department of Atmospheric and Oceanic Sciences

Dr. David Noone

Dr. Mary Barth

Date _____

The final copy of this thesis has been examined by the signatories, and we find that both the content and the form meet acceptable presentation standards of scholarly work in the above mentioned discipline.

Wong, J. (Ph.D., Atmospheric and Oceanic Sciences)

Upper Tropospheric Ozone Enhancement during the North American Monsoon evaluated using the Weather Research and Forecasting Model with Chemistry (WRF-Chem)

Thesis directed by Dr. David Noone

Upper tropospheric ozone has significant impacts on the total atmospheric chemistry and radiative budget. Previous studies noted an upper tropospheric ozone enhancement above southern United States during the North American Monsoon (NAM). This recurring phenomenon has been observed by the satellite-borne Tropospheric Emission Spectrometer (TES) and IONS-06 ozonesondes. Using the Weather Research and Forecasting model with Chemistry (WRF-Chem), we attempt to simulate the ozone enhancement and understand the underlying structure, chemical pathways, and sensitivity to emissions.

Using a modified lightning parameterization based on the Price and Rind scheme, a July-August simulation is performed using WRF-Chem. Validation shows that flash rate is overpredicted by a factor of 10, which subsequently causes an overestimation of O_3 . Despite the amplified ozone enhancement, boundary layer and stratospheric tracers do not show substantial differences within and outside the anticyclone, contrary to what has been predicted in other studies. On the other hand, lightning tracers, lateral boundary tracers, tracer-tracer correlations, and chemistry pathways can be used to distinguish between the anticyclone and the surrounding area.

Sensitivity and control simulations are also performed to investigate how different emission sources contribute to the ozone enhancement. It is shown that lightning emission enhances NO_x superlinearly, which leads to NO_x -titration in the upper troposphere. On the other hand, anthropogenic emission is shown to modify the ozone concentration and chemistry profiles via sensitivity to VOC, and biogenic emission affects ozone via sensitivity to NO_x . As a result of the changes in ozone mixing ratio profile, convective tendency is also affected, which forms a nonlinear feedback between chemistry and convection in response to perturbation in emissions.

Acknowledgements

First and foremost, I would like to thank Dr. Mary Barth (NCAR/ACD) and Dr. David Noone (CIRES/ATOC) for providing the opportunities and exceptional guidance throughout my graduate study at University of Colorado at Boulder. This work was supported by the NASA Atmospheric Composition program (grant number NNH07AM47G) and appointment via the NRCM project (NSF-EaSM grant AGS-1048829; “Developing a Next-Generation Approach to Regional Climate Prediction at High Resolution”). TheNLDN dataset is provided by Vaisala and made available via Dr. James Crawford of NASA Langley Research Center and Dr. Owen Cooper at NOAA/ESRL. The ENTLN dataset is prepared and provided by Steve Prinzivall at Earth Networks. We would like to acknowledge high-performance computing support provided by NCAR’s Computational and Information Systems Laboratory, sponsored by the National Science Foundation (project code P35071370). We also thank the following individuals who have provided valuable advices and insights in relation to this study and assistance in developing the diagnostics and lightning parameterization modules for WRF-Chem: Dr. Linnea Avallone (LASP/ATOC), Dr. Georg Grell (NOAA/ESRL/GSD), Dr. Sasha Madronich (NCAR/ACD), Dr. David Noone (CIRES/ATOC), Dr. Steven Peckham (NOAA/ESRL/GSD), Dr. Gabriele Pfister (NCAR/ACD), Dr. Bill Skamarock (NCAR/MMM), Dr. John Worden (NASA/JPL). Finally, I would like to acknowledge and thank Dr. Tom Warner (NCAR/RAL, CU-Boulder/ATOC) for his support before he passed away on May 30, 2011.

Contents

Chapter

1	Introduction	1
1.1	Tropospheric ozone chemistry	3
1.1.1	Sources for Volatile organic compounds (VOCs)	4
1.1.2	Anthropogenic sources for Nitrogen oxides (ANO _x)	7
1.2	Parameterizing Lightning-generated NO _x (LNO _x)	8
1.2.1	Overview of lightning physics	9
1.2.2	Flash rate parameterization	10
1.2.3	Lightning-generated NO _x	14
1.3	Summary	16
2	Lightning parameterization	18
2.1	Methods	20
2.1.1	Parameterization overview	20
2.1.2	Model setup and implementation	22
2.1.3	Data description	25
2.2	Results and discussions	27
2.2.1	Precipitation	27
2.2.2	CG flash rate	31
2.2.3	IC:CG ratio	34

2.3	Resolution dependency	35
2.3.1	Sensitivity to grid size	37
2.3.2	Sensitivity to formulation	38
2.4	Conclusions	40
2.5	Comments on cloud-top height reduction	42
3	2006 North American Monsoon Case Study	45
3.1	Model description	46
3.1.1	Model options and parameterizations	47
3.1.2	Chemistry and emissions	47
3.1.3	Tendency diagnostics and passive tracers	50
3.2	General results and validation	52
3.2.1	Meteorology	52
3.2.2	Ozone	57
3.2.3	Carbon monoxide	62
3.2.4	Formaldehyde	69
3.2.5	Nitrogen Oxides	73
3.3	Discussion	78
3.3.1	Tracer relations	78
3.3.2	Tendency diagnostics	84
3.4	Sensitivity study	89
3.4.1	Lightning emission	89
3.4.2	Anthropogenic emission	98
3.4.3	Biogenic emission	101
3.5	Conclusions	103
4	Summary	107
4.1	Perspectives and outlook	110

References	112
-------------------	------------

Appendix

A Acronyms and Abbreviations	124
B WRF-Chem v3.4.1 Namelist	128
C User documentation for LNO_x in WRF-Chem 3.5	131
D WRF-Chem bug fixes	134
D.1 Fast TUV	134
D.1.1 Bug description	134
D.1.2 Changes made	135
D.1.3 Other problems	136
D.2 Passive tracer-convective transport	137
D.2.1 Bug description	137
D.2.2 Changes made	137
D.2.3 Other problems	137

Tables

Table

2.1 WRF lightning simulations setups	21
3.1 Examples of NEI-RADM2 speciation mapping	105
3.2 IONS-06 August data usde	106
3.3 Linear regression on NO_2 VCDs	106
D.1 Compaison of photolysis rates from FTUV and TUV.	135

Figures

Figure

1.1	Filtered upper tropospheric ozone from <i>Cooper et al.</i> (2007)	1
1.2	National Emission Inventory (NEI) VOC emission trend	5
1.3	National Emission Inventory (NEI) NO _x emission trend	7
1.4	Illustration of MCS electric charge structure from <i>Stolzenburg et al.</i> (1998)	9
2.1	Domain for lightning simulations	22
2.2	Spatial distribution of JJA total precipitation in 2006 and 2011	26
2.3	Time series and frequency distribution for 2006 and 2011 daily precipitation	28
2.4	Spatial distribution of NLDN and WRF-predicted CG flash counts	30
2.6	CG flashes vs. precipitation	31
2.5	NLDN and WRF CG flash counts	32
2.7	PR92-predicted total lightning as a function of cloud-top	33
2.8	ENTLN and predicted IC:CG bulk ratios	34
2.9	ENTLN and predicted total lightning	36
2.10	Resolution-dependency of lightning prediction	37
2.11	Formulation dependency of lightning prediction	39
3.1	2006 case study model domain	46
3.2	EPA NEI05 NO emission	48
3.3	WRF and NWS July and August precipitation	53

3.4	WRF and NWS precipitation time series	54
3.5	NLDN and WRF CG daily flash count and distribution	55
3.6	Simulated August ozone at 300 hPa	57
3.8	WRF-Chem and TES ozone frequency distributions	58
3.7	TES/WRF-Chem Ozone comparisons	59
3.9	IONS-06 Huntsville launches	62
3.10	Simulated August CO at 300 hPa	63
3.11	WRF-Chem and TES CO frequency distributions	64
3.12	TES/WRF-Chem CO comparisons	66
3.13	WRF and MOPITT CO comparisons	68
3.14	SCIAMACHY and WRF-Chem formaldehyde on 8/18	70
3.15	SCIAMACHY and WRF-Chem formaldehyde on 8/24	72
3.16	WRF-Chem NO _x VMR	74
3.17	WRF-Chem and SCIAMACHY NO ₂ VCDs	77
3.18	CO-O ₃ model correlation	78
3.19	Passive tracers	81
3.21	BL-ST tracer correlation	82
3.20	Passive tracer age	83
3.23	Time series for upper tropospheric tendency diagnostics	85
3.22	Ozone advective tendency	86
3.24	Vertical profiles of decaying tracers and tendency diagnostics	87
3.25	Upper tropospheric sensitivity to lightning	91
3.26	Vertical sensitivity profiles of O ₃ , CO, & NO _x to lightning	93
3.27	Daytime and nighttime chemical tendencies	94
3.28	HO _x radical termination	96
3.29	CO-O ₃ model correlation	97
3.30	Vertical profiles for sensitivity to anthropogenic emission	99

3.31 Spatial distribution of sensitivity to anthropogenic emissions	100
3.32 Vertical profiles for sensitivity to biogenic emission	101

Chapter 1

Introduction

Upper tropospheric ozone has significant impacts on the radiative and chemical budgets of the atmosphere (*Kiehl et al.*, 1999). The global tropospheric ozone burden has seen an increase of 71–130 Tg since the preindustrial period, with much of the uncertainties coming from the estimation of preindustrial emission scenarios for anthropogenic, biomass burning, and lightning sources (*Lamarque et al.*, 2005, and references therein). The radiative forcing resulting from this increase depends strongly on the vertical distribution and is the most sensitive near the tropopause (*Lacis et al.*, 1990). *Gauss et al.* (2006) calculated that the global net radiative forcing resulting from a 7.9–13.8 Dobson units increase in tropospheric ozone (ignoring stratospheric changes) varies between 0.25 and 0.45 W m^{-2} . In particular, several models cited by *Gauss et al.* (2006) as well as *Stevenson et al.* (1998) estimated up to $0.5\text{--}1.1 \text{ W m}^{-2}$ increase over parts of northern mid-latitude regions such as the United States and the Mediterranean region. The ozone increases over these areas are

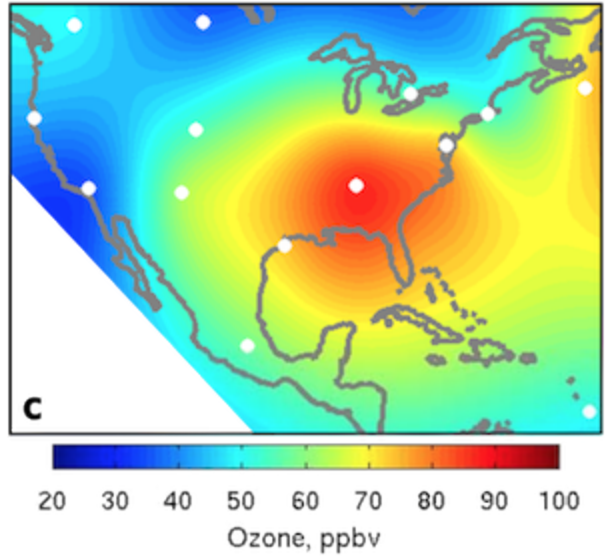


Figure 1.1: **Filtered upper tropospheric ozone from Cooper et al. (2007)** — Interpolated ozonesonde measurements between 10 and 11 km less stratospheric influence estimated using back trajectory (after *Cooper et al.*, 2007, Figure 2c).

also observed by ozonesonde records spanning periods between 1970's and 2004 (*Oltmans et al.*, 2006).

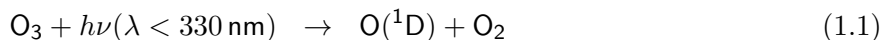
Recent studies have identified monsoonal accumulations of ozone precursors above North America (*Li et al.*, 2005; *Cooper et al.*, 2009, and references therein), Asia (*Park et al.*, 2007; *Worden et al.*, 2009), and equatorial Africa (*Bouarar et al.*, 2011) during summers in the upper troposphere. *Cooper et al.* (2007) calculated a median tropospheric ozone mixing ratio of 87 ppbv (after removing stratospheric intrusion) above Huntsville, AL in August 2006 (Figure 1.1). This is about twice the value measured along the United States west coast during the same period. The observed upper tropospheric ozone enhancement is linked to the North American Monsoon anticyclonic circulation, which traps ozone precursors that subsequently enhance ozone production (*Li et al.*, 2005). *Cooper et al.* (2006) estimated that up to 84% of the enhancement observed above the southern United States can be attributed to *in situ* ozone production from lightning-produced NO_x (LNO_x). The local radiative forcing of this enhancement is +0.50 W m⁻², 70% of which is attributable to enhancement through LNO_x.

By leveraging improved lightning parameterization, online budgeting diagnostics, and passive tracers, this thesis intends to extend the results from previous studies and understand various contributing factors that led to the observed ozone distribution. To understand the processes involved in the NAM upper tropospheric ozone enhancement, the central topic of this thesis, the primary goals of this study are defined as follow:

- (1) Simulate the observed ozone distribution using a regional chemistry transport model and evaluate the outputs against independent observations;
- (2) Utilize online budgeting diagnostics and passive tracers to understand the evolution of the simulated ozone distribution;
- (3) Conduct sensitivity simulations to evaluate how the ozone enhancement would react to different scenarios of anthropogenic, biogenic, and lightning emissions.

1.1 Tropospheric ozone chemistry

Since the primary goals of this study involve diagnosing the simulated ozone values, it is crucial to understand the basis and complexity of tropospheric ozone chemistry. Through its production-destruction cycle, ozone interacts with dozens of chemical species in the troposphere. In the presence of water and shortwave radiation, photodissociation of ozone is also a major precursor for hydroxyl (OH) radicals through the following reactions:



Since OH is the primary oxidizing agent for many volatile organic compounds (VOCs) in the atmosphere, by extension, ozone governs the oxidation capacity of the atmosphere and the lifetime of many trace gases, many of which exclusively originate from anthropogenic and biogenic emissions.

In a dry low-hydrocarbon atmosphere such as the stratosphere, the following reactions determine the steady-state level of ozone:



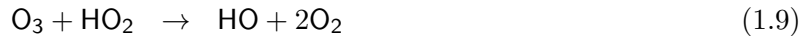
Reaction 1.4 is a termolecular reaction consuming a ground-state oxygen atom produced primarily from photolysis of NO_2 (Reaction 1.3). However, the produced O_3 , or any other ozone molecule in the environment, may react with NO to form NO_2 again (Reaction 1.5). This set of reactions does not destroy or produce ozone molecules, thus it implies a steady-state of ozone, which may be characterized by $[\text{O}_3] \approx (J_{1.3}/k_{1.5})([\text{NO}_2]/[\text{NO}])$, where $J_{1.3}$ is the photolysis rate constant for Reaction 1.3 and $k_{1.5}$ is the rate constant for Reaction 1.5.

In the presence of volatile organic compounds (VOCs) and hydroxyl radicals (OH), however, the reaction set becomes much more complicated. VOCs may be oxidized to produce hydroperoxy radicals (HO_2), e.g. from CO and HCHO , or other peroxy radicals with higher carbon numbers

(RO_2), e.g. methyl peroxy radical (CH_3O_2). These products may then compete with Reaction 1.5 to consume the available NO without the cost of an ozone molecule in the process:



Of course, the produced NO_2 may now proceed to be photolyzed through Reaction 1.3 and perpetuate the ozone cycle. Incidentally, an excess presence of HO_x from the oxidation of VOCs is capable of reducing ozone level through two reactions:



Thus excessive presence of hydrocarbons without sufficient NO to carry out Reactions 1.6 and 1.7 also has the potential of destroying ozone by shortcircuiting the ozone recycling reaction chain.

All the reactions between O_3 , NO_x , HO_x and VOCs result in an ozone level determined by the balance between NO_x and VOCs concentrations as well as photolysis rates. Too much NO_x without sufficient VOCs may cause “ NO_x -titration,” a process which reduces ozone concentration through Reaction 1.5. On the other hand, in an environment with sufficient VOCs but NO_x is scarce, ozone is also destroyed. Thus, for high ozone level to occur (such as in photochemical smogs), compatible levels of both NO_x and VOCs are required. In theory, the variability of ozone concentration in a homogeneously mixed volume may be explained by looking at the ratio between NO_x and VOCs, and identifying the corresponding NO_x -limited and VOC-limited regimes. In practice, transport and mixing complicates such approximation.

1.1.1 Sources for Volatile organic compounds (VOCs)

The definition of volatile organic compounds, or VOCs, varies. For consistency, we use the following definition from the United States Environmental Protection Agency (EPA):

Volatile organic compounds (VOC) means any compound of carbon, excluding carbon monoxide, carbon dioxide, carbonic acid, metallic carbides or carbonates,

and ammonium carbonate, which participates in atmospheric photochemical reactions (EPA, 2012).

The extended definition also explicitly excludes specific chemicals for “negligible photochemical reactivity,” e.g. methane, ethane, CFCs, HCFCs, HFCs. Sources for VOCs can be partitioned largely into anthropogenic and biogenic emissions, with episodic contributions from biomass burning and volcanic eruptions.

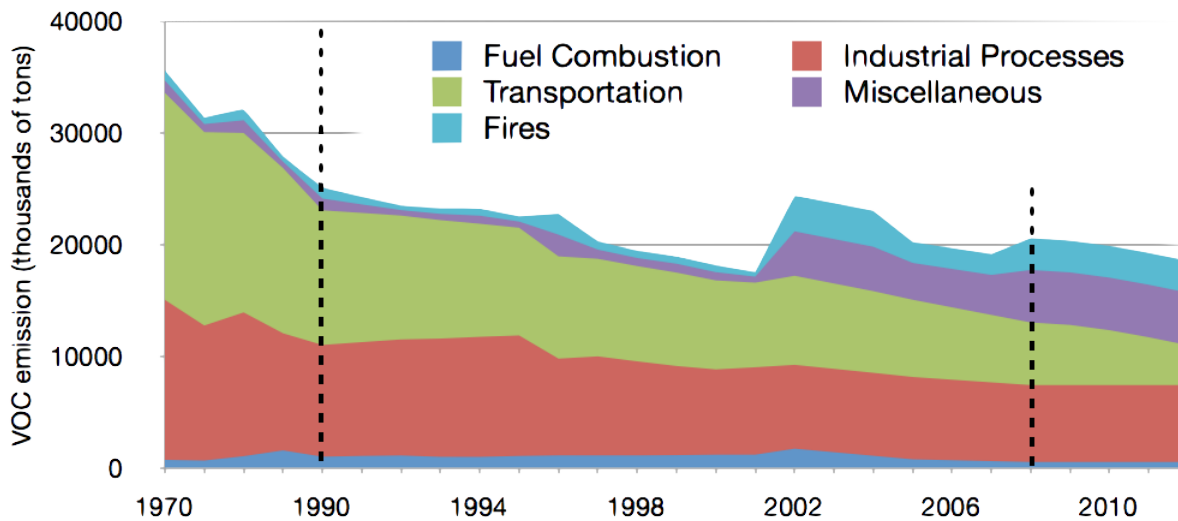


Figure 1.2: **National Emission Inventory (NEI) VOC emission trend** — Trend for total NEI VOC emission for 1970–2012. Data points prior to 1990 were reported every 5 years. 2006 and 2007 are interpolation of 2005 and 2008 data. After 2008, except for transportation, all other emissions were assumed constant. While some changes are real, some are due to changes in inventory methodology.

According to the EPA’s 2008 National Emission Inventory (NEI), the leading sources for anthropogenic VOCs in the United States are industrial processes, emitting 6.9×10^6 tons and contributing to a third of the national anthropogenic VOC budget including wild fires (Fig. 1.2). VOC emission from transportation was 5.6×10^6 tons (27% of total). These numbers are to be compared to 2005 figures of 7.4×10^6 tons (36% of total) for industrial processes and 6.9×10^6 tons (34%) for transportation. Further reduction in emission from transportation is seen in 2011, down to 4.3×10^6 tons. However, emission from wild fires have drastically increased to 2.8×10^6 tons

(4%) in 2008 from 1.9×10^6 tons (3%) in 2005¹. Also, emission from the “miscellaneous” category, which includes sources such as prescribed fire and gas stations, also increased from 3.3×10^6 tons (9%) in 2005 to 4.7×10^6 tons (14%) in 2008. Totals excluding wild fire were 18.3×10^5 tons for 2005 and 17.7×10^6 tons for 2008.

NEI2008 also estimated 31.7×10^6 tons of biogenic VOCs (BVOCs) in the contiguous United States (CONUS). In rural areas, BVOCs naturally dominates. On the synoptic scale, as anthropogenic VOC emission is being reduced through regulatory efforts, the impact of BVOCs on tropospheric chemistry is also becoming more important. Of the hundreds of BVOCs identified, the global flux is dominated by isoprene (C_5H_8) (Guenther *et al.*, 2006), which is primarily emitted by terrestrial foliage. Bottom-up global estimates of isoprene emission using the Model for Emissions of Gases and Aerosols from Nature (MEGAN) gives about 600 Tg for 2003 (Guenther *et al.*, 2006), and its regional distribution has been further constrained with satellite observation of formaldehyde (HCHO) column from satellite instruments such as the Global Ozone Monitoring Experiment (GOME) instrument on board of ERS-2 (Palmer *et al.*, 2001, 2003, 2006), the SCIAMACHY instrument on board of the ENVISAT (Dufour *et al.*, 2009; De Smedt *et al.*, 2008, 2010), and the Ozone Monitoring Instrument (OMI) on board of the EOS Aura satellite (Millet *et al.*, 2008; Marais *et al.*, 2012).

Due to ozone’s nonlinear sensitivity to changes in VOC, the simulation of ozone depends heavily on the accurate characterization of the emission inventory inputs or parameterization, which is the sole source for many hydrocarbons such as toluene or alkanes of high carbon numbers. Of particular interest to this study is how changes in each of these sources may impact the observed upper tropospheric ozone level and ultimately the chemistry budget.

¹ This increase is partially due to re-classification of “open burning” emissions into two separate categories of wildfires and prescribed burning in 2008.

1.1.2 Anthropogenic sources for Nitrogen oxides (ANO_x)

Due to the large contribution from BVOCs, the ambient ozone level is controlled by the oxides of nitrogen ($\text{NO}_x \equiv \text{NO} + \text{NO}_2$), which is dominated by anthropogenic NO_x (ANO_x). The straightforward conjecture is that the more NO_x is available, the higher the ozone concentration. However, this is not the case in either “clean” air, wherein VOC level is low, or in the presence of excessive NO_x . Either case can induce NO_x -titration, which is discussed briefly in Section 1.1. In addition, lightning-generated NO_x , or LNO_x , and soil² NO_x are also identified as an important natural source for atmospheric NO_x . Introduction to LNO_x is provided in the next section (Section 1.2).

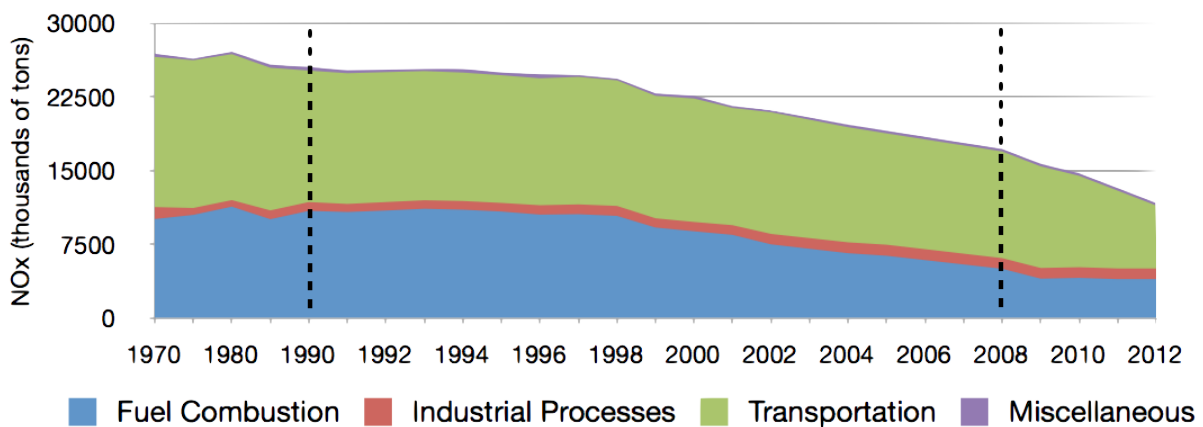


Figure 1.3: **National Emission Inventory (NEI) NO_x emission trend** — Trend for total NEI NO_x emission for 1970–2012. Data points prior to 1990 were reported every 5 years. 2006 and 2007 are interpolation of 2005 and 2008 data. After 2008, except for transportation, all other emissions were assumed constant. While some changes are real, some are due to changes in inventory methodology.

Global ANO_x emission has gradually decreased over the last two decades. Müller (1992) estimated a 72 Tg N/yr global emission for during the 1980’s. The Intergovernmental Panel of Climate Change (IPCC) Third Assessment Report (AR3) estimated 28–32 Tg N from fossil fuel combustion, out of an approximately 50 Tg N annual global total NO_x sources at the end of the 20th century (Schumann and Huntrieser, 2007; Lamarque et al., 2010, and references therein). In

² Emissions of NO_x from soil due to bacterial denitrification and biodecay are sometimes classified as biogenic emission.

particular, emission of ANO_x in the United States has been reduced substantially over the years. Figure 1.3 shows the NEI national trend expressed in thousands of tons of total NO_x . The primary sources of ANO_x in the U.S. have been consistently dominated by the transportation and fuel combustion sectors, contributing to 63% and 29%, respectively, of the total ANO_x . Comparing 2005 and 2008 NEI, NO_x from transportation has been reduced by 4.2% and NO_x from fuel combustion has been reduced by 21%. Such trend has also been observed through combined model-satellite studies (*Kim et al.*, 2009).

Similar to VOCs (Section 1.1.1), the reduction in ANO_x has gradually increased the relative importance of its natural counterparts. Nonetheless, the overall decline in ANO_x does not preclude the role of ANO_x in tropospheric ozone chemistry. Specifically, the co-location of ANO_x and various anthropogenic sources for VOCs continues to dominate the anthropogenic-factor of tropospheric ozone production (e.g. *Kim et al.*, 2011).

1.2 Parameterizing Lightning-generated NO_x (LNO_x)

The global emission rate of LNO_x is highly uncertain and largely unconstrained because of the transient nature of lightning, thus introducing uncertainties in ozone climate simulations. The best current estimate for LNO_x is $5 \pm 3 \text{Tg N}$ per year globally, which contributes to around 10% of the total NO_x emission (*Schumann and Huntrieser*, 2007). Despite being a smaller direct source than ANO_x , LNO_x has a comparable potential for ozone production due to its direct emission in the free troposphere, where it has a much longer lifetime than in the boundary layer (*Lamarque et al.*, 1996; *Allen et al.*, 2000; *Schumann and Huntrieser*, 2007, and references therein). *Hauglustaine et al.* (2001) used the Model for OZone And Related chemical Tracers (MOZART) to study the ozone produced from LNO_x and found ozone enhancement of over 140% at 250 mb in January above southern Atlantic, Africa, and south America. Similarly, *Cooper et al.* (2007) also found that the North American Monsoon upper tropospheric ozone enhancement, the central topic of this thesis, is largely due to LNO_x .

1.2.1 Overview of lightning physics

Lightning flashes are the result of spontaneous electric discharges from accumulated charge volumes within a thunderstorm. Empirical studies point to the likelihood that the dominant electric charge generating process within convective systems is the non-inductive charge transfer arisen from the asymmetric elastic collisions between ice crystals and graupel within the updraft region (*Reynolds et al.*, 1957; *Jayaratne and Saunders*, 1985; *Saunders et al.*, 2006, and references therein). Charge separation is then promoted by the differential terminal velocities between particles of different sizes. Further charge transport is facilitated by the rapid convective motion within the storms. By observing changes in electric field measured from the ground. *Wilson* (1916) was the first to observe through experiments that thunderstorms typically exhibit a positive dipole structure, wherein positive charges are situated on top. More recent studies such as *Stolzenburg et al.* (1998) also suggested multipole structures within mesoscale convective systems (MCS) as illustrated in Figure 1.4. Regardless of the presumed charge structure, the initial charging zone is governed by the presence of a heterogenous mixture of frozen cloud particles, which leads to the temperature and microphysics dependence used by many parameterization.

A common approach to modeling the triggering process given a charge distribution is the stochastic dielectric breakdown model formulated by *Niemeyer et al.* (1984); *Wiesmann and Zeller* (1986). For example, *Mansell et al.* (2002), in constructing an explicit scheme for lightning parameterization, used a height-varying initiation threshold with upper and lower bounds of 30 kV m^{-1} and 125 kV m^{-1} . Once the threshold has been reached, a branched stepped leader (discrete connected

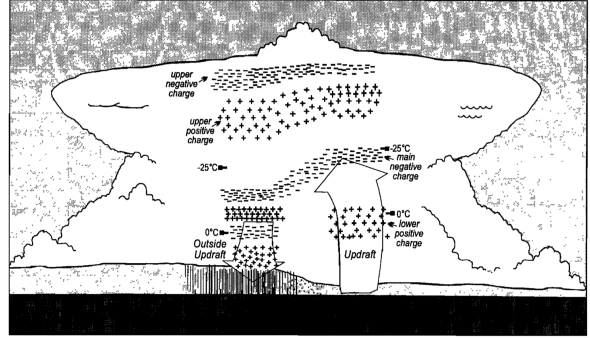


Figure 1.4: Illustration of MCS electric charge structure from *Stolzenburg et al.* (1998) — Illustration of a mesoscale convective system (MCS) with a multipole charge structure (after *Stolzenburg et al.*, 1998, Figure 3).

charged link) begins to form with an average downward propagation speed of 2×10^5 m/s and peak pulse current > 1 kA (*Uman and Krider*, 1989). For a negative cloud-to-ground (CG-) lightning, once the stepped leader (-) connects with an upward-moving discharge from the ground (+), a return stroke is formed. The first return stroke is typically one that carries most of the charges in a flash, with a median positive peak current is about 20–30 kA, but can exceed 200 kA (*Orville et al.*, 2010; *Cummins and Murphy*, 2009).

Discharging roughly 4×10^8 J flash $^{-1}$, lightning channels may reach a temperature in excess of 10,000 K during the first return stroke. This rapidly heated channel then expands and generates an outward-propagating shockwave, which is observed as thunder from afar. Finally, both the channel itself and the shock front are rapidly cooled through mixing. This rapid heating and cooling has been identified as the source for LNO_x (see Section 1.2.3).

1.2.2 Flash rate parameterization

A common first step to parameterizing LNO_x emission is to constrain the lightning flash count distribution. Many studies have attempted to reduce its spatiotemporal uncertainty through a combination of ground-based lightning detection instruments (e.g. *Boccippio et al.*, 2001; *Hansen et al.*, 2010), satellite-borne instruments (e.g. *Ushio et al.*, 2001; *Jourdain et al.*, 2010; *Martini et al.*, 2011), convective outflow measurements (e.g. *Pickering et al.*, 1998; *Skamarock et al.*, 2003), and chemistry transport models (e.g. *Price et al.*, 1997; *Allen et al.*, 2010, 2012; *Ott et al.*, 2010). Using the predicted flash rate, one may then deduce the LNO_x emission and its distribution once provided a method for flash-to-emission conversion, which will be discussed in the next section (Section 1.2.3).

Work by Bernard Vonnegut (1914–1997) laid down the theoretical foundation for a physically-based parameterization of lightning flash rate. Based on the works of *Vonnegut* (1963) and *Williams* (1985), *Price and Rind* (1992) constructed a lightning parameterization based on cloud-top height. The theoretical basis may be summarized as follow (after *Boccippio*, 2002).

Conceptualize the electric structure of a thunderstorm as two tangential spherical charge volumes of radius R and charge density $\pm\rho$. Compared to more recent studies, which point to dipole (*Williams*, 1989) or multipole (*Stolzenburg et al.*, 1998) charge structures, a dipole approximation is an obvious but reasonable simplification by accounting for the dominating region for charge separation. Then, assume an aspect ratio of unity, *i.e.* horizontal dimensions are similar in size to the vertical dimension. *Boccippio* (2002) noted the potential of an “at best” factor-of-two inaccuracy under this assumption. A third simplification asserts that the dipole is maintained through a generator current modeled as a net charge transport velocity. Finally, it is assumed that the variation of this current is small. Expressing the generator power as a product of the generator current (I) and the electric potential of the dipoles (Φ), we have $P = I\Phi$. Applying the definitions of I and Φ and applying Gauss’ Law, *Boccippio* (2002) writes ³

$$P \sim \varepsilon^{-1} \rho^2 V_Q A z_d^2 \quad (1.10)$$

where V_Q is the charging velocity, $A = \pi R^2$ is the horizontal cross-section area of the charge volume, and $z_d = 2R$ is the dipole separation. Hence a fundamental conclusion is arrived here stating that the geometric term dominates the generator power. If power dissipation by lightning varies monotonically with the generator power and that each flash dissipates a constant amount of energy, then flash rate f is proportional to the generator power P and we write

$$f \sim \rho^2 V_Q A z^2 \quad (1.11)$$

Here, z_d has been simplified to storm height z . Three more final assumptions on storm properties can be made to make this relationship operationally viable. (1) Applying the assumption on the storm aspect ratio, A is replaced with z^2 . (2) Using w as the best approximation for V_Q . (3) Charge density has negligible variability at least within the dominant dipole regions. These simplifications produce the following relationship.

$$f \sim wz^4 \quad (1.12)$$

³ Assuming different charge geometry can lead to a different scaling relationship, e.g. asserting 2D charge plates instead of spheres would lead to $P \sim \rho_{gen} V_Q R^2 z_d E_{crit}$ (*Boccippio*, 2002).

Compiling data from several studies between 1962 – 1979, *Williams* (1985) observed a linear relationship between vertical velocity and cloud size for continental storms. This empirical relation allows one to further simplify 1.12 to obtain the continental flash rate f_c :

$$f_c \sim z^5 \quad (1.13)$$

This scaling relationship has been shown to be operationally viable in several studies (e.g. *Yoshida et al.*, 2009; *Ushio et al.*, 2001). Compiling data from *Williams* (1985), the empirical relationship of flash rate and cloud top height for continental storm is written as (*Price and Rind*, 1992, hereafter PR92)

$$f_c(z) = 3.44 \times 10^{-5} z^{4.9} \quad (1.14)$$

Alternatively⁴ , f_c may be written as a function of the maximum updraft velocity w_{\max} , giving $f_c \sim w_{\max}^{4.54}$. While the linear relationship between w_{\max} and cloud top height in continental clouds is confirmed by *Price and Rind* (1992), w_m for marine clouds appear to scale much slower with cloud size:

$$w_m = 2.86 z^{0.38} \quad (1.15)$$

Subsequently, a separate parameterization for marine clouds is formulated as $f_m = 6.2 \times 10^{-4} z^{1.79}$. Due to the lack of data, the marine relationship is not tested thoroughly and thus Equation 1.15 has been frequently challenged. *Michalon et al.* (1999), taking into account the effects of marine cloud condensation nuclei (CCN), rewrites f_m as $6.57 \times 10^{-6} z^{4.9}$. However, this has been quickly shown to produce excessive flash rates (?). Soon after, *Boccippio* (2002) shows that PR92's marine formulation is formally inconsistent with *Vonnegut* (1963) by correlating continental flash rates with marine cloud top heights, *i.e.* $f_c(z_m)$.

Price and Rind (1993) used the flash data from eleven states in the western United States, detected by wide-band magnetic direction finders, in combination with thunderstorm radar and radiosondes data to find a relation for the IC:CG ratio (Z) from cold-cloud depth (d), defined as

⁴ *Baker et al.* (1995) theoretically derived $f_c \sim w^6$ instead.

the distance from the freezing level to cloud-top.

$$Z = 0.021d^4 - 0.648d^3 + 7.49d^2 - 36.54d + 63.09 \quad (1.16)$$

In *Price and Rind* (1994), a “calibration factor” (c) for the resolution dependency of PR92 is introduced by regridding 5 km data between 1983 and 1990 from the International Satellite Cloud Climatology Project data set (ISCCP; *Rossow and Schiffler*, 1991) to different horizontal grid sizes. The resulting equation is as follow

$$c = 0.97241 \exp(0.048203\Delta A^\circ) \quad (1.17)$$

where ΔA° is the grid area in squared degrees. *Price and Rind* (1994) claims that there is no dependence of c on latitude, longitude, or season.

Other bulk-scale or resolved-scale storm parameters may also be correlated with lightning flashes for the purpose of formulating alternative parameterization schemes. For instance, *Allen and Pickering* (2002) and *Allen et al.* (2010) implemented a parameterization of flash rate to the square of deep convective mass flux. *Zhao et al.* (2009) and *Choi et al.* (2005) based the flash rate prediction on both the deep convective mass flux and the convectively available potential energy (CAPE). *Allen et al.* (2012) used a flash rate prediction scheme based on the convective precipitation rate. *Petersen et al.* (2005) gave a linear relation between flash rate and ice water path (IWP). *Deierling and Petersen* (2008) investigated a linear dependence of flash rate on updraft volume for $T < 273\text{ K}$ and $w > 5\text{ m s}^{-1}$. *Hansen et al.* (2012) produced a lookup-table for flash rate from convective precipitation and mixed phase layer depth by correlating data from observations. *Barthe et al.* (2010) compared several of these methods including PR92, through two case studies, and showed that while the polynomial orders are lower in the non-cloud-top based formulations, the level of uncertainties may still be higher than PR92 due to a combination of errors from model biases in the parameters used, e.g. hydrometeors, and observational biases in the datasets used for constructing the relationships. *Futyan and Del Genio* (2007) arrived at a similar conclusion about the reduced reliability of precipitation-based approaches in global climate simulations for

predicting lightning flash rate. Explicit schemes, wherein electrification within convective cells are resolved, also exist (e.g. *Barthe et al.*, 2005; *Zhang et al.*, 2003). However, they are often too costly for synoptic modeling and thus their usages are limited to single-storm case studies.

1.2.3 Lightning-generated NO_x

Lightning-generated NO_x (LNO_x) is produced shortly following a channel formation. One prevalent theory for explaining LNO_x production is the shockwave heating theory, which describes NO molecules being formed in the air surrounding the lightning channel according to the Zel'dovich mechanism (*Zeldovich*, 1966; *Borucki and Chameides*, 1984, and references therein): When the cylindrical shock is propagating outwards from the current, air is heated to $\sim 2500\text{ K}$ at the shock front, which produces a high NO-to-N₂ equilibrium ratio. Behind the shock front, air is rapidly cooled to the ambient temperature, which “freezes” the NO-to-N₂ ratio obtained at the prior instant. However, *Stark et al.* (1996) argued that the shockwave does not travel fast enough to produce the necessary temperature for Zel'dovich mechanism.

Using experimental data, *Wang et al.* (1998) relates the production of NO (in $10^{21}\text{ molecules/m}^3$) to peak current (I) and pressure (p):

$$n_{\text{NO}}(I) = 0.14 + 0.026I + 0.0025I^2 \quad (1.18)$$

$$n_{\text{NO}}(p) = 0.34 + 1.30p \quad (1.19)$$

The correlation factor (r^2) for the above fits to measurements are 0.89 and 0.67 respectively, but it should be noted that the coefficients in Equation 1.18 have significant relative uncertainty (± 0.33 , ± 0.036 , ± 0.0009 respectively).

Using the mean peak current from remote sensing measurements, *Price et al.* (1997) estimated that intracloud (IC) flashes produce only 10% of the energy produced by cloud-to-ground (CG) flashes and thus deducing that the moles of NO per flash from IC is also a factor of 10 smaller than that from CG, which is calculated at 1.1 kmoles per CG flashes. However, more recent studies have found that such ratio is grossly overestimated and that both IC and CG flashes produce

approximately the same amount of NO. *Ott et al.* (2010) estimated 500 moles NO per flash or 7 kg N per flash with a range of 360–700 moles NO per flash. This is compared to a calculation using the median peak current from North American Lightning Detection Network (NLDN; *Orville et al.*, 2002) and relationship in *DeCaria et al.* (2000) after *Wang et al.* (1998).

After the total emission of a flash is estimated, one may want to assign a spatial distribution to the molecules. In models that are capable of resolving explicit electrification, flash path, and stroke tortuosity (e.g. *Mansell et al.*, 2002), those details may be leveraged in combination with Equation 1.19 to compute the vertical distribution (*Barthe and Pinty*, 2007). In regional models, a fixed column profile based on cloud extent or observations are often used instead. *DeCaria et al.* (2000) prescribes a Gaussian-like distribution for emissions from CG flashes and a bimodal distribution for IC flashes. Horizontal distribution based on 20 dBZ reflectivity is also proposed by *DeCaria et al.* (2005) based on *MacGorman and Rust* (1998). *Pickering et al.* (1998) derived total LNO_x profiles with a peak at the detrainment level and a maximum in the boundary layer by using measurements from multiple campaigns and 2D models. *Ott et al.* (2010) corrected these profiles by using a 3D model, and found that convective updraft removes the boundary layer maximum and places a single maximum at 6–9 km for midlatitude storms. *Hansen et al.* (2010) also investigated the vertical distribution of flash segments for four storms and found that profiles can exhibit large variabilities.

Several modeling studies have approached LNO_x parameterization using scaling/assimilation techniques. For example, *Hudman et al.* (2007) used the 500 moles NO per flash from *Ott et al.* (2010) in combination of NLDN CG flash counts adjusted by IC:CG ratio suggested by *Boccippio et al.* (2001). *Jourdain et al.* (2010) scaled flash rates regionally to Optical Transient Detector/Lightning Imaging Sensor (OTD/LIS *Boccippio et al.*, 2000) monthly and 44 flashes/s globally annually to be consistent with climatology from *Christian et al.* (2003). The scaled LNO_x strength is further constrained using observation of O₃ by Tropospheric Emission Spectrometer (TES *Beer*, 2006). *Schumann and Huntrieser* (2007, Table 24) also compiled a list of 78 studies with dependence on

LNO_x production rate since 1981 and found that large number of studies without sufficient a priori reasons for choosing their prescribed source strength.

In conclusion, lightning parameterization remains a major uncertainty in tropospheric ozone modeling. Many methods have been proposed with varying degrees of generality and complexity. This study has elected to use the simplest method available for flash rate parameterization, *i.e.* *Price and Rind* (1992), which is evaluated in depth in Chapter 2.

1.3 Summary

This chapter has summarized various aspects of ozone chemistry relevant to the upper tropospheric ozone enhancement studied by *Li et al.* (2005) and *Cooper et al.* (2007). While residing in the upper troposphere, due to the nonlinearity of the $\text{O}_3\text{-VOC-NO}_x$ chemistry, the ability to simulate and analyze the ozone enhancement depend heavily on the model's skill in simulating vertical transport (convective or advective), chemistry, as well as prescribing or parameterizing emissions. Of the three primary emission sources (anthropogenic, biogenic, and lightning), lightning NO_x is the least well-constrained because of its transient nature and its sensitivity to cloud parameters, for which the values will be obtained from parameterized convection in this study. Furthermore, *Cooper et al.* (2009) found that the ozone enhancement depends strongly on lightning emission. Therefore, before conducting the modeling study to understand the upper tropospheric ozone enhancement (Ch. 3), the parameterization of lightning emission is evaluated and discussed in depth Ch. 2.

Even though previous studies have already investigated the enhancement phenomenon and shown with confidence the contributions from dynamics and emissions to the inter-annual variability, little research has been done in understanding the spatiotemporal structure of the chemistry at higher granularity. Using a single high-resolution model, *Barth et al.* (2012) showed substantial daily variability during the 2006 North American Monsoon. By trading off resolution and accuracy especially in convection, this study mimics *Barth et al.* (2012) and supplements its results with

additional diagnostics and sensitivity simulations. Reiterating the goals stated at the beginning of this chapter, and given the additional background information on the intricacy of studying upper tropospheric ozone, this thesis intends to answer the following questions:

- (1) Trading off model resolution and parameterizing convection, how well can the model simulate the ozone enhancement? This will be addressed through detailed validation exercises against various observations in Chapter 3.2.
- (2) Considering the various factors controlling ozone, what is the relative importance of each component to the overall ozone level? By using various diagnostics and techniques, this question will be addressed in Chapter 3.3. ⁵
- (3) Focusing on each emission source, how sensitive is the ozone enhancement to various scenarios? Separate simulations are performed by varying emission parameters, this is evaluated in Chapter 3.4.

⁵ **Editing note:** Later drafts may separate 3.3, 3.4 into Chapter 4, thus moving Chapter 4 to Chapter 5 resulting in 4 core chapters.

Chapter 2

Lightning parameterization

Over the last decade, predictions of lightning flash statistics in numerical weather and climate models have garnered increasing interests. One of the likely drivers is the advances in online chemistry models, wherein chemistry is simulated alongside of physics (e.g., *Grell et al.*, 2005). Lightning-generated nitrogen oxides (LNO_x) are predicted to be very efficient in accelerating the production of tropospheric ozone, which is identified as a significant greenhouse gas in the upper troposphere (*Lacis et al.*, 1990; *Kiehl et al.*, 1999). *Cooper et al.* (2007) showed that , lightning can contribute 25–30 ppbv of upper tropospheric ozone during the summertime North American Monsoon. *Choi et al.* (2009) has remarked on the increasing importance of LNO_x in tropospheric ozone production as anthropogenic sources of NO_x are being reduced in the United States. Furthermore, the inherent nonlinearity between NO_x emission and commonly validated quantities such as radiative balances and ozone concentration makes it challenging to quantify the skill of a LNO_x parameterization through proxy or total NO_x measurements. Therefore, it is important to evaluate existing lightning parameterizations by directly validating flash rate predictions in order to more accurately interpret results from models that incorporate LNO_x emission.

The most commonly used method for parameterizing lightning flash rate is perhaps that by *Price and Rind* (1992, 1993, 1994). It has been used by chemistry transport modeling studies such as GEOS-Chem (*Hudman et al.*, 2007), MOZART-4 (*Emmons et al.*, 2010), and CAM-Chem (*Lamarque et al.*, 2012). Continental flash rates are related to the fifth-power of cloud-top height by *Williams* (1985) and *Price and Rind* (1992, hereafter PR92) through empirical evidences that

are consistent with the theoretical scaling arguments of *Vonnegut* (1963). The partitioning between intracloud and cloud-to-ground flashes, or IC:CG ratio, is estimated with a fourth-order polynomial of cold cloud-depth, i.e., distance between freezing level and cloud-top, in *Price and Rind* (1993, hereafter PR93). Finally, the parameterization is generalized for different grid sizes with an extrapolated “calibration factor” in *Price and Rind* (1994, hereafter PR94).

The goals of this study are to evaluate the cloud-top height based parameterization (PR92, PR93, and PR94) across the bridging resolutions between those commonly used by global chemistry models ($\Delta x \sim O(1^\circ)$) and cloud-resolving models ($\Delta x < 5\text{ km}$), and report on statistics over time periods useful for studying upper tropospheric chemistry ($O(\text{month})$) (*Stevenson et al.*, 2006). It is, however, not the goal of this study to invalidate previous studies, but to draw attention to the need for careful implementation and validation of the use of these parameterizations. Here we report on experiments using PR92, PR93, and PR94 implemented into the Weather Research and Forecasting model (WRF; *Skamarock et al.*, 2008), focusing on results from simulations performed at 36 km and 12 km grid-spacing. A simulation at 4 km grid spacing for 2 weeks in July and August 2006 is also analyzed to demonstrate how PR92 behaves transitioning from cloud-parameterized to cloud-permitting resolutions and provide insights on how or whether such transition can be done.

Similar studies have been performed for global models (e.g., *Tost et al.*, 2007), but previous regional-scale modeling studies utilizing PR92 at comparable horizontal grid spacings have not provided evaluations of the lightning parameterization. Thus, there has been insufficient information to understand the behavior of PR92 in this regime. Even though these formulations were derived using near-instantaneous data at a cloud-permitting resolution (5 km), past applications often utilize temporally and spatially averaged cloud-top height outputs or proxy parameters. While the effects of spatial averaging is addressed by the PR94 scaling factor, effects of temporally averaging cloud-top heights are rarely addressed and may lead to significant underestimation due to the fifth-power sensitivity (*Allen and Pickering*, 2002). Addressing the potential issue of temporal averaging, instantaneous cloud-top heights and updraft velocities at each time step are leveraged. Comparisons are then performed for temporal, spatial, and spectral features.

The next section (Sect. 2.1) outlines the methods used in this study, which includes the formulation and overview of the parameterization (Sect. 2.1.1), relevant aspects of the model setup, practical considerations of implementing PR92 (Sect. 2.1.2), and the data used for validation (Sect. 2.1.3). Section 2.2 describes the model results and discusses the implications of various statistics from validation against observations of precipitation, flash rate, and IC:CG ratios. Section 2.3 discusses how the performance of PR92 transitions between different resolutions (Sect. 2.3.1) and between theoretically similar formulations (Sect. 2.3.2). Finally, Sect. 2.4 provides a summary of key results and cautionary remarks on specific aspects of the utilization of PR92, PR93, and PR94.

2.1 Methods

2.1.1 Parameterization overview

In PR92, a fifth-power relation between continental lightning flash rate (f_c) and cloud-top height (z_{top}) is established with observational data following the theoretical and empirical frameworks of *Vonnegut* (1963) and *Williams* (1985). Assuming a dipole structure with two equal but opposite charge volumes and a cloud aspect ratio of approximately one, it is first formulated, based on scaling arguments of *Vonnegut* (1963), that the flash rate would be proportional to maximum vertical updraft velocity (w_{max}) and fourth-power of cloud dimension. Imposing a linear relation between w_{max} and cloud dimension, the flash rate relationship can be reduced to fifth power of z_{top} (*Williams*, 1985). It is empirically fit to radar and flash rate data from several measurements between 1960–1981 to give the continental equation (*Price and Rind*, 1992):

$$f_c(z_{\text{top}}) = 3.44 \times 10^{-5} z_{\text{top}}^{4.9}. \quad (2.1)$$

PR92 also estimated that $w_{\text{max}} = 1.49 z_{\text{top}}^{1.09}$ for continental clouds, thus allowing a second formulation based on maximum convective updraft:

$$f_c(w_{\text{max}}) = 5 \times 10^{-6} w_{\text{max}}^{4.54}. \quad (2.2)$$

Table 2.1: WRF simulations performed for lightning parameterization study.

Case #	dx (km)	dt (s)	Output	Duration
1	36	90	hourly	JJA 2006
2	36	90	hourly	JJA 2011
3	12	36	3-hourly	Jul 2011
4	4	12	hourly	25 Jul–7 Aug 2006

A separate formulation of second-order, instead of fifth-order, is also derived by *Price and Rind* (1992) for marine clouds, for which updraft velocity is observed to be significantly slower:

$$f_{m(PR92)}(z_{\text{top}}) = 6.2 \times 10^{-4} z_{\text{top}}^{1.73}. \quad (2.3)$$

Taking into account effects from cloud condensation nuclei, *Michalon et al.* (1999) modified the marine equation to fifth-order:

$$f_{m(M99)}(z_{\text{top}}) = 6.57 \times 10^{-6} z_{\text{top}}^{4.9}. \quad (2.4)$$

The practical viability of the continental relation was proven by *Ushio et al.* (2001) and *Yoshida et al.* (2009) through several case studies. However, *Boccippio* (2002) showed that the marine equations are formally inconsistent with *Vonnegut* (1963), and that the marine equations cannot be inverted to produce cloud tops within the range of cloud-top observations.

Price and Rind (1993) used the flash data from eleven states in the western United States, detected by wide-band magnetic direction finders, in combination with thunderstorm radar and radiosondes data to find a relation for the IC:CG ratio (Z) from cold-cloud depth (d), defined as the distance from freezing level to cloud-top.

$$Z = 0.021d^4 - 0.648d^3 + 7.49d^2 - 36.54d + 63.09 \quad (2.5)$$

In *Price and Rind* (1994), a “calibration factor” (c) for the resolution dependency of PR92 is introduced by regridding 5 km data between 1983 and 1990 from the International Satellite Cloud Climatology Project dataset (ISCCP; *Rossow and Schiffler*, 1991) to different horizontal grid sizes.

The resulting equation is as follows:

$$c = 0.97241 \exp(0.048203R) \quad (2.6)$$

where R is the grid area in squared degrees. *Price and Rind* (1994) claim that there is no dependence of c on latitude, longitude, or season. For the grid sizes used in this study, the values of c are 0.9774 for 36 km, 0.973 for 12 km, and 0.9725 for 4 km.

2.1.2 Model setup and implementation

Simulations in this study are performed using the Weather Research and Forecasting (WRF) model version 3.2.1 (*Skamarock et al.*, 2008) over the contiguous United States (CONUS), including part of Mexico and Canada (Fig. 2.1). The simulations have slightly different model domains because the simulations were developed and performed for objectives independent of validating the lightning parameterization. Meteorology is initialized and continuously nudged (horizontal winds, temperature, water vapor) with the National Center for Environmental Prediction (NCEP) Global Forecasting System (GFS) final (FNL) gridded analysis at 6 h intervals (00:00 UTC, 06:00 UTC, 12:00 UTC, 18:00 UTC). Four simulations are performed (Table 2.1), two at 36 km grid spacing, one at 12 km grid spacing, and one at 4 km grid spacing. All cases use the same vertical coordinates with 51 sigma levels up to 10 hPa. The Grell–Devenyi ensemble convective parameterization (*Grell and Devenyi*, 2002) with *Thompson et al.* (2008b) microphysics is used for the simulations where grid-spacing $\Delta x > 10$ km, for which a convective parameterization is needed. The implementation of the GD scheme employed in this

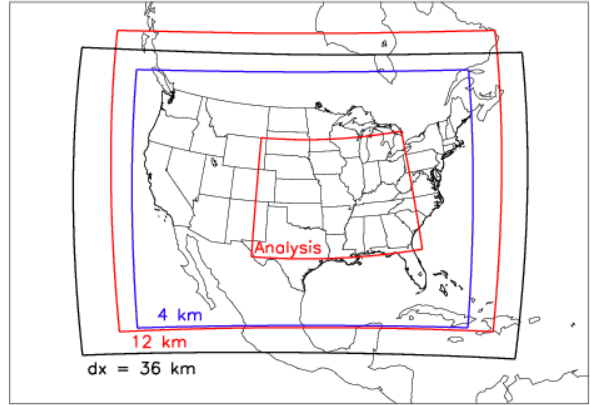


Figure 2.1: **Domain for lightning simulations** — Non-nested domains for WRF simulations and region for lightning simulations.

study consists of $3 \times 3 \times 16 = 144$ ensemble members comprising of interactions between different dynamic control and static control/feedback closures. The maximum moist static energy (MSE) is then used as input with entrainment to calculate the level neutral buoyancy (LNB), or cloud top. For further information about the convective parameterization, readers are encouraged to refer to Grell (1993).

Since the simulations were designed independently, some physics options used are not consistent. The planetary boundary layer (PBL) parameterization is handled by the Yonsei University scheme (*Hong et al.*, 2006) at 36 km and Mellon–Yamada–Janjic (MYJ) scheme (*Janjić*, 1994) at 12 km and 4 km. At 36 km, the surface layer physics option used is based on Monin–Obukhov similarity theory. The surface layer option used at 12 km and 4 km is also based on Monin–Obukhov theory but includes Zilitinkevich thermal roughness length.

While theoretically the scaling argument of *Vonnegut* (1963) does not distinguish between definitions of cloud-top height, the data used to derive the PR92 relation are radar reflectivity cloud-top heights at a certain reflectivity threshold. In the WRF implementation of Grell–Devenyi convective parameterization, the level of neutral buoyancy (LNB) is computed, with convective entrainment and detrainment accounted for within the calculation of cloud moist static energy, and readily available as a proxy for sub-grid cloud-top height. Thus, instead of 20 dBZ reflectivity cloud top, z_{top} is approximated by reducing LNB by 2 km, which will be shown to produce results within the range of the observed values. The choice of 2 km reduction is made independent of, but supported by, a recent study comparing different definitions of LNB and found the traditional “parcel” method definition of LNB over estimates the level of maximum detrainment by 3 km (*Takahashi and Luo*, 2012). Section 2.5 contains detailed discussions of the choice of 2 km cloud-top reduction and how it compares to offline computations of 20 dBZ cloud tops. Alternative methods for estimating the difference between the two heights can be formulated by directly taking into account their respective definitions. However, echoing *Barthe et al.* (2010), such addition of complexity increases the number of sources for uncertainty, especially in the context of parameterized convection. Similarly, using modeled cloud particle variables would also add an additional level of sensitivity

due to sub-grid variability in hydrometeor mixing ratios. Therefore, reflectivity calculations are only performed in the 4 km simulation and only for the purpose of redistributing lightning flashes horizontally as described below.

For case 4 (Table 2.1), convection is explicitly simulated with a modified *Lin et al.* (1983) microphysics scheme. Since no convective parameterization is used, the resolved maximum vertical velocities (w_{\max}) within the convective core are utilized (*Barth et al.*, 2012), and Eq. (2.2) is used instead of Eq. (2.1) for estimating flash rate. In addition, since a single storm may often cover multiple model grids, flashes are redistributed to within regions with a minimum reflectivity of 20 dBZ calculated using hydrometeor (rain, snow, graupel) information that is now better constrained at 4 km. The IC:CG ratio is prescribed using a coarse version of the *Boccippio et al.* (2001) 1995–1999 climatological mean, which was computed using data from the Optical Transient Detector (OTD; *Boccippio et al.*, 2000) and the National Lightning Detection Network (NLDN; *Cummins and Murphy*, 2009). Because PR92 developed Eq. (2.2) based on data at 5 km resolution, no resolution scaling is done to this simulation. Because this particular simulation was driven by the meteorology of its own WRF outer domains, it is restarted “cold” on 2 August to be consistent with the outer domain meteorology.

Most of the implementations used in these simulations are arguably “untuned” and not scaled to climatology or observations by any additional tuning factors, with the exceptions of the 2 km cloud-top height reduction used in the cases with parameterized convection and the prescribed climatological IC:CG ratios in case 4. Therefore, the correctness and predictiveness of the flash rate parameterization are not guaranteed at the time of the simulation given the lack of supporting validations of PR92 at the tested grid spacings. However, without feedback to the meteorology (except in case 4) and providing sufficient linearity in the biases of flash prediction, offline comparisons should reveal any tuning requirements for operational and research uses.

2.1.3 Data description

While desirable, event-by-event analysis would be technically challenging because the simulation may not produce the same strength, timing, and location of each convective event. Furthermore, an event-by-event analysis is unnecessary in the context of a mesoscale upper tropospheric chemistry study, of which the meaningful timescales often average biases from many individual events. Therefore, a large area where thunderstorms commonly occur is selected. The “analysis domain,” defined as 30°– 45°N, 80°– 105°W (Fig. 2.1), is used for time series and statistical comparisons.

The predicted lightning properties depend strongly on how the model simulates convection. Thus, in Sect. 2.2.1, WRF simulated precipitation is compared against National Weather Service (NWS) precipitation products to evaluate the model’s skill in representing convective strengths. The data are collected from radars and rain gauges and improved upon using a Multi-sensor Precipitation Estimator (MPE). Manual post-analyses are then performed by forecasters to identify systematic errors (http://www.srh.noaa.gov/abrfc/?n=pcpn_methods). The final data products used here are mosaic CONUS precipitation maps from 12 River Forecast Centers (RFCs) during JJA 2006 and 2011. The data are gridded into 4 km resolution and are available as 24 h totals over a hydrological day beginning and ending at 12:00 UTC.

The simulated CG flash counts, computed online as predicted total flashes × predicted CG fraction, are compared against data from the Vaisala US National Lightning Detection Network (NLDN; *Cummins and Murphy*, 2009). The network provides continuous multiyear CONUS and Canada coverage of > 90 % of all CG flashes with ongoing network-wide upgrades (*Orville et al.*, 2002, 2010). The median location accuracy is 250 m, which is well within the resolutions employed in this study. Multiple strokes are aggregated into a single flash if they are within 1 s and no more than 10 km apart. Weak positive flashes with < 15 kA have been filtered from all data. Finally, the flash data are binned into hourly flash counts for each model grid cell for comparison against model output.

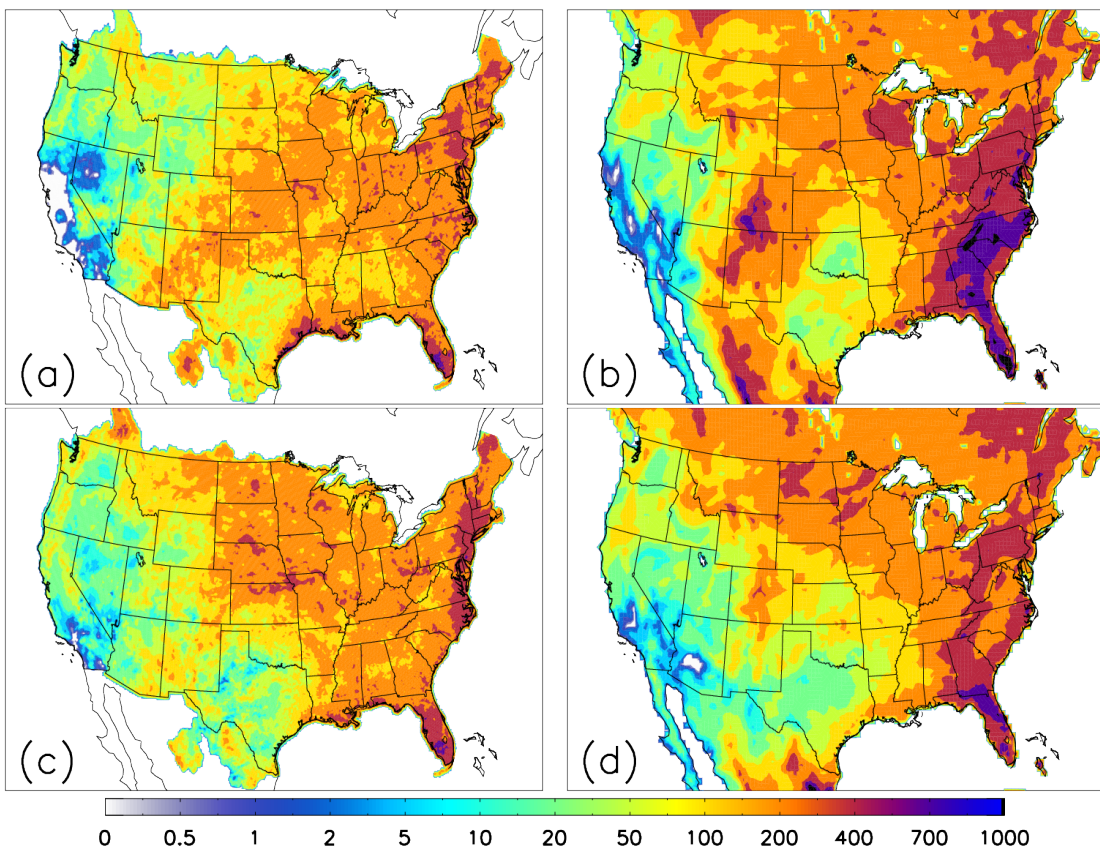


Figure 2.2: **Spatial distribution of JJA total precipitation in 2006 and 2011** — Spatial distribution of 2006 and 2011 JJA total precipitation in millimeters. (a) and (c) are NWS precipitation degraded to 12 km resolution. (b) and (d) are 36 km WRF-simulated total precipitation over the same periods with data above water surfaces masked.

Data from Earth Networks Total Lightning Network (ENTLN), previously WeatherBug Total Lightning Network (WTLN), are used to validate the model-produced IC:CG ratios. ENTLN employs a wide-band system that operates between 1 Hz to 12 MHz (*Liu and Heckman, 2011*). The theoretical detection efficiency (DE) for CG flashes across CONUS is 90–99 %, while the IC DE falls between 50–95 % (50–85 % within the analysis domain). Since the mappings of the corresponding DEs are not available with the data, 95 % and 65 % are used for CG and IC DEs, respectively, in analyses for which a prescribed DE is required. To address the concern of the impact of this simplification, the range of possible flash counts, IC:CG ratios, and biases will be provided when appropriate within the discussion in Sect. 2.2 to place bounds on the uncertainty. Due to the limited deployment duration of the network, only the IC:CG ratios during JJA 2011 within the analysis domain (see Fig. 2.1) are estimated and compared. For consistency with the comparisons against NLDN CG flash counts, the stroke aggregation criteria used here are 10 km and 1 s as done by NLDN, instead of the 10 km and 700 ms window typically used by Earth Networks to generate flash statistics.

2.2 Results and discussions

2.2.1 Precipitation

While lightning does not directly depend on precipitation, they are both the results of the same processes that promote ice–graupel collisions. Further, precipitation is observed robustly and continuously, thus giving us a high quality measurement for validating model results. On the other hand, while convective mass flux may produce a more consistent correlation with lightning, the lack of well-controlled direct observations and the large uncertainty in model calculations make it an inferior proxy for convective strength in this context.

Figure 2.2 shows the total precipitation during JJA 2006 and 2011 over the CONUS as simulated at 36 km grid spacings by WRF and observed by NWS. The gradients across the CONUS for both years are well captured by the model, but WRF has a high bias for 2006. WRF also

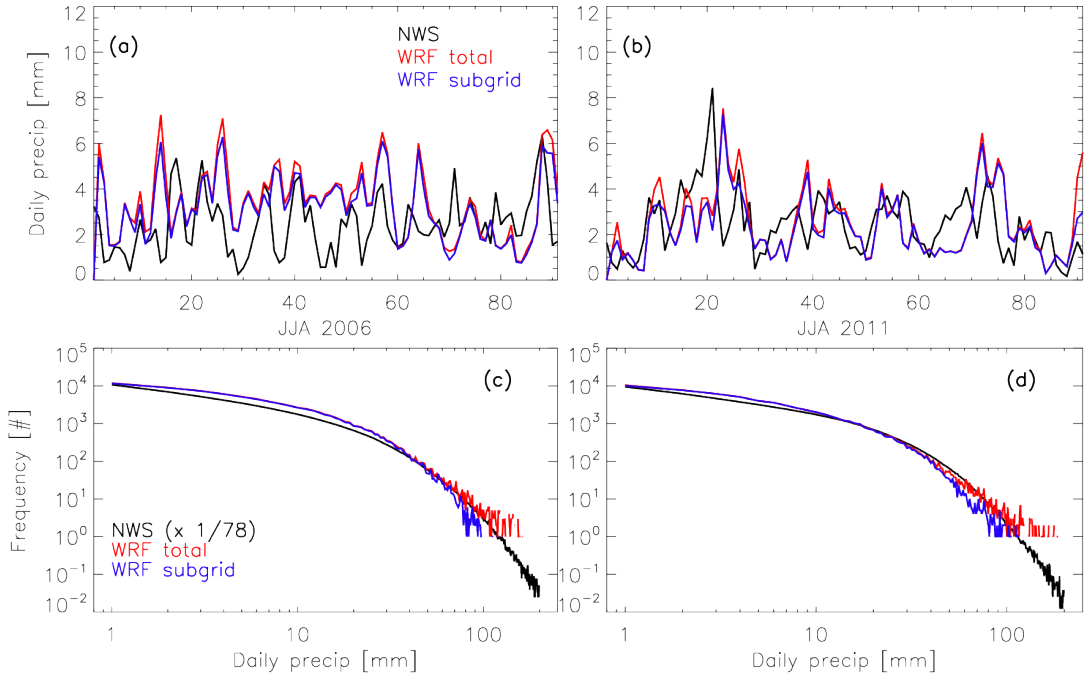


Figure 2.3: Time series and frequency distribution for 2006 and 2011 daily precipitation
— Time series and frequency distributions for JJA 2006 and 2011 area-averaged daily precipitation within the analysis region (see Fig. 2.1). Distributions for NWS are scaled by the ratios between total grid counts in WRF at 36 km and total grid counts in NWS within the analysis boundaries ($\sim 1/78$). WRF subgrid is the portion of precipitation from subgrid cumulus parameterization. Only grid points with more than 1 mm of precipitation are included.

simulates up to an order of magnitude more precipitation for coastal regions for both years but primarily for 2006. The time series for mean daily area-averaged precipitation and frequency distributions for JJA 2006 within the analysis domain (Fig. 2.3a and c) also reveal a median model bias of 37 %. In particular, WRF predicted more than twice the precipitation between late-June and mid-July in 2006. In contrast, the median bias for 2011 is 4.9 % with almost equal occurrence of over- and under-predictions. The model frequency distribution for both years also closely track those observed (Fig. 2.3c and d) except at the high end of the distribution where limits of model grid resolution induces significant noise.

The simulated daily precipitation at 12 km is higher than the NWS observed precipitation by 24 % during July 2011. However, an anomalously strong diurnal cycle is simulated at 12 km grid spacing that is not present in the 36 km simulation. Comparing the area-averaged 12 km nocturnal precipitation over the entire analysis domain to that of 36 km output, nocturnal precipitation at 12 km is too low but the daytime precipitation is too high. One-day simulations were performed to evaluate the impact from the differences in model physics, but there remained significant unidentified discrepancies between the precipitation amount in the two runs that cannot be explained by horizontal resolution differences alone; thus, it is concluded that there is no value in redoing the entire simulation. The identified causes for the differences between the two simulations are, in decreasing order for magnitude of influence, initial conditions for soil temperature and soil moisture, differences in planetary boundary layer scheme (Sect. 2.1.2), and the land surface model option. Such difference in diurnal behavior in the simulations is expected to have significant impact on how the lightning parameterization is evaluated, but the full impact can be minimized through incorporation of precipitation into the analysis.

Large scale meteorology and moisture inputs are unlikely the causes for these biases due to nudging. In 2006, biases mostly occurred in the low-to-mid end of the distribution (i.e., light precipitation events, Fig. 2.3c), indicating that the problem lies in parameterizing subgrid events. Despite the differences in the eastern United States, convection over the central United States is reasonably represented. Finally, the goal of this study is not to evaluate the convective parame-

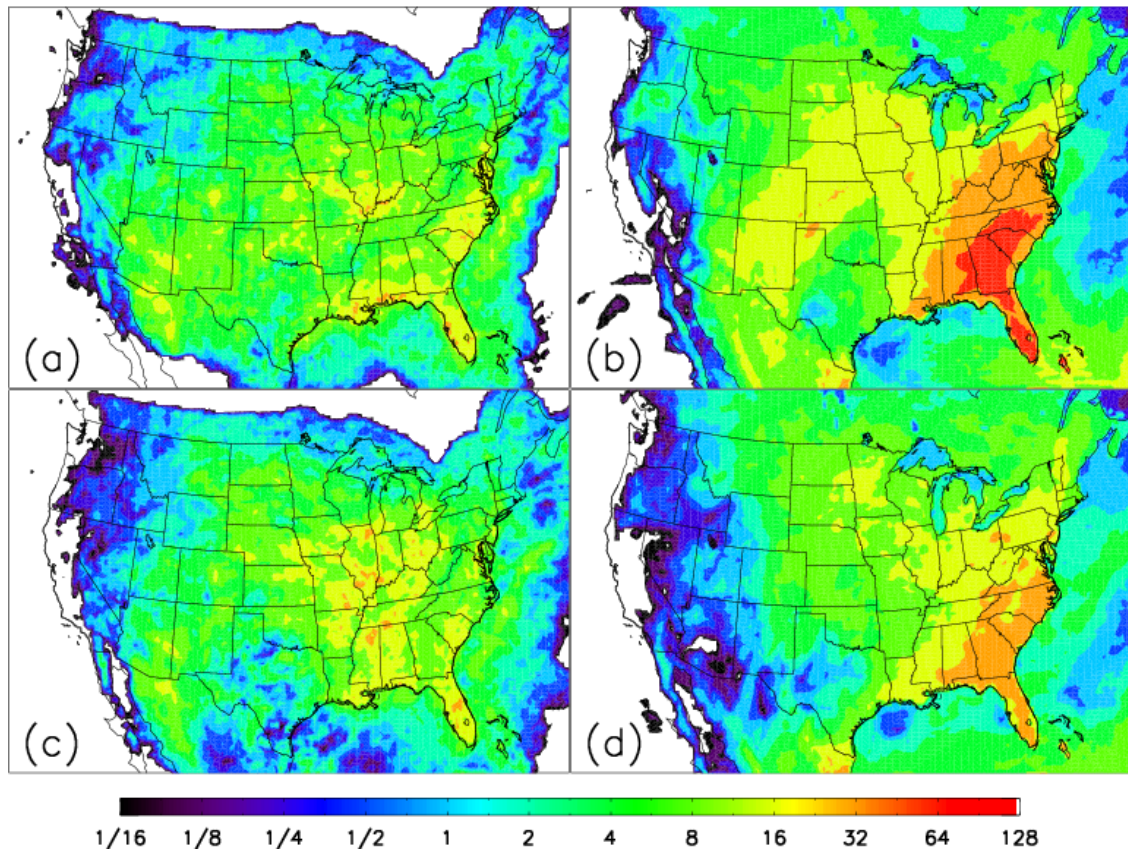


Figure 2.4: Spatial distribution of NLDN and WRF-predicted CG flash counts — Total CG flashes in number per km^2 per full-year during JJA 2006 (first row) and 2011 (second row). First column (**a** and **c**) shows the NLDN observed density gridded to WRF 36 model grid, and second column (**b** and **d**) shows the modeled flash density output by WRF at 36 km.

terization nor specific model setup, but rather to evaluate the performance characteristics of the lightning parameterization when implemented into a regional model with all the expected (and unexpected) defects.

2.2.2 CG flash rate

Figure 2.4 shows the CONUS CG flash density (units in number per km^2 per year). WRF is consistently higher along the East Coast for 2006 where positive bias is also observed in the modeled precipitation, which is used as a proxy for quantifying the comparison of simulated convective strength against observations. Similarly, both flash rate and precipitation are over-predicted in the Colorado and New Mexico region for 2006. On the other hand, the low precipitation bias in Arizona simulated by WRF for 2011 is coincident with a severe low bias in the same region for the CG flash density. Otherwise, flash densities are within the order of magnitude of those observed for regions where simulated precipitation is consistent with NWS observations.

The over-prediction of CG flash density along the East Coast in 2006 dominates the regional mean and produces significantly high biases compared to 2011. Figure 2.5a and 2.5b show the time series of the total number of ground flashes predicted by WRF and observed by NLDN within the analysis region (Fig. 2.1). The me-

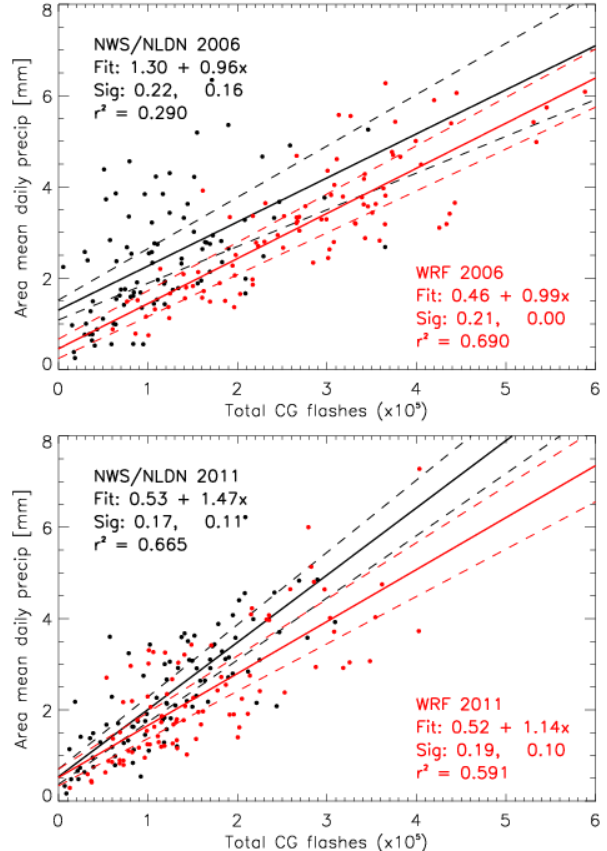


Figure 2.6: **CG flashes vs. precipitation** — Total CG flashes (#) versus area-mean daily precipitation (mm) within the analysis domain (Fig. 2.1). Solid line is the least-square linear fit and dashed lines are $\pm 1\sigma$ for both the constant terms and first-order coefficients. WRF is simulated at 36 km.

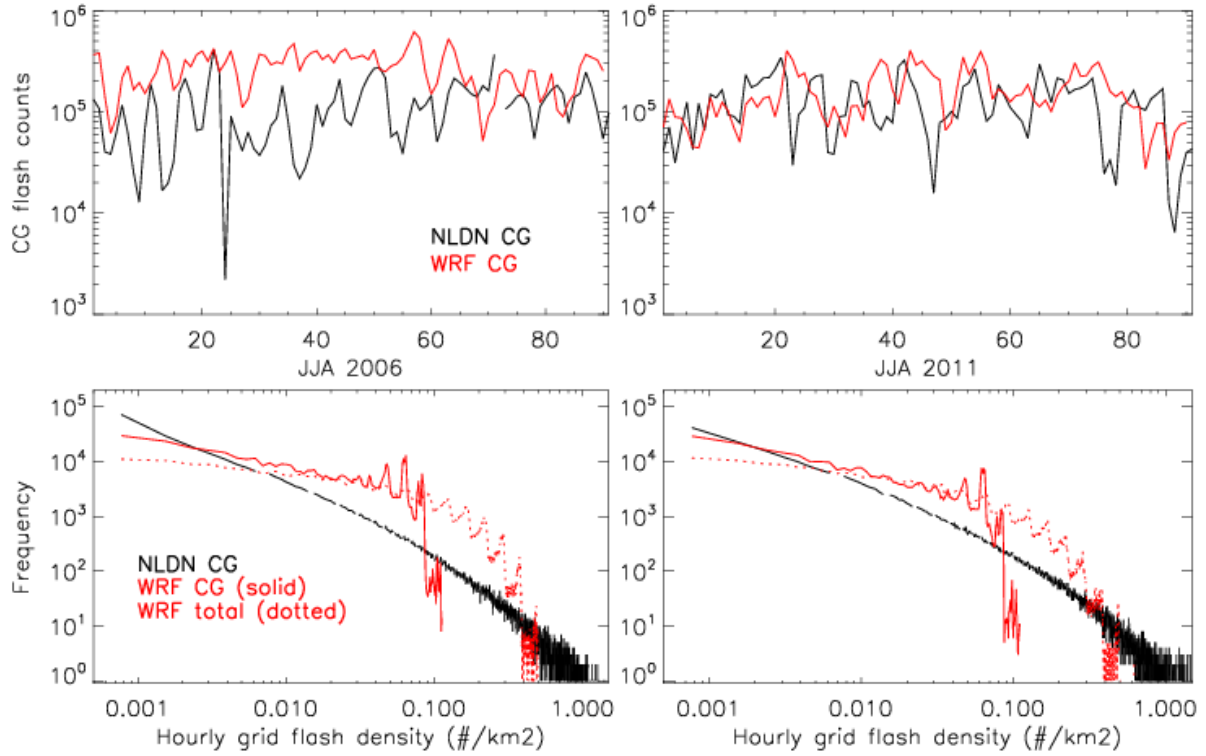


Figure 2.5: **NLDN and WRF CG flash counts** — Comparisons of time series and frequency distributions between NLDN CG flash counts (black) and WRF predicted CG flash counts (red) at 36 km within the analysis domain defined in Fig. 2.1. Total flash counts predicted by WRF are shown as dotted red lines.

dian daily CG bias is 140 % for 2006 and only 13 % for 2011. It should be noted that these values were obtained by sampling all 3 months. Sampling one month would produce varying results. For instance, while JJA 2011 produces an overall median bias of 13 %, July 2011 alone produces about twice as much lightning as observed but is offset by under-predictions in June and August. Because the lightning detection efficiency of NLDN varies spatially, the CG bias can vary over ranges of 116–154 % for 2006 and 1.7–20 % for 2011. The differences between the median biases for the two summers can be attributed largely to the differences in the total precipitation biases, as illustrated in the previous section (Sect. 2.2.1), for which 2006 is 37 % too high while 2011 is only 5 % higher than observations.

To take into account the bias in the simulated convective strength, area-averaged daily precipitation is correlated with total CG flash count. While the relation is likely nonlinear, the area averages over the analysis domain are roughly linear in both WRF-simulated and observed data (Fig. 2.6). The slopes for the 2006 data are statistically the same, there is a constant positive bias for model produced flash counts over observed values. In contrast, 2011 results are close for small values but modeled and observed values diverge for more intense events. Such inconsistency between years demonstrates the potential for strong inter-annual variability in the correlation between flash rate and precipitation.

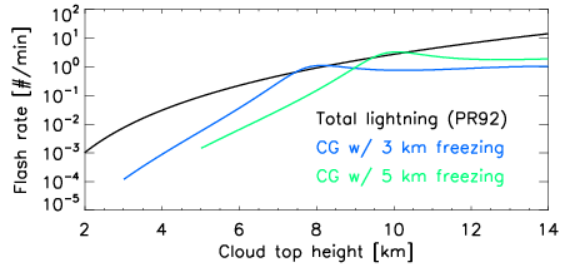


Figure 2.7: **PR92-predicted total lightning as a function of cloud-top** — Total lightning and CG flash rates computed using PR92 and PR93 for various cloud-top heights and freezing levels, demonstrating the source of spectral cut-off in Fig. 2.6.

Figure 2.5c and d show the frequency distributions of the hourly grid flash density. From the spectra, it is apparent that the over-prediction observed in the time series occurs between flash densities of 0.003 to $0.1 \text{ CG flashes km}^{-2} \text{ h}^{-1}$. However, the abrupt cutoff beyond ~ 0.11 in both 2006 and 2011 modeled distribution indicates that PR92 fails to replicate the observed distribution.

The occurrence of this cutoff can be explained by the local maximum when combining the PR92 total flash rate parameterization and PR93 IC : CG ratio parameterization (Fig. 2.7). Together, the predicted CG flash rate is capped at a certain limit, depending on the freezing level regardless of the cloud-top height. In addition, the total flash rate is also under-predicted for high flash rate events (dotted red lines in the figures), thus contributing to the truncated model frequency distribution.

An initial comparison of the model results against the Lightning Imaging Sensor (LIS) total flash data also shows a high bias ($\sim 2.3 \times$) in overall flash count but an underestimation of the high flash count events, similar to the results demonstrated by the NLDN comparison. However, comparisons against the LIS data for this study have a low confidence level because of the relatively short time period simulated and the many uncertainties, such as variable detection efficiency and shifting diurnal sampling bias of LIS data, associated with the analysis.

2.2.3 IC : CG ratio

The JJA 2011 IC:CG bulk ratios ($\equiv \sum_t \text{IC}(\mathbf{x}, t) / \sum_t \text{CG}(\mathbf{x}, t)$) are calculated within the analysis domain (Fig. 2.8a) using constant detection efficiencies of 95 % and 65 % for CG and IC flashes, respectively. While

WRF produced a median IC:CG ratio of 1.74 within the region, ENTLN observed a median of 5.24 with a possible range of 3.80 to 7.17 due to the spatial variability in both IC and CG DEs. Considering the ambiguity in the choice of cloud-top definition described in Sect. 2.1.2, a

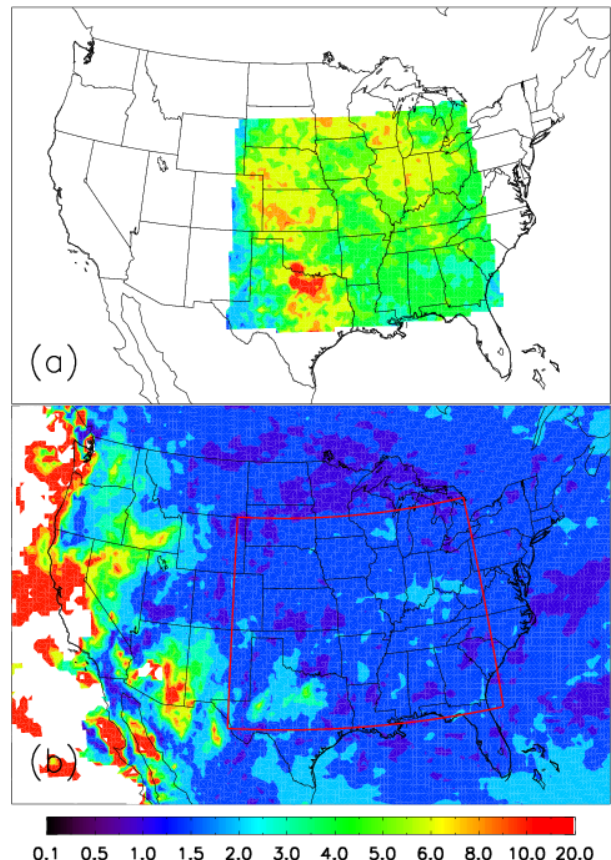


Figure 2.8: **ENTLN and predicted IC:CG bulk ratios** — IC:CG bulk ratios for JJA 2011 as (a) observed by ENTLN and (b) predicted by WRF at 36 km grid spacing using PR93. The ENTLN detection efficiency used here is 0.65 for IC and 0.95 for CG.

possible solution to increase the IC:CG ratio computed using Eq. (2.5), thus achieving better comparison against observations, is by eliminating the cloud-top height reduction, an option that maintains the conceptual interpretation of the parameterization but has the potential of offsetting the bias. For consistency, the cloud-top height used in the total lightning parameterization needs to be un-adjusted as well.

To learn whether reasonable lightning flash rates and IC:CG ratios can be estimated by using just the level of neutral buoyancy (LNB), an offline calculation is made of the daily flash counts with the cloud-top height adjustment eliminated. The offline calculation is performed using instantaneous, hourly model output of LNBs and temperatures (for determining freezing levels). While the offline calculation is able to replicate almost precisely the online flash count prediction, which causes both time series to appear overlapping in Fig. 2.9, the CG flash rate frequency distribution is severely degraded because of vertical discretization of cloud tops to model levels and lowered temporal resolution to hourly outputs. When LNB is used for the cloud-top height (with no adjustment), the prediction of both CG and total lightning flash rates increase, as expected. The CG median bias over ENTLN increases from 44 – 51 % to 158 – 172 %, and the total lightning median negative bias of 53 – 25 % becomes a positive bias of 23 – 95 % for the aforementioned range of DEs. Furthermore, even though the frequency distribution of total lightning is closer to the observed distribution, the CG distribution still experiences the truncation as described in Sect. 2.2.2.

2.3 Resolution dependency

A goal of this study is to evaluate the applicability of the PR92 parameterization to resolutions between fully parameterized and partially resolved convection. Thus, it is useful to evaluate how the parameterization behaves as the grid size changes. To test the behavior of the PR94 calibration factor, a 12 km simulation for July 2011 is used. As grid sizes are reduced to allow convective parameterization to be turned off, the transition to w_{\max} based formulation of PR92 (Eq. 2.2) is tested with a 4 km simulation between 25 July–7 August 2006. The domains for these simulations

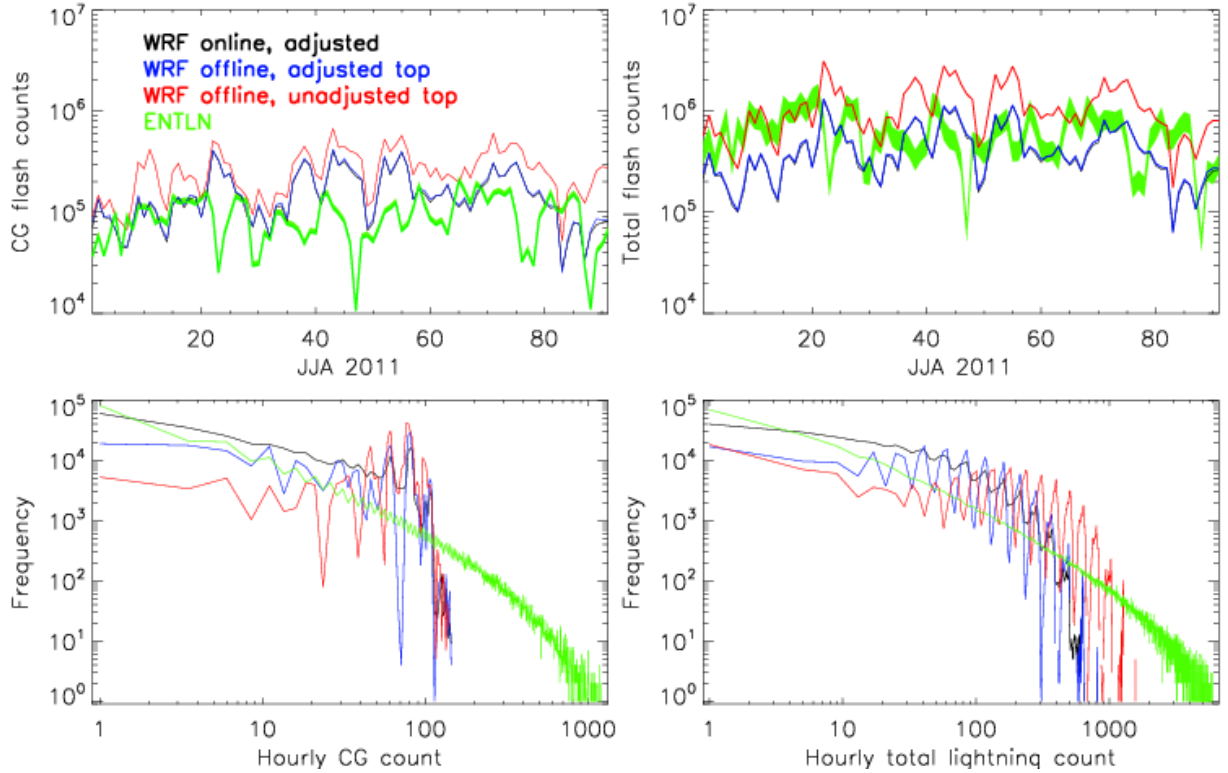


Figure 2.9: ENTLN and predicted total lightning — Comparison of WRF predicted lightning flash counts generated online and offline with and without -2 km cloud-top height adjustments against ENTLN CG and total flash counts. Thicknesses of the ENTLN bands in the time series are computed using the minimum and maximum theoretical IC and CG detection efficiencies within the analysis domain. Noisiness of offline calculated distributions are associated with using hourly outputs only rather than accumulating flashes at every model time step. It should be noted that online (black) and offline (blue) WRF outputs with adjusted top appear coincident in the time series, but are evidently different from the frequency distribution.

are shown in Fig. 2.1. Together, the results from these simulations will provide insights and recommendations on how to achieve resolution-awareness or independence while using PR92.

2.3.1 Sensitivity to grid size

At 12 km, the resolution dependency factor or “calibration factor” (c) from *Price and Rind (1994)* is negligibly smaller (0.56 %) than that applied to 36 km. However, comparison against the 36 km simulation and observations shows that there is a factor of ~ 10 high bias. While there are differences in the statistics of convective strengths between the two simulations, as quantified by precipitation in Sect. 2.2.1, they are too minor to fully reconcile the large bias at 12 km. Therefore, an areal ratio scaling factor ($1/9 = 12^2/36^2$) is applied offline to partially reconcile the differences on top of $c(\sim 1)$, which was applied online.

There are two reasons why the use of areal scaling instead of PR94 is justified in this study. The first reason pertains to why PR94 failed while it has been shown to work in GCMs. The PR94 calibration factor was derived from area-averaged cloud-top heights for progressively larger grid sizes from the original ISCCP 5 km resolution to $8^\circ \times 10^\circ$. On the contrary, the LNBs from the convective parameterization

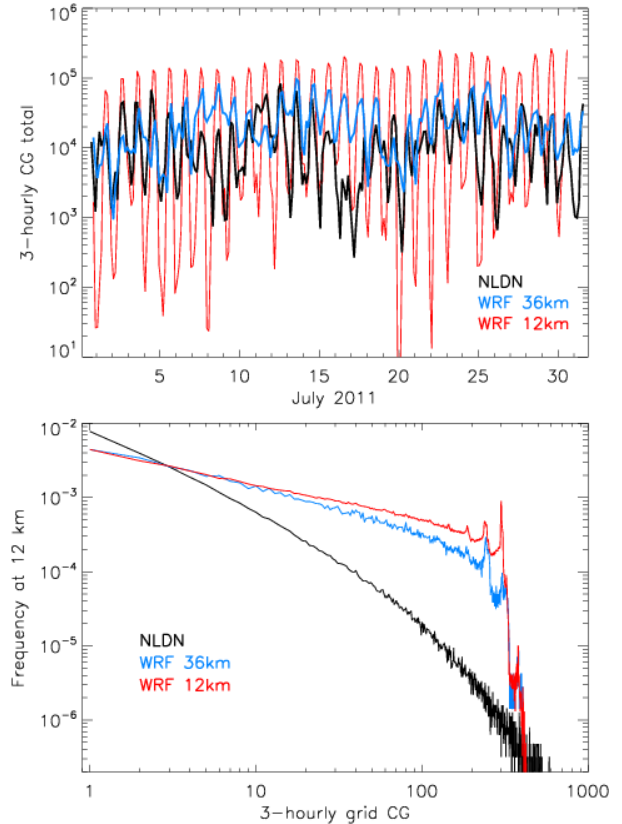


Figure 2.10: Resolution-dependency of lightning prediction — Time series and frequency distributions of 3-hourly CG flash counts compared to NLDN gridded to 12 km. The WRF 36 km distribution is adjusted by $\times 9$ to account for the grid per area difference. The choice of computing the distributions for flash rate per grid as opposed to flash density is to demonstrate the consistency of the spectral drop-off at different resolutions.

are expected to change only slightly with grid resolution as long as the environmental parameters such as buoyancy remain similar.

The second reason addresses why the areal ratio is expected to work for regional scales. PR92 produces flash counts in unit of number of flashes per storm; thus, when approaching almost convection-resolving resolutions, where major storm size is comparable to grid size, the appropriate scaling should be done according to the expected number of convective cores per grid. Since $\Delta x = 36 \text{ km}$ gives a reasonable flash rate compared to observations over 3 months, we assumed one storm per grid at this resolution and scaled the flash counts from $\Delta x = 12 \text{ km}$ as an areal ratio. However, the base case resolution may spatially vary because of the dynamics controlling the minimum-permitted distance between convective cores. At coarse grid sizes, the area covered by the convective storm systems may only be a fraction of the grid cell area. Thus, the area scaling ratio may not be applicable when changing from base-case grid spacing (with approximately one storm per grid) to much coarser grid sizes. A possible solution is to include a cloud fraction estimate as part of the scaling factor between grid sizes.

After scaling by 1/9, WRF at 12 km predicts a median of 40 % more 3-hourly lightning flashes than observed by NLDN (Fig. 2.10). This is to be compared with 36 km, which predicted double the 3-hourly lightning for the same period. Simulating an anomalously strong diurnal cycle in precipitation, the 12 km flash count also shows a much more prevalent diurnal variation, associated with the poor simulation of the diurnal cycle of precipitation as previously noted. Much of the over-prediction is compensated by the negative biases in the nocturnal flash rates in the final statistics. Despite the differences in diurnal skill, the parameterization was able to produce the same drop-off in grid frequency distribution beyond 200 flashes per grid per 3 h, for which the primary cause is discussed in Sect. 2.2.2.

2.3.2 Sensitivity to formulation

Comparing the 36 km simulation to the 4 km simulation provides insight into how the predicted flash density changes between resolutions using $f(z_{\text{top}})$ for parameterized convection and

$f(w_{\max})$ for resolved convective systems. This is an important factor to be considered if flash rate predictions are to be included in nested simulations or models permitting non-uniform grid-spacings such as Model for Prediction Across Scales-Atmosphere (MPAS-A; Skamarock *et al.*, 2012).

The area-averaged daily precipitation predicted by the 4 km WRF-Chem simulation is 70 % too high prior to 2 August 2006 and only 7.5 % too high after 2 August. On 2 August, the 4 km WRF simulation was re-initialized (with no clouds) to be consistent with the re-initializations of the outer domain WRF simulations that drove this 4 km simulation described in Barth *et al.* (2012). The flash rate predicted by the 4 km simulation follows the precipitation trend. A 26 % decrease in flash rate occurs between the period before 2 August and the period afterwards.

While the 36 km simulation over-predicted lightning flash rate for this period (25 July–7 August 2006), the 4 km simulation underpredicted the flash rate, exhibiting a –83 % bias relative to the NLDN flash counts prior to the cold-start and a –95 % bias after (Fig. 2.11). Similar underestimation of the w_{\max} formulation has been noted for both tropical (Hector storm near Darwin, Australia) and US continental storms (Cummings *et al.*, 2013). These results indicate that it is important to evaluate the flash rate parameterizations with observations. It is insufficient to use high resolution model results as “truth” for coarse resolution simulations.

Despite the low bias in flash rate prediction, the 4 km WRF-Chem simulation matches the observed distribution of flashes for high

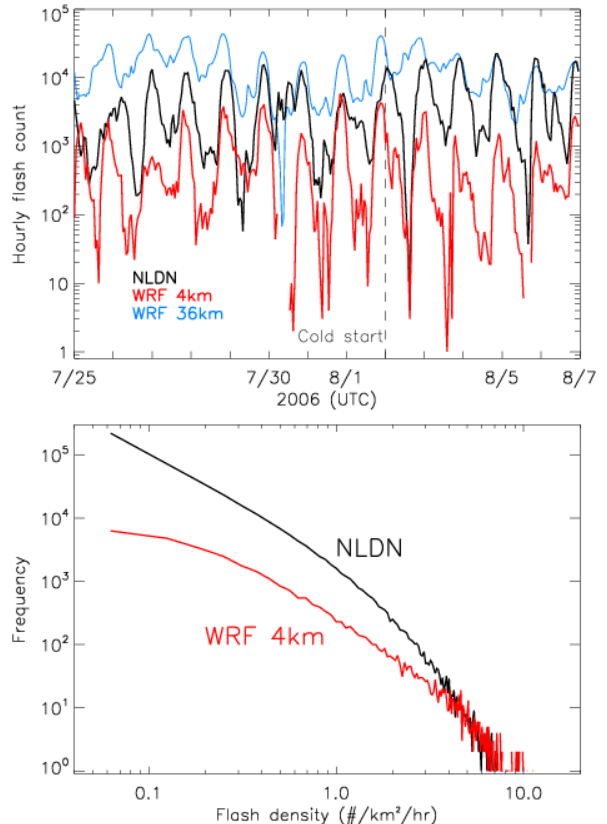


Figure 2.11: Formulation dependency of lightning prediction — Time series and frequency distributions of hourly CG flash counts within the analysis domain as observed by NLDN and simulated by WRF at 4 km grid spacing.

flash rate events and placed the burden of underestimation on the low-end of the distribution, which causes the distribution to appear flatter than observed. Since we are using a constant IC:CG ratio based on *Boccippio et al.* (2001) climatology instead of the PR93 parameterization, the erroneous drop-off in the CG flash rate distribution found in the other cases using PR93 is not present. Such improvement in spectral characteristics suggests that constant climatological IC:CG ratios may be a reasonable if not superior alternative to PR93.

2.4 Conclusions

We have implemented the WRF-Chem model parameterizations for lightning flash rate using prescribed IC:CG ratios and the associated resolution dependency by *Price and Rind* (1992, 1993, 1994), which are based on cloud-top height. In our implementation, the cloud-top height is estimated by the level of neutral buoyancy (LNB), adjusted by -2 km to reconcile the difference between LNB and radar reflectivity cloud top. No additional tunings and changes to the parameterizations are done. The modeled precipitation and lightning flash rate are evaluated for the simulations with 36 km , 12 km , and 4 km grid spacings over CONUS for JJA 2006 and 2011.

The first result is that, after a 2 km reduction, the use of LNB as a proxy for cloud-top simulated at 36 km grid spacing produces CG flash rates at the same order of magnitude as NLDN observations. For models using other convective parameterizations, alternative choices of cloud-top proxies may be available and thus the appropriate methods of cloud-top adjustment should be determined on a case-by-case basis. Taking into account model biases in convection, as quantified by precipitation, the precipitation–lightning relation from the model and observations are statistically indistinguishable. While there is up to a factor of 2.4 median bias in the flash counts from the 2006 36 km simulation, it is accompanied by a 37% over-prediction in precipitation. In contrast, the 2011 36 km simulation has a precipitation bias of 5%, which leads to a 13% over-prediction in flash counts. For the 12 km simulation the lightning flash rate bias is linked to the anomalously

strong diurnal cycle simulated for convection, indicated by precipitation. Such bias in the simulated convection may be caused by a number of other model components.

Second, despite the correct CG count, it is shown that PR92 is incapable of producing the correct frequency distribution for CG flashes, which are truncated at a much lower flash density than observed. The most likely cause is the function form of combining the PR92 total flash rate parameterization and the PR93 IC:CG ratio parameterization, which produces an upper-limit in the permitted maximum CG flash rate. This brings into question the validity of PR93 in contexts where spectra characteristics are a concern. It is recommended that using constant bulk ratios such as the climatology presented in *Boccippio et al.* (2001) or one derived from total lightning measurements may produce equal, if not better, spectra. Considering that the observed JJA 2011 IC:CG ratio also displays significant departure from the *Boccippio et al.* (2001) climatology for certain areas, it would be useful to revisit the subject of IC:CG climatology in future studies, taking advantage of the advances in continuous wide-area lightning detections over the past two decades.

Third, due to the use of LNB from the convective parameterization instead of area-averaged cloud-top heights, using the PR94 factor to adjust for different horizontal resolutions is not applicable and an areal ratio factor should be used instead to reconcile the resolution dependencies. Since the 36 km base cases produced relatively satisfying results, the 12 km simulation is scaled with an areal ratio relative to 36 km. However, it may be argued that the outcome from the 36 km simulations is only a corollary of the probability of having exactly one convective core within a single model grid. Therefore, other choices of “base case” grid spacings near 36 km may also produce similar results for CONUS, specifically within the analysis domain (Fig. 2.1), and other areas with different storm density may require a different base-case resolution for scaling. On the other hand, area ratios may not be appropriate at coarser resolution as convective core number density is highly non-uniform.

Finally, at 4 km, we used a theoretically similar formulation of PR92 based on w_{\max} within convective cores identified as regions with 20 dBZ or greater radar reflectivity. While the parameter-

ization includes the high flash rate storms, thereby giving a frequency distribution shaped similar to that observed without the erroneous drop-off, the flash count is under-predicted by up to a factor of 10. From this experiment, we see the need to evaluate flash rate parameterizations with observations for the locations and periods specific to the simulations. It is insufficient to use high resolution model results as “truth” for coarse resolution simulations. Hence, validation and tuning prior to further usage of $f(w_{\max})$ from Eq. (2.2) is encouraged. Furthermore, parameterizing flash rate in cloud-resolving models based on other storm parameters (*Barthe et al.*, 2010) should also be tested.

To summarize, we recommend the following when applying the Prince and Rind parameterizations for lightning flash rates:

- (1) Proper adjustment to cloud top should be made to match the expected 20 dBZ radar reflectivity top when applying PR92;
- (2) PR93 for IC:CG partitioning should be used only if it is unnecessary to get information on the frequency distribution of flashes;
- (3) Scaling for resolution dependency may be performed by areal ratio against a base-case resolution, defined as that producing 1 storm per grid within the domain of interest (36 km grid spacing in this study).

To further the confidence of the lightning flash rate parameterizations and IC:CG partitioning, long-term wide-area total lightning detection and data archiving should be accompanied by coincident observations of cloud-top or other convective properties with well-defined error characteristics in observations and quantifiable predictability in numerical models.

2.5 Comments on cloud-top height reduction

In this study, we used the level of neutral buoyancy (LNB) from the WRF implementation of the Grell–Devenyi convective parameterization (*Grell and Devenyi*, 2002) as a proxy for sub-grid

cloud-top heights for the purpose of testing a flash rate parameterization by *Price and Rind* (1992, 1993, 1994). A reduction of 2 km is used to reconcile the differences between LNB and the cloud top that would be obtained if defined at a 20 dBZ reflectivity threshold. While this method produces an integrated flash count consistent with that observed after taking into account model biases in convective precipitation, we acknowledge that storm-to-storm variability cannot be captured by such a simple approach. Presented in this section are offline calculations of both 20 dBZ cloud tops and LNB cloud tops from a 13-day simulation at 4 km grid spacing to understand the margin of potential errors.

Radar reflectivity is estimated by using rain, snow, and graupel particle information from hourly outputs. For consistency, the offline calculation of reflectivity uses the same modified equations from *Smith et al.* (1975) and criteria as those used in the 4 km simulation. The highest model level with more than 20 dBZ is then defined as the 20 dBZ top.

LNB is estimated by a simple “parcel method,” rather than emulating the full algorithm in the parameterization as implemented in WRF. Therefore, the result may differ from what would be produced within the model. First, the dew point depression at the surface model level is determined, which is then used to seek the lifting condensation level (LCL) assuming adiabatic ascent. From the LCL, the moist adiabatic lapse rate (Γ_m) is calculated and the level of free convection (LFC) is determined by linearly extrapolating the moist adiabat using the lower level’s Γ_m to the model level immediately above. From the LFC, a search is performed at incremental model levels until the LNB is exceeded. Grid points with LFCs < 500 m or above-freezing temperature at LNBs are discarded.

In total, 1.34×10^6 columns with sufficient reflectivity and cloud-top heights greater than 5 km AGL are found. The distribution of the difference $\langle h_{\text{LNB}} - h_{\text{dBZ}} \rangle$ indicates that LNB is higher than the 20 dBZ top 62 % of the time with a mean of 1.1 km and a standard deviation of 2.3 km. Other metrics for defining the required offsets between the two heights can produce different results. For example, to minimize the bias after applying PR92 with $\left| \langle (h_{\text{LNB}} - \delta h)^5 / h_{\text{dBZ}}^5 \rangle - 1 \right|$, the reduction δh evaluates to 3.27 km. While the 2 km reduction used in this study differs from

the two computed here, it is within the calculated range and thus can still be considered a median representation, especially when the uncertainties in the methods used for the offline LNB and radar reflectivity computations are taken into account.

Finally, it is essential to re-emphasize that the choice of cloud-top reduction is specific to the use of the Grell–Devenyi convective parameterization in WRF or other models producing LNB as the best-available proxy for sub-grid cloud-tops. In other models, cloud-top proxies other than LNB may be present. In those cases, an adjustment specific to those proxies should be used if PR92 is the preferred method for parameterization. An alternative would be to reformulate PR92 to be based on LNB, which lies beyond the scope of this paper and may be attempted in the future as needed.

Chapter 3

2006 North American Monsoon Case Study

The recurring upper tropospheric ozone enhancements during North American Monsoon (NAM) seasons have been extensively studied by *Li et al.* (2005), *Cooper et al.* (2006, 2007, 2009), and *Barth et al.* (2012). Other studies have also highlighted the relevance of this feature (e.g. *Hudman et al.*, 2007; *Choi et al.*, 2009; *Jourdain et al.*, 2010). While previous studies produced results that have been used to infer the climatological impact of the upper tropospheric ozone enhancement on the radiative balance, a closer look at model outputs reveals substantial variabilities. To further the understanding of a chemistry model's capability in capturing the necessary details, this study intends to perform simulations using WRF-Chem (*Grell et al.*, 2005) over July and August of 2006. The period covered by this study is chosen to capture substantial anticyclonic recirculation in the upper-air, which has been shown to enhance ozone production (*Cooper et al.*, 2007).

The case study simulation results are compared against several independent data sets to identify any biases or deficiencies in the model that have implications on the modeled ozone budget. In addition, sensitivity simulations are also performed to evaluate the relative sensitivity of the simulated ozone distributions to emission scenarios of anthropogenic, biogenic, and lightning sources. The results from these simulations are used to bound the range of uncertainty as well as to address the impact from potential changes in emission scenarios in the future.

The first section of this chapter describes the model settings used in this study (Section 3.1). Then, a general description of the model outputs and corresponding validation against various empirical data sets is given in Section 3.2. Once the model's performance has been evaluated,

Section 3.3 describes the core results derived from the base case simulation. Finally, this chapter is concluded with sets of sensitivity tests for determining ozone's variability with respect to lightning-generated NO_x (LNO_x) emissions (Section 3.4.1), anthropogenic emissions (Section 3.4.2), and biogenic emissions (Section 3.4.3).

3.1 Model description

Simulations are performed with the Weather Research and Forecasting model (*Skamarock et al.*, 2008) with Chemistry (WRF-Chem; *Grell et al.*, 2005) version 3.4.1 over July and August, 2006. The model is configured with a horizontal grid spacing of 36 km on a Lambert conformal projection centered over the contiguous United States (CONUS) as shown in Figure 3.1. Vertical levels are discretized on a eta coordinate with a terrain-following surface and a fixed top at 10 hPa.

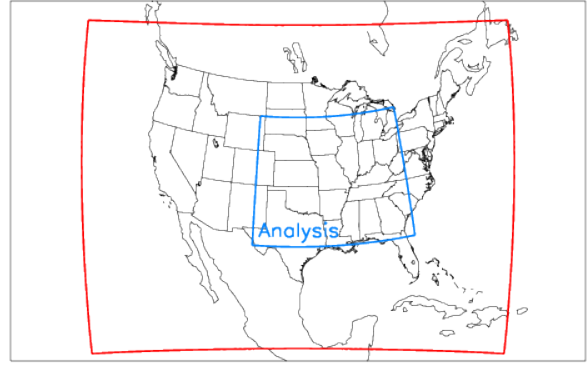


Figure 3.1: 2006 case study model domain — WRF-Chem model domain (red). Marked inner region (blue) is the primary area used for various analysis in Section 3.3.

Meteorology is initialized and assimilated with data from National Center for Environmental Prediction (NCEP) Global Forecasting System (GFS) final (FNL) gridded analysis at 6-hr intervals (00, 06, 12, 18 UTC). Nudging is performed for temperature and water vapor above the planetary boundary layer (PBL). Nudging for horizontal winds is performed above model level 10.¹ Advection of moisture, scalar, chemical, and tracer variables are performed with positive-definite and monotonic limiters described in *Skamarock* (2006).

Descriptions of some of the pertinent model settings and options are given in the following section. The full namelist template for the base case simulation is provided in Appendix B.

¹ At this model level, mean and standard deviation of pressure and height are $843 \pm 55 \text{ hPa}$ and $1.6 \pm 0.6 \text{ km}$.

3.1.1 Model options and parameterizations

For convective parameterization, we use the Grell-3 (G-3) scheme, a modified version of the *Grell and Devenyi* (2002) ensemble scheme. It uses a 144 ($= 3 \times 3 \times 16$) dynamic control and static control/feedback closures with varying parameters. In addition, shallow convection is also enabled to permit less severe convective activities. For cloud microphysics, the *Thompson et al.* (2008b) scheme is used, which allows a generalized gamma distribution for graupel.

Shortwave radiative transfer uses the Goddard two-stream method described by *Chou et al.* (1998) with 11 bands using a δ -Eddington approximation for scattering and transmission. It also takes into account third-order effects from molecular absorption. Longwave radiative transfer uses the Rapid Radiative Transfer Model (RRTM; *Mlawer et al.*, 1997). The NOAH Land Surface Model (*Chen and Dudhia*, 2001) is used for the land surface and the Yonsei University (YSU) scheme (*Hong et al.*, 2006) is used for the boundary layer physics parameterizations.

3.1.2 Chemistry and emissions

The chemical mechanism used in this study is the Regional Acid Deposition Model version 2 (RADM2; *Stockwell et al.*, 1990) compiled with a “WRF-conformed” version of the Kinetic Pre-processor (KPP; *Sandu and Sander*, 2006). KPP uses a Rosenbrock approach, which is a iterative predictor-corrector method described by *Hairer et al.* (1993), to solve the highly nonlinear stiff system of differential equations consisting of 63 species, 21 photolysis, and 136 gas-phase reactions. No aerosol is included in any of the simulations. Photolysis is calculated using the fast Tropospheric Ultraviolet-Visible (FTUV; *Tie et al.*, 2003) scheme. However, there are several implementation errors, which have largely been identified and patched after substantial efforts (see Appendix D.1).

Chemical initial and boundary conditions are obtained from the Model for OZone and Related chemical Tracers (MOZART-4) global chemistry model (*Emmons et al.*, 2010), which includes 85 gas-phase species, 39 photolysis, and 157 gas-phase reactions. Therefore, species mapping is necessary for some of the bulk species (e.g. $OLT := C_3H_6 + MVK + 0.5BIGENE^2$). LNO_x emission

² $OLT =$ terminal alkenes in RADM2; $MVK =$ methyl vinyl ketone, $BIGENE = C_{4+}H_8$ in MOZART-4

uses a modified *Price and Rind* (1992) method described and evaluated in detail in Chapter 2 as well as *Wong et al.* (2013). The base case simulation uses an emission factor of 350 moles NO/flash and vertical distributions described in *Ott et al.* (2010). Further improvements have also been implemented for WRF-Chem version 3.5, released in mid-2013 (Appendix C).

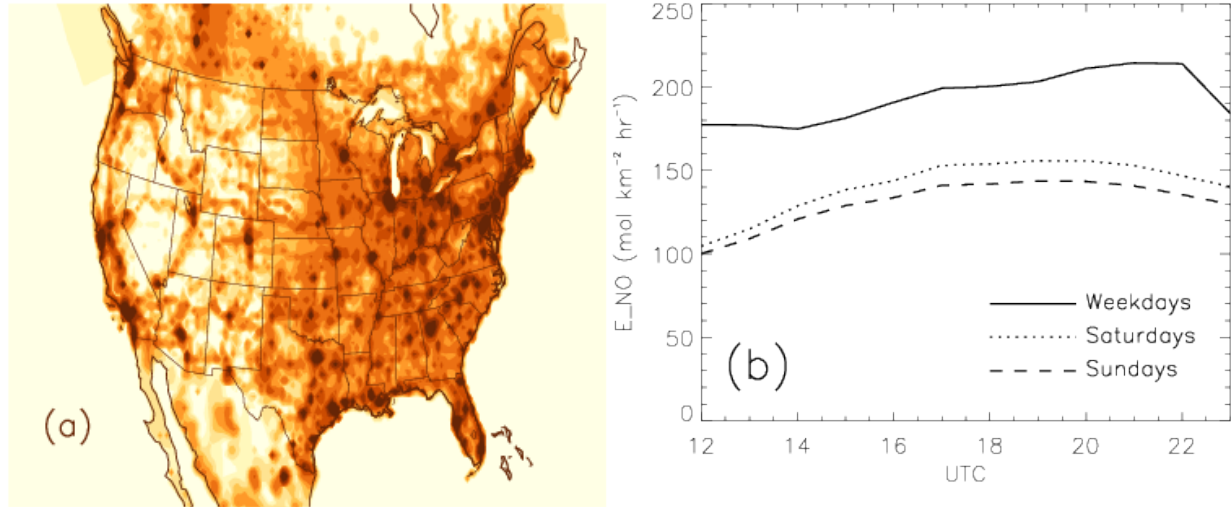


Figure 3.2: **EPA NEI05 NO emission** — (a) NEI05 NO emission during weekdays at 12Z after mapping to WRF grid. (b) NO emission at Houston, TX between 12Z–23Z as an example for demonstrating the differences between emissions for different days of the week.

Anthropogenic emissions

The 2005 National Emission Inventory (NEI05) from the Environmental Protection Agency (EPA) is used to define the anthropogenic emission over CONUS. Three sets of data are separately available for weekdays (Monday – Friday), Saturdays, and Sundays respectively and are swapped in accordingly at 06Z on each simulated day, or 11:00pm to 2am local time depending on the time zone. Figure 3.2 uses NO as an example to demonstrate a typical national emission distribution and differences between days of the week. The utility “*emiss_v03*” provided by NOAA/ESRL is used with the lambert conformal mapping function rewritten to be consistent with that of WRF’s Preprocessing System (WPS) version 3.4.1. The NEI05 source data include CO, NO_x, SO₂, NH₃, 40 hydrocarbon aggregated species, 5 PM2.5 groups, and PM10. Each species is then mapped into its

corresponding counterpart in RADM2. Table 3.1 shows a few examples of how the species mapping is done. Since the case study is performed without aerosols, the aerosol products produced by the utility are not used.

Biogenic emissions

The Model for Emissions of Gases and Aerosols from Nature (MEGAN2; *Guenther et al.*, 2006) is used to drive a biogenic emission parameterization within WRF-Chem. MEGAN2 uses a combination of climatological leaf area index (LAI), vegetation speciation, predicted model temperature, and predicted model solar radiation to compute BVOC emissions consistent with the model meteorological state, of which isoprene is the primary species of interest (see Section 1.1.1).

The general formulation of BVOC emissions is as follow (after *Guenther et al.*, 2006):

$$\text{Emission} = \varepsilon \cdot \gamma \cdot \rho \quad (3.1)$$

where ε is the emission of a compound under standard climatological conditions and is spatially varying, γ is the emission activity factor that accounts for deviation from climatology, and ρ is a factor that accounts for production and loss of the emitted species within the plant canopy, which is fixed at 1.0 in WRF-Chem.

The emission activity factor γ is the product of multiple factors accounting for the canopy environment (CE), age of the vegetations, and soil moisture (SM):

$$\gamma = \underbrace{\gamma_{LAI} \cdot \gamma_P \cdot \gamma_T}_{\gamma_{CE}} \cdot \gamma_{age} \cdot \gamma_{SM} \quad (3.2)$$

Like the production/loss factor, γ_{SM} is set to 1.0 in WRF-Chem. The age factor γ_{age} classifies foliage into 4 types: new, growing, mature, and old, of which the respective weighting is computed using the changes in LAI.

Instead of a detailed canopy model, γ_{CE} is represented as three factors controlled by leaf area (γ_{LAI}), photosynthetic photon flux density (PPFD; γ_P), and temperature (γ_T). Such approach is referred to as the parameterized canopy environment emission activity (PCEEA) algorithm, which

produces annual global isoprene emissions within $\sim 5\%$ of a standard canopy model but may exceed by up to 25% for certain times and locations (*Guenther et al.*, 2006). The temperature factor is highly nonlinear and depends on current and past averages of the leaf temperature:

$$\gamma_T = E_{opt} \frac{C_{T2} \exp(C_{T1} \cdot x)}{C_{T2} - C_{T1}(1 - \exp(C_{T2} \cdot x))} \quad (3.3)$$

$$x = [1/T_{opt} - 1/T] / 0.00831 \quad (3.4)$$

$$T_{opt} = 313 + 0.6 \cdot (T_{240} - 297) \quad (3.5)$$

$$E_{opt} = 2.034 \exp[0.05(T_{24} - 297)] \exp[0.05 \cdot (T_{240} - 297)] \quad (3.6)$$

where T is the leaf temperature in Kelvin, $C_{T1} = 95$ and $C_{T2} = 230$ are empirical coefficients, T_{24} and T_{240} are average leaf temperature over the past 24 and 240 hours respectively. On the other hand, the LAI factor is sublinear:

$$\gamma_{LAI} = \frac{0.49 \text{ LAI}}{\sqrt{1 + 0.2 (\text{LAI})^2}} \quad (3.7)$$

Therefore, the LAI factor is the most sensitive to changes at low LAI and is equal to 1.0 at LAI=5.0.

3.1.3 Tendency diagnostics and passive tracers

Budgeting the tendencies, or attributing changes, of a chemical or aerosol species has been the primary goal of many studies. For air quality studies using limited ground stations, such task has been performed using decomposition methods such as Principal Component Analysis (PCA) a.k.a. Singular Value Decomposition (SVD) (*Langford et al.*, 2009, and references therein). However, PCA relies on the assumption of orthogonality and thus is unable to properly decompose correlated tendencies.

Presented here is a simple method implemented into WRF-Chem since version 3.3. It leverages the deterministic nature of WRF-Chem and extracts the relevant tendencies prior to coupling without loss of information. Conceptualize the tendency calculation of a scalar S from time step t to $t + 1$ as follow:

$$S^{(t+1)} - S^{(t)} = (\Delta_{chem} + \Delta_{conv} + \Delta_{vmix} + \mathbf{v} \cdot \nabla + w\delta_z)S^{(t)}\delta t + E_S^{(t)} + LS^{(t)} \quad (3.8)$$

where Δ 's are the time-stepping operators for chemistry, convective transport, and vertical mixing, \mathbf{v} is the horizontal wind vector, and w is the vertical wind. $E_S^{(t)}$ and $LS^{(t)}$ are the emission and loss terms. Then, we may accumulate at every single time step for a specific process p to obtain the total tendency T for a scalar S due to the said process up to time t from initialization :

$$T_p^{(t)} = \sum_{\tau=0}^t \Delta_p S^{(\tau)} \delta\tau \quad (3.9)$$

While Equation 3.9 appears first-order, the tendencies obtained from each time step are calculated with the accuracy of the respective method used. For example, advection in the simulations employed in this study use a method that has a lower order term and a monotonic limiter described in *Skamarock* (2006). To compute the two advective tendencies, both terms are included into the accumulated diagnostic outputs. Therefore, if $\langle E_S^{(\tau)} + LS^{(\tau)} \rangle_{\tau < t} = 0$, the following is expected to hold with the processes \mathcal{P} from Equation 3.8:

$$\sum_{p \in \mathcal{P}} T_p^{(t)} \equiv S^{(t)} - S^{(0)} \quad (3.10)$$

The default implementation includes 5 processes: chemistry, convection, vertical mixing, horizontal advection, and vertical advection. $T_p^{(t)}$ for 8 species are computed for this study: O₃, CO, NO, NO₂, HO, HO₂, HNO₃, and isoprene. These diagnostic outputs are used extensively throughout this study.

Another subject of frequent interest is the source and age of an air mass. It is often achieved by including online point-sourced tracers or computing Lagrangian trajectories offline with tools such as FLEXPART (*Stohl et al.*, 2005). Of interest in this study are air masses from the boundary layer, stratosphere, lateral domain boundaries, and those affected by LNO_x emission. Values of the lateral boundaries, boundary layer, and stratospheric tracers are held at 1.0 at their sources and allowed to be freely transported through advection, convective transport³ , and vertical mixing. Similarly, lightning tracers are also emitted at the same rate and locations as those determined by the LNO_x parameterization described in Chapter 2, in both passive and decaying form. All decaying twins of these tracers decay with an *e*-folding time of one day. An equivalent mean tracer

³ By sharing the convective transport subroutine with chemical species, an implementation error was introduced. See Appendix D.2 for more details.

age within a volume V may be defined as

$$a_e = (1 \text{ day}) \times \ln \left(\int_V \phi_0 dV / \int_V \phi_1 dV \right) \quad (3.11)$$

where ϕ_0 is the passive non-decaying tracer, and ϕ_1 is the decaying twin. Such definition is chosen over $\int_V \phi_0 / \phi_1 dV$ to avoid cases where $\phi_0 \sim \phi_1 \sim 0$.

3.2 General results and validation

This section describes various aspects of the simulation results and compares them against corresponding observational data sets. The primary goal of this section is to provide context and bounds for uncertainty for further discussions in Section 3.3.

3.2.1 Meteorology

The influence of meteorology on chemistry is of significant importance for the formation of the NAM ozone enhancement (*Li et al.*, 2005; *Cooper et al.*, 2007; *Barth et al.*, 2012). In particular, convection has been shown to detrain boundary layer (BL) air, rich in ozone precursors, into the upper troposphere and thus perturbing ozone distributions (*Dickerson et al.*, 1987; *Kar et al.*, 2004; *Weinstock et al.*, 2007). Moreover, intense convective activities also generate thunderstorms responsible for LNO_x emissions, which accelerates ozone production by supplementing to the NO_x-poor BL air. On the synoptic scale, anticyclonic circulation in the upper troposphere has been attributed to retaining ozone precursors detrained from convection, allowing ozone production above the southern United States over an extended period of time (*Li et al.*, 2005; *Cooper et al.*, 2007).

Precipitation/convection

The primary meteorological feature of interest in this study is convection. While precipitation is not a good measurement of the immediate convective strength, the accuracy and availability of information from the National Weather Service (NWS) Advanced Hydrological Prediction Service

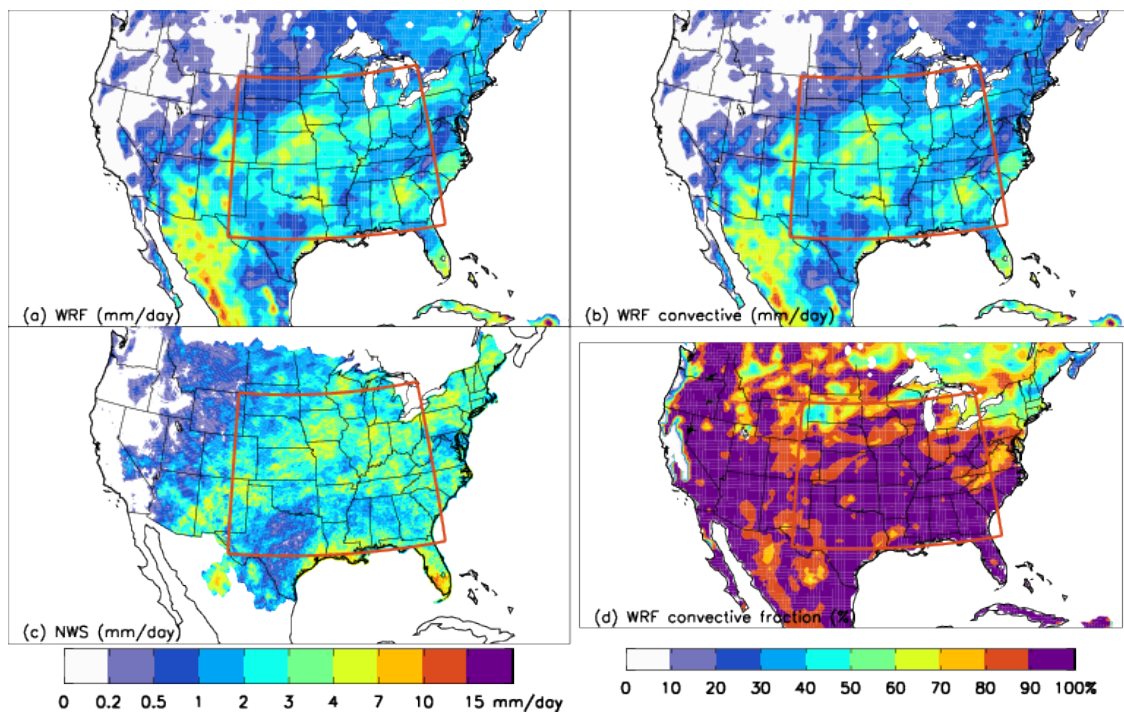


Figure 3.3: **WRF and NWS July and August precipitation** — (a) WRF-simulated total precipitation, (b) WRF-simulated convective precipitation, and (c) total NWS AHPS precipitation in mm/day. (d) Parameterized fraction (%) of model simulated precipitation.

(AHPS) allows continuous validation of the model's prediction. The data product used here is the daily precipitation product from NWS AHPS, a national mosaic product using the combined data from 12 River Forecast Centers (RFCs). Estimation and improvement of observed precipitation from the NWS RFCs are produced by a Multi-sensor Precipitation Estimator (MPE), which combines data from radar and rain gauges across the United States. Post-analyses are also performed manually by NWS forecasters to identify any systematic errors. The resulting data are gridded onto a Hydrologic Rainfall Analysis Project (HRAP) grid with dimensions $4\text{ km} \times 4\text{ km}$ every 24 hours ending at 12 UTC each day (http://www.srh.noaa.gov/abrfc/?n=pcpn_methods).

Figure 3.3 shows a comparison of the spatial distribution of the simulated precipitation amount by WRF and the observed precipitation from NWS AHPS during the July and August of 2006 with Figure 3.3(a) being the total precipitation and (b) being the fraction generated by convective parameterization. Since NWS AHPS does not have coverage over marine regions, WRF outputs have been masked with the land mask. From the figure, the WRF simulation is shown to produce a comparable spatial distribution to NWS, with a high bias at the Arkansas/Texas border and a low bias over Tennessee and Kentucky. Another low bias is located in North Carolina east of the Blue Ridge Mountains. The simulated coastal rainfall north of the Gulf Mexico is also generally lower than observed except for regions near Houston, TX.

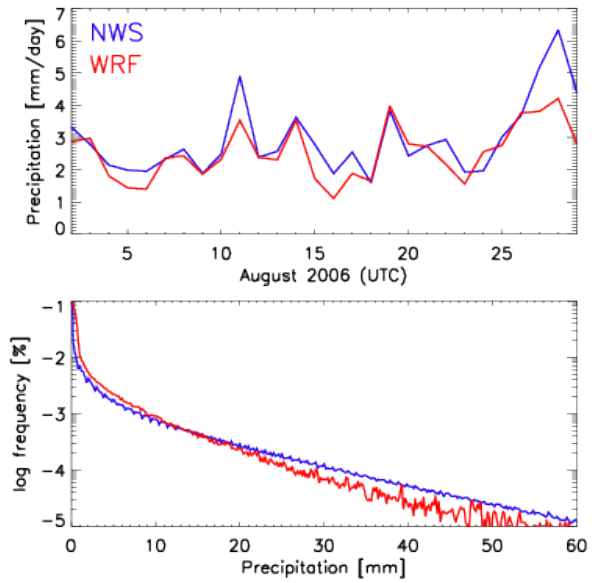


Figure 3.4: WRF and NWS precipitation time series — (a) WRF and NWS daily area mean precipitation within the inner analysis region shown in Figure 3.3 during August 2006. **(b)** Frequency distribution within analysis region with bin size 0.2 mm/day .

During the 28-day period shown in Figure 3.3(a), WRF predicted 71 mm area mean precipitation within the analysis region⁴ while NWS reported 82 mm. This -14% error in precipitation is caused by under-prediction in the frequency of heavy precipitation events above 15 mm/day. A possible cause is that weak convective events have been over-predicted while stronger/grid-scale convective events are underpredicted (Fig. 3.4). Considering the model error in the mean area prediction for individual day, 12 out of 28 days has less than 10% absolute error in the area mean against NWS and 8 out of 28 days are closer than 2% absolute error. An attempt to improve precipitation prediction by reducing the timescale for nudging water vapor to 1 hr instead of 3 hr has instead shown to increase the negative bias to -61% instead. Since the precipitation statistics differ significantly from those in Chapter 2, a separate validation for lightning flash count is performed below.

Lightning

Since LNO_x is a primary upper tropospheric ozone precursor, it is important to understand the model's behavior in terms of lightning prediction. Since total lightning monitoring from ENTLN is not available during 2006, and that LIS/OTD only covers up to subtropical latitudes with variable shifting diurnal-sampling biases, NLDN data is used to evaluate flash rate predictions. Even though Chapter 2 evaluated the lightning parameterization in detail, the change in precipitation statistics

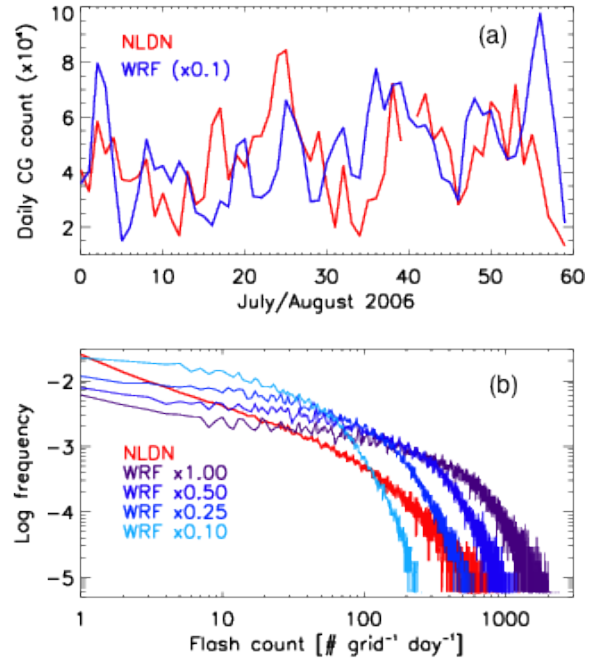


Figure 3.5: **NLDN and WRF CG daily flash count and distribution**—(a) NLDN CG daily flash count ($\times 10^4$) within the analysis region, with WRF-simulated total daily flash count $\times 1/4$ to account for CG fraction and $\times 0.1$ to account for systematic bias. (b) Daily grid flash count frequency distributions from NLDN and WRF with scaling factors.

⁴ Isotropic boundaries defined as 30–40°N, 80–105°W, designed to maximize area coverage without including marine surfaces (minimal NWS data), and the Rocky Mountains (complicated model behavior due to terrain).

with respect to a different nudging parameter and convective fraction demands a separate validation because the statistics of cloud top/level of neutral buoyancy is expected to behave differently as well.

Vaisala⁵ U.S. National Lightning Detection Network (NLDN; *Cummins and Murphy*, 2009) provides continuous multiyear CONUS coverage of > 90% of all CG flashes with ongoing network-wide upgrades since 1984 (*Orville et al.*, 2002, 2010). It is also part of the North American Lightning Detection Network (NALDN), which includes the Canadian Lightning Detection Network (CLDN). Data from NALDN comprise a part of Vaisala's GLD360 global lightning product, which is not used in this study. The network employs the "Improved Accuracy through Combined Technology" (IMPACT) algorithm, which combines direction finding (DF) and time-of-arrival (TOA) information from lightning position and tracking system (LPATS) sensors and IMPACT sensors. The frequency range at which the sensors operate allows detection of primarily CG flashes and a small number of IC flashes. Low peak current strokes < 15 kA are eliminated from the data set due to potential misclassification. The median location accuracy is 250 m, which is well within the model grid size used in this study and thus may be considered negligible. Multiple strokes are aggregated into a single flash if they are within 1 second and no more than 10 km apart.

Since NLDN detects only CG flashes and WRF-Chem produces total flash counts⁶, flash count outputs from WRF is scaled by 1/4, or an IC:CG ratio of 3 : 1, to account for a rough estimate of the CG fraction in the area according to *Boccippio et al.* (2001) and consistent with IC:CG ratio from ENTLN shown in Figure 2.8. Despite precipitation being underestimated, the simulated CG flash count is approximately 10 times higher than observed by NLDN, which is within the order-of-magnitude variance according to Chapter 2.

Figure 3.5a shows the comparison of the daily flash count from NLDN and WRF-Chem after scaling for the systematic bias. However, even though scaling by $\alpha = 0.1$ allows the integrated flash count to be consistent with observation, the distribution truncates prematurely at

⁵ Vaisala acquired NLDN from GeoMat between 2002 and 2003.

⁶ The version used in this study is 3.4.1, which produces an aggregated IC+CG flash count. Estimation of IC:CG ratio is implemented into WRFV V3.5, described in Appendix C.

~ 200 flashes/grid/day and compensates the deficit with overestimations below 100 flashes/grid/day (Fig. 3.5b). Due to the nonlinear response of ozone chemistry to LNO_x, such adjustment is expected to have unrealistic impacts on the ozone production. Sensitivity tests designed to address these uncertainties are described in Section 3.4. For the base case scenario, the default setup ($\alpha = 1.0$) is used even though excess LNO_x is expected. This decision is made because there is no clear evidence to support that the suggested alternatives can produce significantly better results until sensitivity tests are performed.

3.2.2 Ozone

Given the result from the previous section (Sec. 3.2.1), we can expect to see excess tropospheric ozone provided NO_x-titration does not precede ozone production. Since the ozone enhancement occurs primarily above the southern United States, it is useful to define a region of focus different from that used in Section 3.2.1. Consider the August mean geopotential height (\bar{Z}_{300}) at 300 hPa simulated by the model, we define the “anticyclone region” as columns with $\bar{Z}_{300} > 9730$ m. While the anticyclonic circulation is not stationary, using the mean circulation maximizes the duration during which characteristics of the ozone enhancement can be captured.

Both the August mean 300 hPa ozone and geopotential heights are shown in Figure 3.6. The location of ozone enhancement is consistent with that observed by *Cooper et al. (2007)*. The ability to position the enhancement only requires the correct dynamical features such as the anticyclone

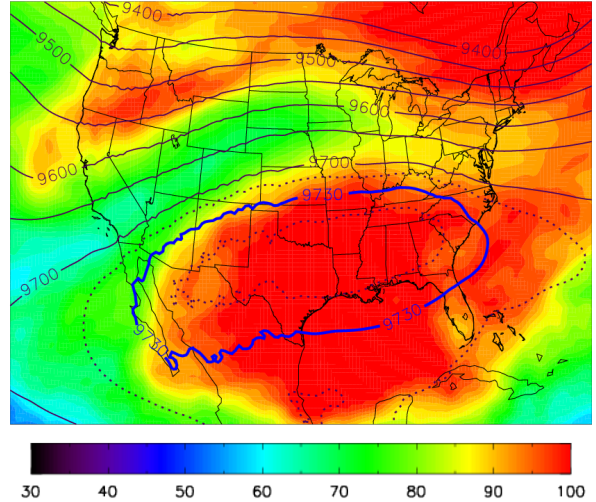


Figure 3.6: **Simulated upper tropospheric ozone** — Simulated ozone (ppbv) and geopotential height (m) at 300 hPa averaged for August 2006. The blue 9730 m geopotential height contour indicates the “anticyclone region” that is used throughout Chapter 3. This figure can be compared to those in *Cooper et al. (2007)*.

formation, which is controlled by data assimilation with NCEP GFS inputs. North of the jet stream, stratospheric ozone appears as consistent high ozone. High ozone VMRs are observed to be mixing across the jet stream in the outflow region (northeast corner of model domain) and circulates into the anticyclone. The finger-shaped low-ozone structure over California separating the ozone enhancement core and northern stratospheric ozone is formed by repeated low-ozone transport from the equatorial Pacific via the southwest corner boundary condition provided by the MOZART global CTM. Nonetheless, compared to the other studies, the magnitude of the simulated ozone enhancement is higher by about 20 ppbv and slightly more widespread especially over the Gulf of Mexico. This can be attributed to the order of magnitude over-prediction of lightning flash rate and thus LNO_x (see Sect. 3.2.1).

Validation against TES

To quantify the bias in the simulated ozone, retrievals from the satellite-borne Tropospheric Emission Spectrometer (TES) are used to provide spatial snapshots along selected transects. TES is a high resolution infrared Fourier-transform spectrometer with a spectral resolution of 0.06 cm^{-1} (Beer, 2006). The data products used are of V004, all of which are special observations in step-and-stare mode with footprints of $5.3 \text{ km} \times 8.3 \text{ km}$ and 35 km gaps between stares. Through comparisons with ozonesondes, a validation with V002 showed that TES ozone had a 3–10 ppbv high bias in the troposphere, but it is still able to pick up the general variability (Nassar *et al.*, 2008). TES products have been used in numerous studies on tropospheric

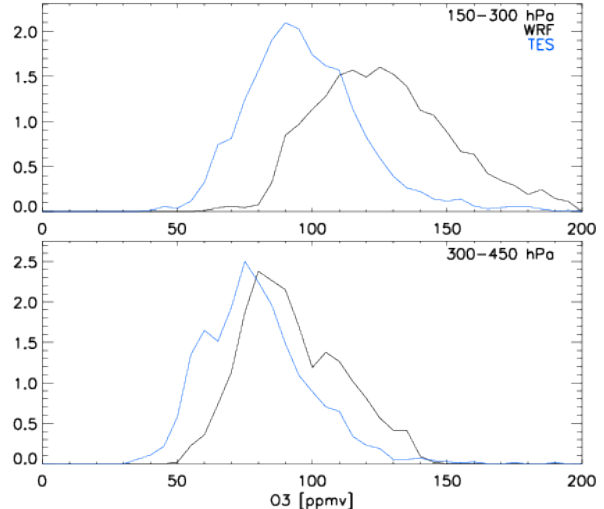


Figure 3.8: WRF-Chem and TES ozone frequency distributions — Normalized frequency distributions (%/ppmv) of TES and WRF-Chem ozone mixing ratios between (a) 150–300 hPa and (b) 300–450 hPa. Only columns between 25–40°N are used.

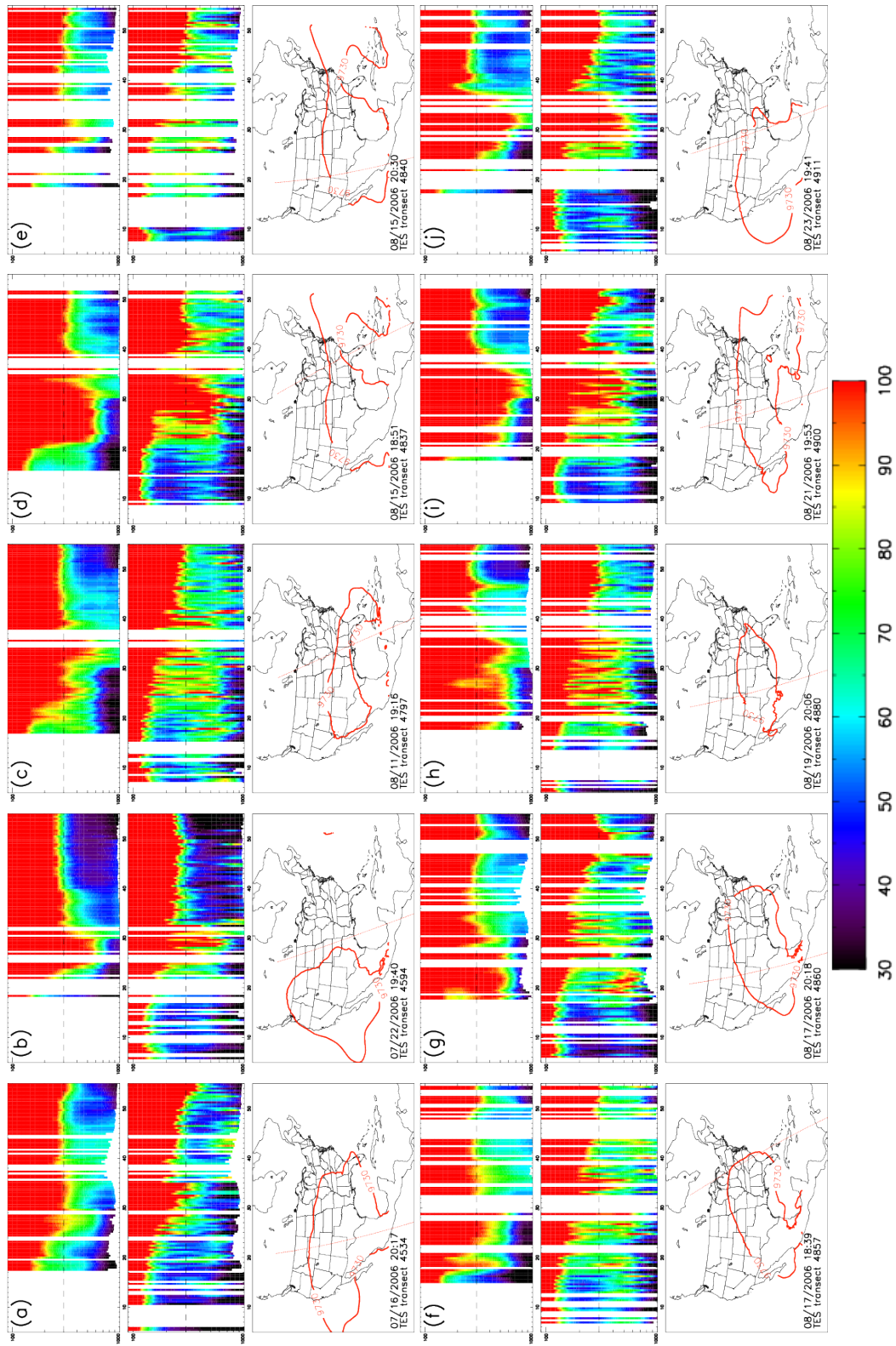


Figure 3.7: **TES/WRF Ozone comparisons** — First row for each panel is the WRF-Chem ozone profiles in ppbv mapped onto TES pressure coordinates after applying Equation 3.12. Second row is the TES profile. Horizontal dashed line indicates the 300 hPa level. Third row shows the TES transect and the 9730 m geopotential contour at 300 hPa from WRF. Time indicated is the 30°N-crossing time in UTC.

chemistry (e.g. *Hegarty et al.*, 2010; *Voulgarakis et al.*, 2011), studies on convection and water budget (e.g. *Brown et al.*, 2008; *Risi et al.*, 2010), and air quality studies (e.g. *McMillan et al.*, 2010; *Wang et al.*, 2011).

Using TES, we first compare the ozone curtain profiles. Between July 15 and August 23, 10 TES transects are selected and compared to the WRF-Chem output of the corresponding date at 18 UTC or 21 UTC, whichever is closer to the 30°N-crossing time (Fig. 3.7). These transects are selected because they either (a) show signals of upper tropospheric ozone enhancement, or (b) intersect regions with 300 hPa geopotential height greater than 9730 m while passing over the United States. Of the ten transects, only transect 4594 does not satisfy criteria (b), but the TES retrieval does show a prominent upper tropospheric ozone enhancement just south of 30°N. In addition, to compare model outputs against TES profiles, proper transformation of the model profile is required. Let \mathbf{x}_{WRF} be the log of ozone column vector extracted from WRF-Chem and interpolated onto TES pressure levels, then the averaging kernel is applied as follow:

$$\mathbf{x}_{\text{WRF}}^{\text{TES}} = \mathbf{x}_a + \mathbf{A} (\mathbf{x}_{\text{WRF}} - \mathbf{x}_a) \quad (3.12)$$

where \mathbf{x}_a is the *a priori* constraint, \mathbf{A} is the averaging kernel, and $\mathbf{x}_{\text{WRF}}^{\text{TES}}$ is how TES would observe the WRF-Chem ozone column. Furthermore, columns with potential problems are filtered out using the master quality assurance flag, the C-curve flag⁷, and the criteria⁸ that $\text{trace}(\mathbf{A}) > 4.0$.

Figure 3.7 shows the WRF-TES comparison along TES transects. Qualitatively, the height of the 100 ppbv ozone isopleth is well simulated north of 30°N. South of 30°N, upper tropospheric ozone is often over-predicted. These over-predictions occur either within Mexico, where the terrain of the Sierra Madre triggers frequent large-scale thunderstorms, or the Gulf of Mexico, where LNO_x marine emission is unconstrained. As an example, transect 4911 (Fig. 3.7j) is able to capture the ozone enhancement between 28–47°N, followed by a ridge-like low-ozone structure at 40°N attributable to low ozone air masses transported from the equatorial Pacific. South of 28°N, where the transect was passing over the Gulf of Mexico, WRF-Chem is biased high with the 100 ppbv

⁷ The C-curve flag filters out retrievals with anomalously high surface ozone (*Zhang et al.*, 2010)

⁸ $\text{trace}(\mathbf{A})$ is sometimes known as the degrees of freedom for signal.

ozone isopleth reaching 500 hPa while TES observed only 70–90 ppbv up to 150 hPa. Similar high biases are also seen for transects 4837 (Aug 15, Fig. 3.7d) and 4900 (Aug 21, Fig. 3.7i).

Comparing the upper tropospheric and mid-tropospheric ozone distribution, Figure 3.8 clearly shows that WRF-Chem simulates higher ozone than observed by TES. Between 150–300 hPa and 25–40°N, WRF simulated a mean ozone mixing ratio of 123.7 ppbv with a standard deviation of 25.8 ppbv after applying the TES averaging kernel. In contrast, TES observed 98.0 ± 17.2 ppbv. Therefore, WRF-Chem simulated a 21% higher concentration of ozone within the ozone enhancement than observed. The larger standard deviation from WRF-Chem also means that the simulated distribution has a higher heterogeneity or less well-mixed. In the mid-troposphere, the WRF-Chem simulated and TES observed statistics are 102.1 ± 26.5 ppbv and 84.8 ± 18.3 ppbv respectively.

Validation against IONS-06

The above validation against TES shows that while ozone is overestimated, the existence of the ozone enhancement and its location is well-simulated. Some drawbacks for using TES are the results' dependencies on *a priori* and their sparse temporal resolution. To complement the validation against TES, we use ozonesonde profiles taken during the INTEX-B Ozonesonde Network Study of 2006 (IONS-06; *Thompson et al.*, 2008a). During this campaign, 410 ozonesondes were launched from 14 sites strategically positioned to represent major sources, sinks, and pathways of tropospheric ozone in North America. These sondes used electrochemical concentration cell (ECC) sensors that have precision within $\pm(5\text{--}10)\%$ in the troposphere (*Smit et al.*, 2007). Between different models of the instruments, measurement biases due to variation in potassium iodide (KI) sensing concentration may be of the order of 2–3% (*Smit et al.*, 2007). Data from this campaign and its predecessor, IONS-04, have been used to support studies on continental tropospheric ozone distribution (*Cooper et al.*, 2007), inferring local ozone sources (*Thompson et al.*, 2008a), and comparisons with air quality model output (*Tarasick et al.*, 2007) and satellite retrievals (*Nassar et al.*, 2008).

Ozonesondes launched during August within the model domain (Table 3.2) are compared against WRF-Chem ozone columns on WRF-Chem model grid. As an example, comparison at Huntsville, Alabama is shown in Figure 3.9. Despite the prevalent over-prediction of ozone concentration throughout the entire troposphere, the timing of the occurrences of upper tropospheric ozone enhancement episodes correlate well with ozonesonde measurements. Specifically, “termination” of the first enhancement on August 11 followed by a drop in ozone throughout the entire column is seen in both WRF-Chem output and the ozonesonde profile. Similarly, the “termination” of the second enhancement on August 23/24 is also simulated. These events are likely caused by the synoptic movement of the enhancement, controlled by dynamical features. Except for Kelowna, British Columbia, the simulated ozone VMR above 200 hPa is a factor of 2–3 or higher at all North American ozonesonde sites within the model domain (not shown).

In conclusion, WRF-Chem is able to simulate an upper tropospheric ozone enhancement that coincides with the “anticyclone region” defined earlier, but the overall ozone VMR is overestimated throughout the tropospheric column. Despite the high bias, spatiotemporal variabilities controlled by large-scale dynamics are observed at individual locations affected by the ozone enhancement. Except for the three North America West Coast locations, surface model levels, and above 200 hPa, tropospheric high bias rarely exceeds 100% ($\times 2$).

3.2.3 Carbon monoxide

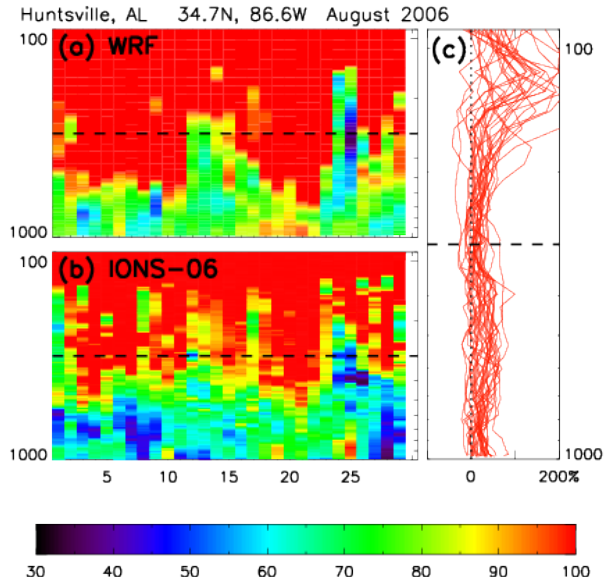


Figure 3.9: **IONS-06 Huntsville launches** — WRF-Chem ozone verticle profiles during August IONS-06 ozonesonde launches at Huntsville, Alabama and the relative bias against the measured ozone mixing ratios. Horizontal dashed lines indicates the 300 hPa levels in each panel.

To understand the ozone bias, it is useful to look at its chemical precursors. Carbon monoxide (CO) is widely used for tracking boundary layer air and pollution (e.g. *Pan et al.*, 2007; *Weinstock et al.*, 2007; *McMillan et al.*, 2010). Emitted through incomplete combustion, CO is an excellent indicator for anthropogenic emission sources and biomass burning. It is also produced chemically through OH oxidation of a wide range of VOCs. Furthermore, its 2–3 month lifetime in the troposphere allows CO to be an effective long-range tracer without being well-mixed.

Figure 3.10 shows the August average CO mixing ratio at 300 hPa. At the center of the NAM circulation is a distinct CO maximum over northeastern Texas. This feature is a combination of tracer retainment via NAM circulation and local convective detrainment of boundary layer air. Considering the comparison performed for precipitation in Section 3.2.1, this feature may be weaker if not absent due to the high bias in convective activity in that region. On the other hand, the high CO simulated over Georgia and neighboring states may have been underestimated because of the under-prediction in convective activity along the Blue Ridge Mountains. North of the jet stream, anomalously high CO is observed near the tropopause transported from the western boundary condition defined by MOZART. This influx of CO in the upper air can be linked to intercontinental transport of widespread wild fires across the Siberian plateau during July. Consistent with the transport pattern of northern high ozone, which is occasionally seen splitting off across the jet stream and transporting southwards along the Atlantic coast and eventually merged into the “anticyclone,” high CO from north of the jet stream is also observed to follow the same transport pattern. Finally, air mass with low CO and low ozone are transported intermittently into

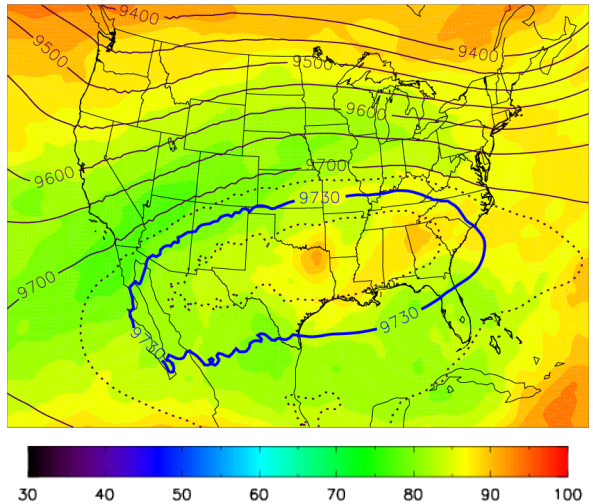


Figure 3.10: Simulated upper tropospheric CO — Carbon monoxide (ppbv) and geopotential height (m) at 300 hPa during August 2006.

the domain via the southwestern boundary and into the inner CONUS between the 9600 m and 9700 m isohyps.

Validation against TES

To evaluate the validity of the model's CO output, we compare WRF-Chem results against TES CO products. The instrument characteristics of TES are already described in Section 3.2.2. The TES CO product has been validated against MOPITT⁹ satellite retrievals (Luo *et al.*, 2007a; Ho *et al.*, 2009) and aircraft measurements (Luo *et al.*, 2007b; Lopez *et al.*, 2008). To summarize, TES CO products show slightly lower column CO values compared to MOPITT and a ±10% bias relative to in-situ measurements with the primary contribution being smoothing errors and dependency on the a priori. Except for instances of poor spatiotemporal coincidences, correlation coefficients between in-situ measurements and TES retrievals are between 0.61 and 0.92. Therefore, while retrieval values may be biased, the relative variabilities of CO are expected to be realistic.

The TES CO product is often utilized in tandem with the TES O₃ product. Logan *et al.* (2008) used these two products to investigate the impact of El Niño on tropospheric composition. Similarly, Voulgarakis *et al.* (2011) used them to investigate the global O₃-CO correlation. Attempts have also been made using the two TES products to characterize urban pollution outflow but was criticized for low sensitivity near the boundary layer as indicated through its averaging kernel (Shim *et al.*, 2007). In the following validation exercise, we compare only WRF-Chem's output to the TES CO prod-

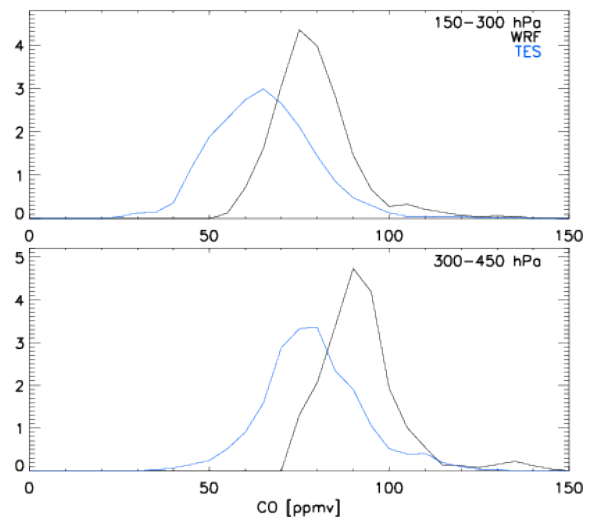


Figure 3.11: **WRF-Chem and TES CO frequency distributions** — Same as Figure 3.8 except for carbon monoxide.

⁹ Measurements of Pollution in the Troposphere.

uct using the procedure outlined in Equation 3.12 to mirror the comparison done with ozone in Section 3.2.2. Further analysis pertaining to O₃-CO correlations will be revisited in Section 3.3.

Figure 3.12 shows the transect-by-transect comparison of WRF-Chem CO mapped onto TES transects against TES CO products. WRF-Chem is obviously biased high in the mid-to-upper troposphere. There are two possible causes for a high bias in CO. The first being an underestimation of the loss rate, governed by dry deposition and chemical losses via CO + OH, which may be subsequently attributed to photolysis as OH is primarily controlled by the photolysis rate $J(O_3)$. The second possible cause is an overestimation of boundary layer air detrainment. Even though precipitation has been under-predicted (Sect. 3.2.1), there is substantial over-prediction in the frequencies of light precipitations events of < 15 mm/day (Fig. 3.4).

While there is a high bias in the upper troposphere connected to convective transport, there is a low bias at northern latitudes at lower-to-mid levels. A source for these low biases is the lack of biomass burning emission via wildfire events and thus the related plume-rise vertical transport. Using the fire products from the Moderate Resolution Imaging Spectroradiometer (MODIS; *Justice et al.*, 2002), several enhanced CO plumes in the TES transects can be identified as fire related. On July 16, transect 4534 (Fig. 3.12a) captured a wildfire at Soda Creek, WY (43.5°N, 110.2°W). On August 15 and 17, multiple transects (Fig. 3.12e–g) captured the downwind plumes of widespread fires from Oregon as heightened CO signature between 46–53°N. Finally, transect 4911 captured the plume from the Idaho fires on August 23 (Fig. 3.12j). Therefore, excluding the influence of wildfire emission, WRF-Chem is almost always biased high.

Considering only data between 25–40°N, the frequency distributions between WRF-Chem and TES retrievals are shown in Figure 3.11. The computed mean values for the upper tropospheric distributions are 81.7 ppbv and 67.7 ppbv for WRF-Chem and TES respectively, and thus WRF-Chem is 20.7% too high. In addition, the standard deviations of the distributions are significantly different with 11.7 ppbv for WRF-Chem and 14.3 ppbv for TES. In other words, WRF-Chem is more well-mixed than TES. In the mid-troposphere, the mean VMRs are 94.6 ppbv and 81.3 ppbv, thus WRF-Chem is 16.3% higher. Similar to the upper troposphere, the standard deviations also

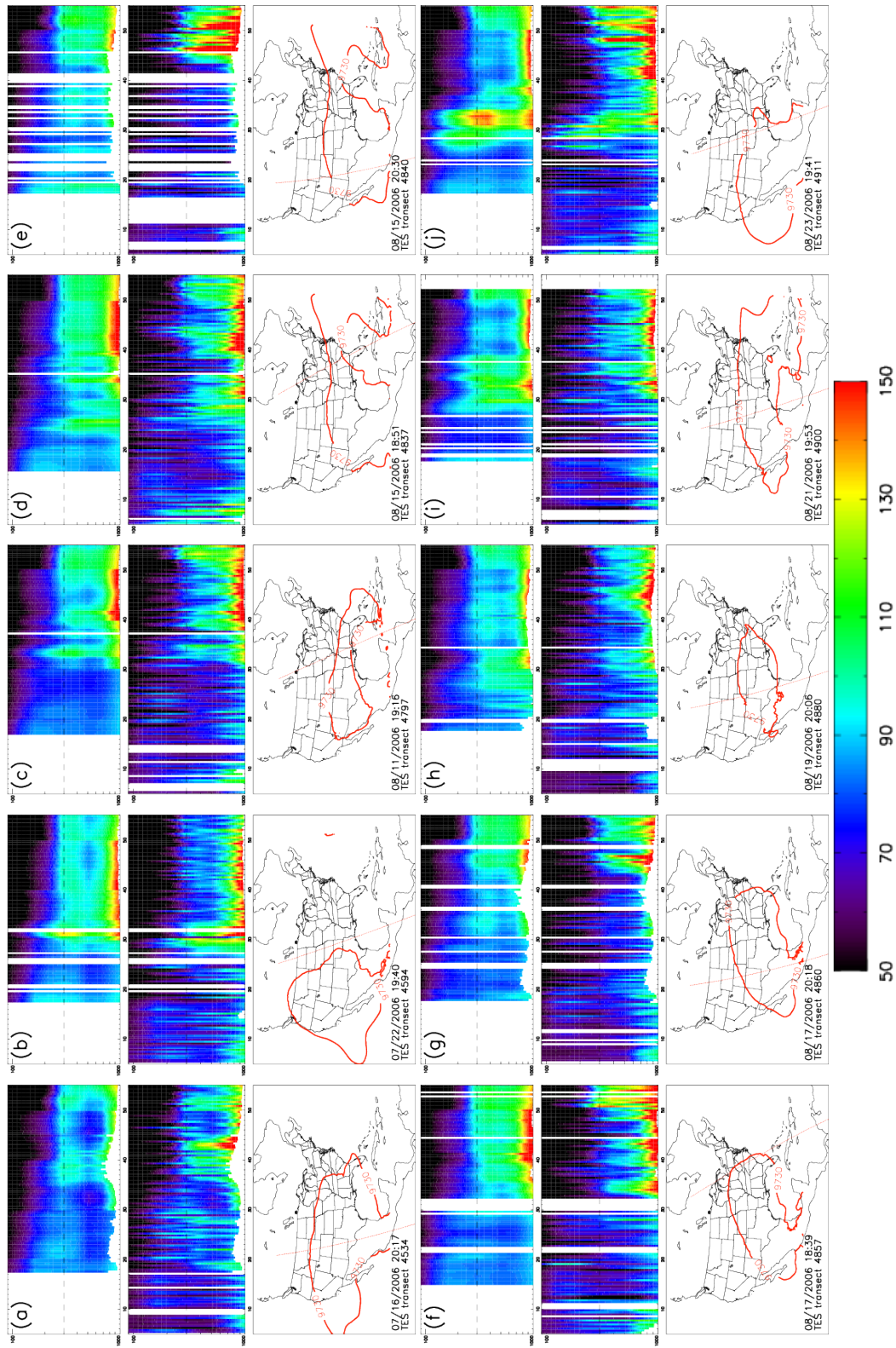


Figure 3.12: TES/WRF CO comparisons — Same as Figure 3.7 except for carbon monoxide.

show that WRF-Chem is more well-mixed. It is worth noting that the disparity in CO spatial heterogeneity between WRF-Chem and TES is surprisingly consistent with the validation done by *Barth et al.* (2012) despite the differences in mean VMR bias and targeted pressure level.

There are at least three possible causes for these biases. The first being wildfire plumes, which intermittently introduce outliers in the TES distribution but not in WRF-Chem's. Another cause, which is debatable, may be that of a longer residence time for CO in WRF-Chem than the actual value. Given the excessive $J(O_3)$ (Apdx. D.1), it may be hypothesized that OH is underestimated and excess LNO_x is responsible for consuming too much HO_x to form various reservoir nitrogen species such as HNO_3 and $HONO$. The model biases in NO_x will be discussed in Section 3.2.5. Finally, a TES transect has a 7.5 mrad or 5.3 km cross-track Field of View (FoV), which is to be compared with the 36 km grid spacing in WRF-Chem. Therefore, TES observations are highly susceptible local variabilities and outliers.

Validation against MOPITT

Measurements of Pollution in the Troposphere (MOPITT) is a satellite-borne instrument with the primary mission of measuring tropospheric CO. MOPITT is a multi-channel gas correlation radiometer (*Drummond and Mand*, 1996). It uses a maximum a posteriori (MAP) algorithm for retrieval (*Deeter et al.*, 2003). It has a horizontal resolution of 22 km \times 22 km and 7 pressure levels. Improvements to the forward model such as consideration of variability in modulation cell pressure are incorporated in version 4 (*Deeter et al.*, 2010). This study uses version 5, which has been validated by *Deeter et al.* (2013). After accounting for the different retrieval methods, and consequently different a priori and averaging kernels, MOPITT produces roughly the same CO volume mixing ratio and column density as TES within $\pm 15\%$ (*Luo et al.*, 2007a). Though having lower spatial resolution, MOPITT offers slightly higher sensitivity than TES close to the boundary layer and a larger FoV, which complements the CO products from TES with valuable cross-track information.

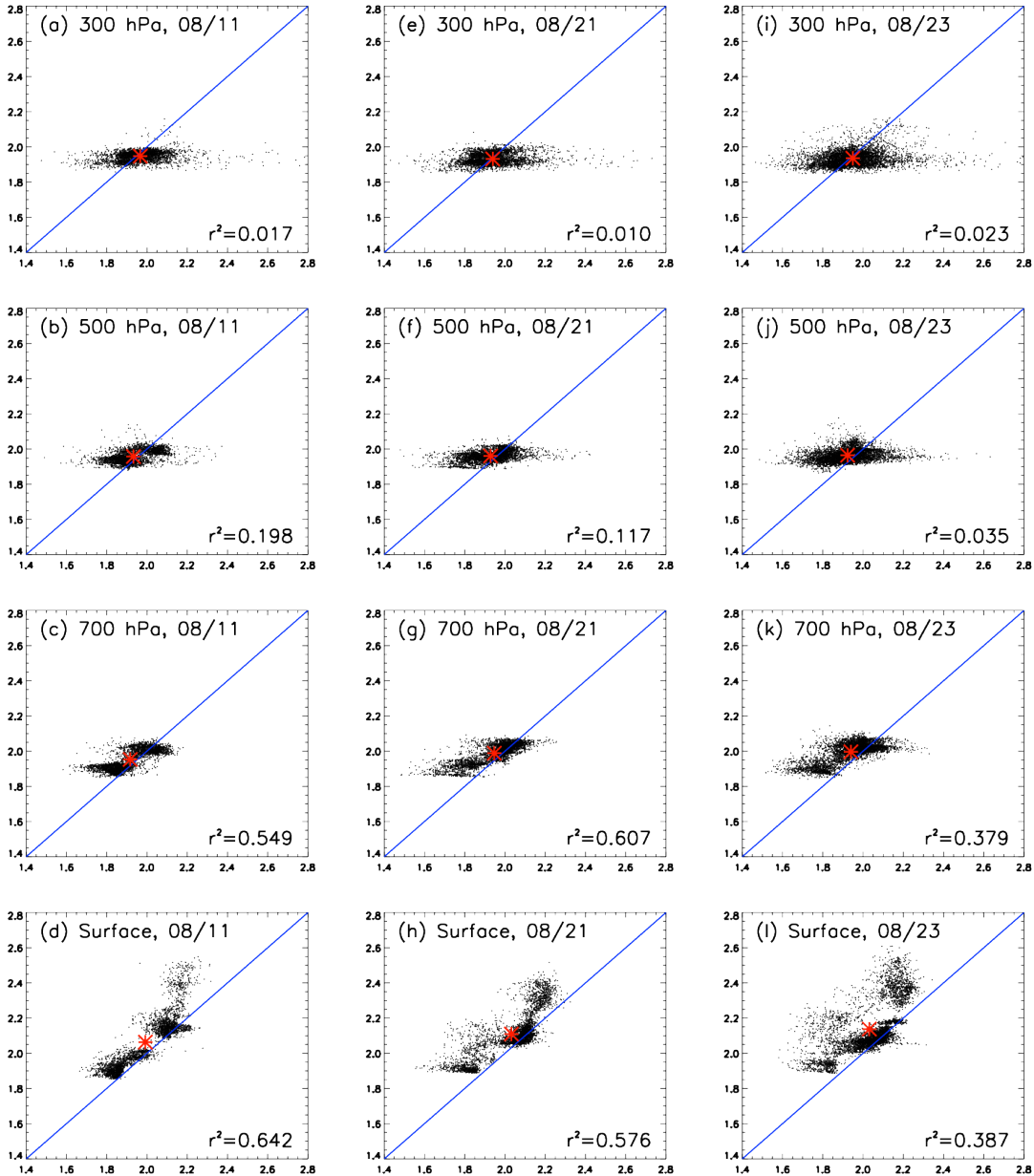


Figure 3.13: WRF and MOPITT CO comparisons — Comparison of WRF-Chem CO \log_{10} VMR (y) against MOPITT \log_{10} retrievals (x) for the indicated dates and pressure levels. Pre-logarithm units are ppbv. Red asterisks are the centers of mass calculated using the geometric means of the two parameters. Diagonal blue lines indicate the identity line. Only data between 12–18 UTC are used.

Figure 3.13 shows the WRF-Chem CO outputs (y), after applying the MOPITT equivalent of Equation 3.12, plotted against MOPITT retrievals (x) at 4 different pressure levels and 3 dates. To minimize diurnal biases, only morning (12–18 UTC) data are used. The total number of columns that lie within the model domain during the given timeframe are 3168, 3693, and 4983 for the 3 days. It is clear that WRF-Chem is performing very poorly in the upper troposphere relative to MOPITT. There is practically no correlation above 700 hPa. The distributions are, nonetheless, consistent with prior validations against TES, wherein WRF-Chem CO has been found to be more well-mixed (vertically) than observed. With this comparison, WRF-Chem is shown to have too much mixing horizontally as well. Considering the means, contrary to previous validations against TES, WRF-Chem is shown to slightly under-estimate CO at 300 hPa, albeit only by -4.4% , -1.7% , and -3.2% for the three days validated. At lower levels, the positive bias in WRF-Chem increases, but so are the correlations with MOPITT. On the surface, the mean biases are $+17.7\%$, $+19.6\%$, and $+27.8\%$.

In conclusion, WRF-Chem CO is almost uniformly biased high compared to satellite retrievals except in the presence of wild fire emission plumes. Comparisons against TES and MOPITT show that CO is predicted to be more well-mixed horizontally and vertically than observations. Constrained by anthropogenic emission sources and coastal boundaries, PBL CO VMRs enjoy high correlations between model and remote sensing data. However, this correlation rapidly drops off for higher altitudes

3.2.4 Formaldehyde

Unlike CO, formaldehyde (HCHO, or CH₂O) has a much shorter residence time of $O(\text{hours})$ in the atmosphere. Besides chemical production from methane, the primary source for HCHO is isoprene, which is emitted by plants, thus HCHO has been used as a proxy for constraining spatial distributions of biogenic emissions. (e.g. *Palmer et al.*, 2006; *Millet et al.*, 2008; *Marais et al.*, 2012). In addition, HCHO may also be emitted through industrial combustion and construction processes. Additional description of anthropogenic and biogenic VOCs are given in Section 1.1.1.

Formaldehyde can be monitored from space using the Scanning Imaging Absorption Spectrometer for Atmospheric Chartography (SCIAMACHY) instrument, an imaging spectrometer on board of the Environmental Satellite (ENVISAT) with an emphasis of monitoring regions with intense biomass burning or anthropogenic pollution (*Burrows et al.*, 1995; *Bovensmann et al.*, 1999). It measures scattered and reflected sunlight in the thermal IR spectral range, providing sensitivity to trace gases in the troposphere such as HCHO and NO₂. The retrieval for the data used in this study is developed at the Royal Netherlands Meteorological Institute (KNMI) and provided by the Tropospheric Emission Monitoring Internet Service (TEMIS) project (<http://www.temis.nl>). Using near-UV radiance measurements and global CTM outputs to provide a priori, HCHO tropospheric vertical column densities (VCDs) are retrieved and constrained using a Differential Optical Absorption Spectroscopy (DOAS) technique (*De Smedt et al.*, 2008). SCIAMACHY HCHO products have also been used for determining long time trends (*De Smedt et al.*, 2010) as well as assimilated to constrain model isoprene (*Dufour et al.*, 2009).

Using the Ozone Monitoring Instrument (OMI; *Levelt et al.*, May 2006), *Millet et al.* (2008) found that most of the high HCHO VCDs are located at approximately east of 96°W and south of 40°N for July–August 2006. Therefore, we focus on SCIAMACHY scans overpassing this region.

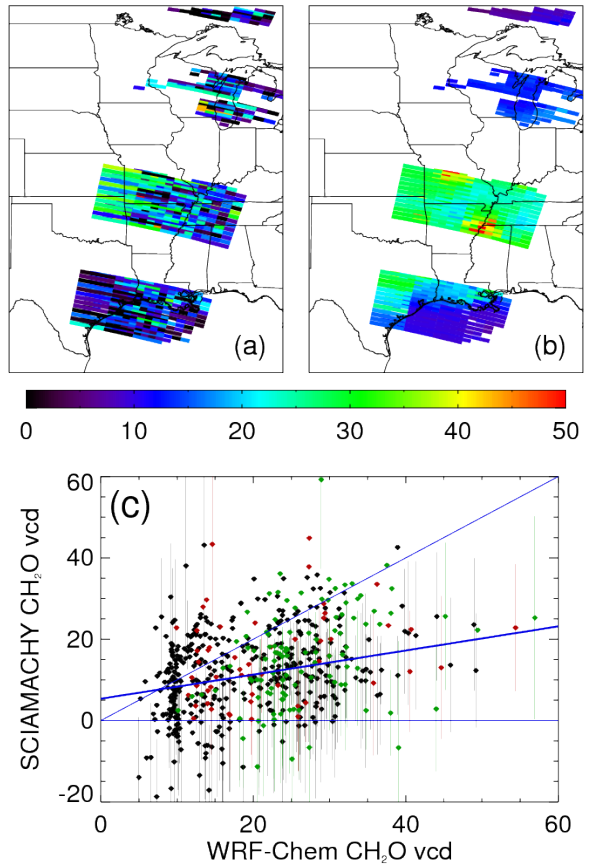


Figure 3.14: SCIAMACHY and WRF-Chem formaldehyde on 8/18 — (a) SCIAMACHY and (b) WRF-Chem HCHO tropospheric VCDs in 10^{15} molecules cm^{-2} for August 18. (c) Both VCDs plotted against each other. Red data points represent anthropogenic sources on the surface. Green data points represent biogenic sources. Blue lines are $y = x$, best-fit, and $y = 0$.

In particular, we use two overpasses on August 18 (track ID 23355) and August 24 (23441) at approximately 16 UTC as examples due to timing and location coincidence of features of interest to this study. The averaging kernels show a mean peak sensitivity between 200–300 hPa with moderate sensitivity close to the surface ($\sim 50\%$ at 700 hPa). To calculate the simulated retrieval error in the VCD, the following equation is used (after *Boersma et al.*, 2004; *De Smedt et al.*, 2008):

$$\sigma_{N_v}^2 = \frac{1}{M^2} \frac{\sigma_{N_s,r}^2}{n} + \frac{1}{M^2} \sigma_{N_s,s}^2 + \left(\frac{\Delta N_s}{M^2} \right)^2 \sigma_M^2 + \sigma_{CTM}^2 \quad (3.13)$$

where $\sigma_{N_s,r}$ and $\sigma_{N_s,s}$ are the random and systematic slant column errors, M is the air mass factor, N_v and N_s are the VCD and slant column density (SCD), n is the number of satellite pixels used, and σ_{CTM} is the error in the reference background from using a CTM during retrieval.

Figure 3.14 shows the pixel-by-pixel comparison of the SCIAMACHY HCHO tropospheric VCDs and the WRF-Chem HCHO VCDs weighting using the SCIAMACHY averaging kernels. All model data points captured by each pixel's bounding polygon are selected and the SCIAMACHY averaging kernel is applied to the geometric mean. In an attempt to classify whether biases are originated from biogenic or anthropogenic sources, data points are highlighted as green if the corresponding model grid-box has a MEGAN isoprene emission factor $> 75 \text{ mol}/\text{km}^2/\text{h}$, i.e. substantial biogenic emission. Those highlighted as red correspond to columns with surface anthropogenic HCHO emission at the 95-percentile from the weekday EPA NEI-08 (see Sect. 1.1.1 and Sect. 3.1.2 for more details). Due to MEGAN's vegetation mapping, biogenic and anthropogenic sources are not mutually exclusive. In cases where both criteria are satisfied, the data point is colored green because of the higher molar emission rate. It should be noted that such categorization of data points is not absolute. Due to transport, non-anthropogenic grids can also see heavy anthropogenic influences. On the other hand, due to the high altitude of SCIAMACHY's maximal sensitivity, pixels expecting high sources of surface emission may not display high VCD when the model is not simulating sufficient lofting.

Similar to the results from the CO validation in Section 3.2.3, WRF-Chem also over-predicts HCHO. However, due to σ_{N_v} being large for most data points, 71% (391/550) of the pixels¹⁰ shown in Figure 3.14 satisfied $|N_{v,WRF} - N_{v,SCIA}| < \sigma_{N_v}$. The minimized- χ^2 fit to the data set gives a slope of 0.297, which loosely implies WRF-Chem predicting three times more HCHO in the atmosphere than observed by SCIAMACHY. Despite the over-estimation, this snapshot sample shows a background value of 10^{16} molecules cm $^{-2}$ and a mean of 2.06×10^{16} molecules cm $^{-2}$, which are consistent with OMI and GEOS-Chem (Millet *et al.*, 2008).

More specific features can also be extracted. For instance, a HCHO local VCD high corresponding to Memphis, Tennessee can be found in the model output but not in the SCIAMACHY retrieval. On the contrary, two single-pixel maxima in the SCIAMACHY retrievals associated with Little Rock, Arkansas and Springfield, Missouri cannot be identified in the model output. This is primarily due to lowering the resolution of EPA NEI-08 data as an input for emission, which subsequently dilutes relatively small urban sources while leaving metropolitan-sized sources intact. However, considering the relative impact of the larger biogenic sources versus small urban sources of formaldehyde, such bias is not expected to have any noticeable influence in the long-term simulated chemistry.

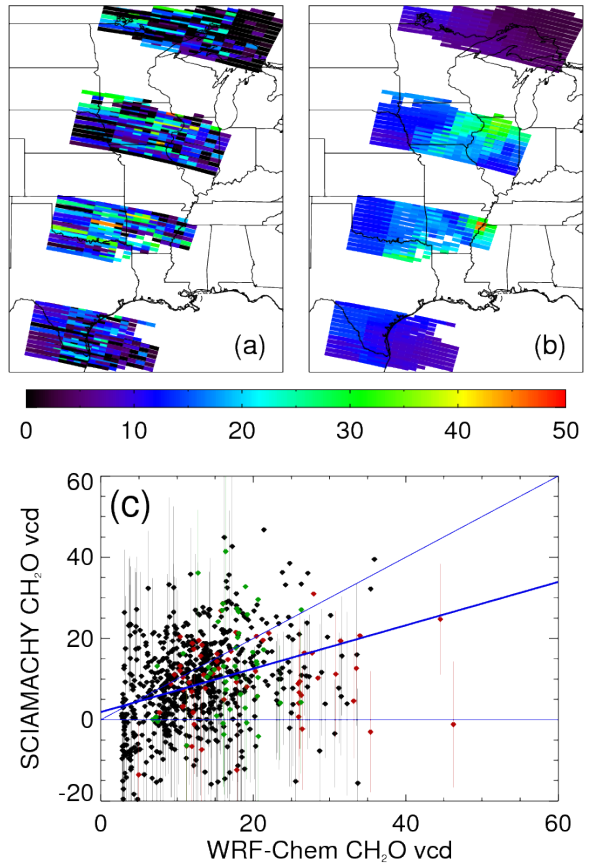


Figure 3.15: SCIAMACHY and WRF-Chem formaldehyde on 8/24 — Same as Figure 3.15 except for August 24.

¹⁰ Error bars for these data points are removed from Fig. 3.14 to avoid overcrowding the figure.

On August 24 (Fig. 3.15), two stationary fronts lingered between the two southern footprints and between the two northern footprints. They generated some convective systems, which caused the missing pixels, but otherwise did not affect the remaining views. Of the 767 pixels available on this day, 612 (79.8%) are within $\pm 1\sigma_{N_v}$ of the identity line. The minimized- χ^2 fit gives a slope of 0.53, which loosely means that WRF-Chem is over-predicting by a factor of 2, compared to the factor of 3 on August 18. Among the large patch of low VCD pixels to the north, the background value is roughly $3 \times 10^{15} \text{ molecules cm}^{-2}$. This is low compared to the *Millet et al.* (2008) seasonal average, but still reasonable compared to SCIAMACHY's retrieval. Otherwise, the rest of the data points are well within the seasonal averages in this area. Similar to August 18, Memphis can again be identified as a spatially isolated formaldehyde source that appears as an outlier in the WRF-Chem distribution but not the SCIAMACHY distribution.

3.2.5 Nitrogen Oxides

Considering that CG flash rate is over-predicted by a factor of 10 (see Sect. 3.2.1), it is expected that NO_x is also substantially over-predicted for the southeastern United States. Indeed, when examining within the anticyclone region, the NO_x VMR is increased by an order of magnitude within the first few days of the simulation (Fig. 3.16). While the initial condition from MOZART provides an average of 300 pptv of NO_x at 300 hPa within the anticyclone, it is increased to 2 ppbv by July 5. Consistent with the hypothesized attribution to tropospheric L NO_x emission, the increase in NO_x is only observed within the troposphere below $\sim 100 \text{ hPa}$ but peaks near 200 hPa where the maximum convective detrainment level typically occurs for larger systems.

To evaluate the model's output, we compare tropospheric NO_2 VCDs against SCIAMACHY's retrieval from KNMI TEMIS. Similar to the formaldehyde retrieval, the algorithm employs the Differential Optical Absorption Spectroscopy (DOAS) method and a data-assimilation technique, which utilizes a chemistry-transport model (CTM) with ECMWF operational analyses meteorology to estimate the stratospheric portion of the retrieved column (*Boersma et al.*, 2004). Validation of the TEMIS NO_2 product has been performed by *Lambert et al.* (2004) against NDSC data, showing

bias up to 3.5×10^{15} molec cm $^{-2}$. The differences between retrievals have been attributed mostly to the tropospheric air mass factor (AMF_{trop}) used (*van der A et al.*, 2010), which has a sensitivity to cloud fractions of up to 20% (*Boersma et al.*, 2004).

Considering the transient nature of storms and the model's skill in predicting the exact locations and magnitudes of individual convective cores over the entire 2-month simulation at a relatively low resolution, this comparison will be performed over a large number of orbits as opposed to individual retrieval as done in the previous section for formaldehyde (Sect. 3.2.4). However, since the pixel size is relatively small and almost always contained within a model grid, each pixel is only associated with a single model column determined by directly mapping to the WRF Lambert conformal grid. Corresponding WRF-Chem output is determined by rounding the time of measurement to the nearest 3-hour. Due to EN-

VISAT's orbit, all measurements are taken between 15–21 UTC. Matched WRF-Chem NO₂ partial columns are then accumulated using the tropospheric VCD averaging kernel defined as $A_{trop} = A \cdot AMF/AMF_{trop}$, where A is the total column VCD averaging kernel, for levels below the provided tropopause index computed using the WMO tropopause definition. These VCDs, together with the associated retrieval biases and SCIAMACHY VCDs, are then accumulated back onto the WRF model grid. Over 61 days, 5.2×10^5 pixels were selected, accounting for $\sim 1\%$ of all pixels globally over the same period. Individual model grid receives anywhere between 0 to 15 pixels, which is less than 20 (≈ 61 days/3 days per global survey) due to rejected measurements.

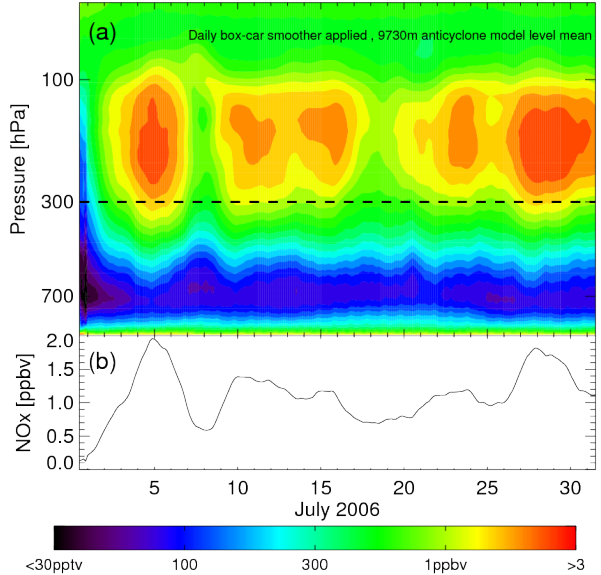


Figure 3.16: **WRF-Chem NO_x VMR** — (a) Average NO_x VMR within the anticyclone region during July 2006 showing sharp increase towards a higher steady state within the first few days of the simulation. (b) VMR time-series at 300 hPa showing a sample of the temporal variability within the anticyclone.

Using this procedure, the frequency distributions of WRF-Chem and SCIAMACHY KNMI NO₂ tropospheric VCDs are calculated (Fig. 3.17a). While the WRF-Chem distribution is lognormal with a background close to 0.1×10^{15} molec. cm⁻², the SCIAMACHY distribution is closer to a normal distribution skewing towards the left with a negative tail. Negative values in tropospheric column is permitted because of the retrieval process, which involves estimating and subtracting the NO₂ stratospheric column. Despite the differences in the distributions, the modes for both distributions are close to 0.5×10^{15} molec. cm⁻², consisting mostly of data points from the Pacific marine columns, Idaho/Montana, and Canada. These regions have low contributions from NO_x of anthropogenic or lightning sources, thus making them less susceptible to biases in emission inventory and lightning parameterization. On the contrary, but as expected, the WRF-Chem substantially over-estimates the $> 2 \times 10^{15}$ molec. cm⁻² range, which corresponds to levels typically observed only at locations with persistent anthropogenic sources. Because of the high bias in lightning emission, NO₂ VCDs over the southeastern United States and Mexico are severely over-estimated (Fig. 3.17c&d).

Using the passive decaying LNO_x tracer, described in Section 3.1.3, each tropospheric VCD data point can be classified as below or above half of the median LNO_x tracer tropospheric VCD ($\approx 4.39 \times 10^{15}$ molec. cm⁻²) computed using the SCIAMACHY averaging kernel (Fig. 3.17b). The results from attempting to perform linear regressions on the data points are summarized in Table 3.3. The upper partition ($VCD > 4.39$), which corresponds to a high level of LNO_x tracer in the model, correlates poorly with SCIAMACHY retrievals with a reduced- $\chi^2 = 52$. The mean ratio of WRF-Chem VCD to SCIAMACHY VCD is 4.9, i.e. NO₂ level is 5 times higher than observed when the region is heavily influenced by LNO_x emission. On the contrary, the lower partition ($VCD < 4.39$) shows good correlation between the model and observation with $\chi^2_{reduced} = 0.911$. For this category, WRF-Chem over-predicted NO₂ by only 17% when lightning is minimally involved.

Finally, the above model-observation comparison should be interpreted with caution as there are numerous factors that prevent literal interpretations. One factor is the frequency distribution of VCDs. While the model shows a lognormal-like distribution, SCIAMACHY's retrieval intro-

duces a negative tail. Since negative values in tropospheric VCD is meaningful and represents a crucial property of the retrieval process, they cannot be filtered out and must be included in the overall statistics. However, the exact interpretation of these non-physical negative VCDs remain ambiguous.

The ozone level is sensitive to the balance between VOC and NO_x (Sect. 1.1.2). In Section 1.1.2, it is shown that (CG) lightning is over-predicted by a factor of 10 under the assumption of a constant CG fraction of 1/4. Together with the validation results from the previous sections (Sect. 3.2.3 & 3.2.4), the model is expected to simulate an both excess VOCs and excess NO_x relative to observation, thereby explaining the over-estimation of ozone shown in Section 3.2.2. By comparing model CO (Sect. 3.2.3), formaldehyde (Sect. 3.2.4), and NO₂ (Sect. 3.2.5) against remote sensing profiles, it is indeed shown that both VOCs and NO_x are definitively over-estimated, though due to intricacy of the validation methods, the numerical results from the comparisons may not be construed with absolute certainty. Nonetheless, by accounting for these biases, the analyses done in Section 3.3 will proceed with caution and will frequently reference individual result from this section when appropriate.

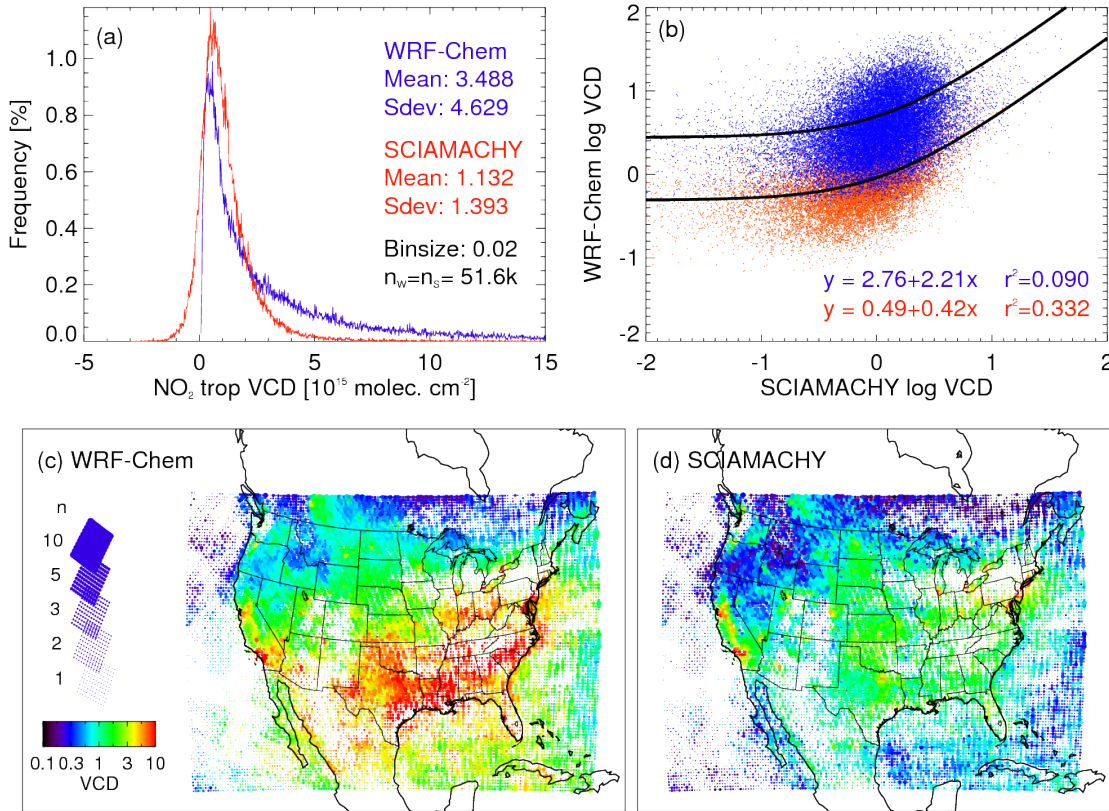


Figure 3.17: **WRF-Chem and SCIAMACHY NO_2 VCDs** — (a) Frequency distributions of WRF-Chem and SCIAMACHY NO_2 tropospheric VCDs in $10^{15} \text{ molec. cm}^{-2}$ during July and August 2006. (b) A log-log plot of the two tropospheric VCDs partitioned into halves by median passive lightning tracer tropospheric VCDs and their corresponding linear minimized- χ^2 fits and correlation coefficient r^2 . (c) Spatial distribution of mean WRF-Chem tropospheric VCDs in $10^{15} \text{ molec. cm}^{-2}$. With pixel density indicating the number of samples used to compute the mean (up to $n = 15$ but saturates at $n = 10$) at each model grid point. (d) Same as c, but for SCIAMACHY.

3.3 Discussion

3.3.1 Tracer relations

The relationship between ozone and carbon monoxide (CO) has been used to study tropospheric-stratospheric transition in chemical regimes (e.g. *Pan et al.*, 2007; *Hegglin et al.*, 2009, and references therein). Similarly, such analysis may be applied to tropospheric data alone to identify contributions from various pathways (e.g. *Zhang et al.*, 2006; *Voulgarakis et al.*, 2011; *Cristofanelli et al.*, 2013). Ignoring NO_x, ozone is expected to be strongly positively correlated with CO (*Chin et al.*, 1994, , see also Ch. 1). However, since the dominating source for CO is surface emission, boundary layer dynamics strongly limit CO's concentration in the upper troposphere. On the other hand, near the tropopause, contribution of stratospheric ozone and upper tropospheric production cause ozone to increase rapidly with height. Together, O₃–CO anti-correlation over a sufficiently expansive column can expect to observe an "L"-shaped joint distribution.

Here we examine the joint-distribution of the August average model ozone and CO from the surface up to 100 hPa (Fig. 3.18). Data points are first separated by within and outside of the anticyclone, defined by the boundary \bar{Z}_{300} as previously defined in Section 3.2.2. Then, each panel is further classified by pressure levels split at 300 and 700 hPa to represent the lower, middle, and upper troposphere. To account for model biases, ozone VMRs between 100–300 hPa have been adjusted by the differences in mean and variance against TES computed in Section 3.2.2.

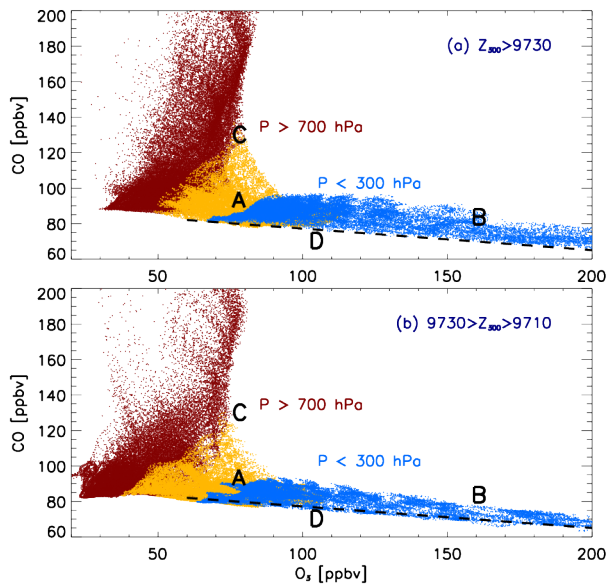


Figure 3.18: CO-O₃ model correlation — (a) Anticyclone ($\bar{Z}_{300} > 9730$ m) CO-O₃(adjusted) joint-distribution separately colored by pressure levels: red below 700 hPa, blue above 300 hPa, and yellow in between. (b) Same as a but outside the anticyclone between 9710 m and 9730 m. Data points south of 25°N have been removed to reduce impact of the southern boundary.

No adjustment is performed at the other pressure levels due to insignificant bias compared to observations. The shape and features of the joint-distribution remain consistent before and after the adjustment. The labeled features annotated in the figure are discussed below.

Feature A indicates a type of air mass exist only outside the anticyclone. By identifying the locations and timing of these data points, this feature is identified to be corresponding to subtropical Atlantic influx from the southern boundary. Typically, it has higher CO but the ozone VMRs at 300 hPa from lower latitudes are lower in general. These air masses intermittently contribute to the anticyclone, similar to the air masses mixed across the jet stream from the north (see Sect. 3.2.2 & 3.2.3). Feature B indicates the upper tropospheric branch of the O₃-CO distribution. It is evident from the labels, which are placed at the same locations in both panels, that CO is more effective in raising the ozone level within the upper troposphere above the baseline, indicated by the dashed line (feature D), which is manually fitted and replicated for the sole purpose of acting as a visual aid for inter-comparison between panels. Using the dashed line as reference, the baselines from both panels appear practically identical. Thus, it can be argued that the background O₃-CO correlations are consistent both inside and outside the anticyclone. Finally, feature C denotes the mid-to-lower tropospheric branch, which includes the boundary layer. Similar to B, feature C is chemically different across the anticyclone. Since the upper air anticyclonic circulation is not a huge factor at low altitudes, a plausible explanation is the relatively abundant sources of anthropogenic and biogenic emissions of both VOCs and NO_x, which subsequently enhance in-situ ozone production within this layer and transported upwards. Finally, the low-CO, low-O₃ value at the interface of lower and middle tropospheres is about 10 ppbv higher within the anticyclone compared to the ~38 ppbv value outside of the region despite negligible differences in their corresponding CO level, potentially indicating influence from NO_x.

The analysis above shows that the conditions within the anticyclone has higher ozone values throughout the entire troposphere at a wide range of VMRs for CO (features B and C). Since emission dominates transport in the lower troposphere, the appropriate hypothesis for the enhancement at C is the elevated level of NO_x from either co-located emissions or subsidence of LNO_x within the

region. However, more information is required to properly diagnose feature B, which can be either an indication of enhanced O₃ chemical production at the 80 ppbv CO or enhanced CO at levels with O₃ through convective detrainments.

Figure 3.19 shows four of the tracers released from the lateral boundaries, the boundary layer, the stratosphere, and lightning sources. All tracers shown decay with a lifetime of 1 day (1-d) to account for loss of chemical properties over time. The impact of the NAM circulation is clearly shown in the spatial distribution of the lateral boundary (BC) tracer (Fig. 3.19a). Within the anticyclone region ($\bar{Z}_{300} > 9730\text{ m}$), the air mass retains no more than an average of 3% of the characteristics from any of the boundaries. Since these tracers are dynamically-driven, i.e. independent of chemistry, it can be confidently asserted that the impact of boundary condition on the principal results is minor.

The lightning NO_x tracer (LT) tracer also shows substantial localized enhancement within the anticyclone (Fig. 3.19g). The observed eastward shift from the 9730 m contour can be explained by the overall higher lightning flash rate in the southeastern United States. Accounting for the one order of magnitude deviation from observed CG flash rate, the maximum accumulated lightning 1-d tracer is 0.5 ppbv. Despite a fixed maximum emission altitude of 6–8 km ($\sim 400\text{ hPa}$) according to *Ott et al.* (2010), the vertical distribution along the 33°N cross-section shows that the tracer has values $> 3\text{ ppbv}$ (0.3 after account for overprediction in flash rate) within a wide range of pressure levels between 120–500 hPa (Fig. 3.19h). Finally, the abundance of lightning decaying tracers in the stratosphere is likely the direct result of using a fixed altitude-dependent emission profile, which includes more than 10% (35 moles flash⁻¹) above 12 km for subtropical latitudes.¹¹

On the other hand, the spatial distribution of the boundary layer (BL) tracer shows little correlation with the shape or positioning of the anticyclone. Instead, the features of the tracer at 300 hPa are dominated by orographic influence of the Rocky Mountains near 115°W (Fig. 3.19c). Similarly, the stratospheric (ST) tracer shows very minimal impact from the NAM circulation

¹¹ Due to this, it may be a good idea to scale the *Ott et al.* (2010) distribution by tropopause height.

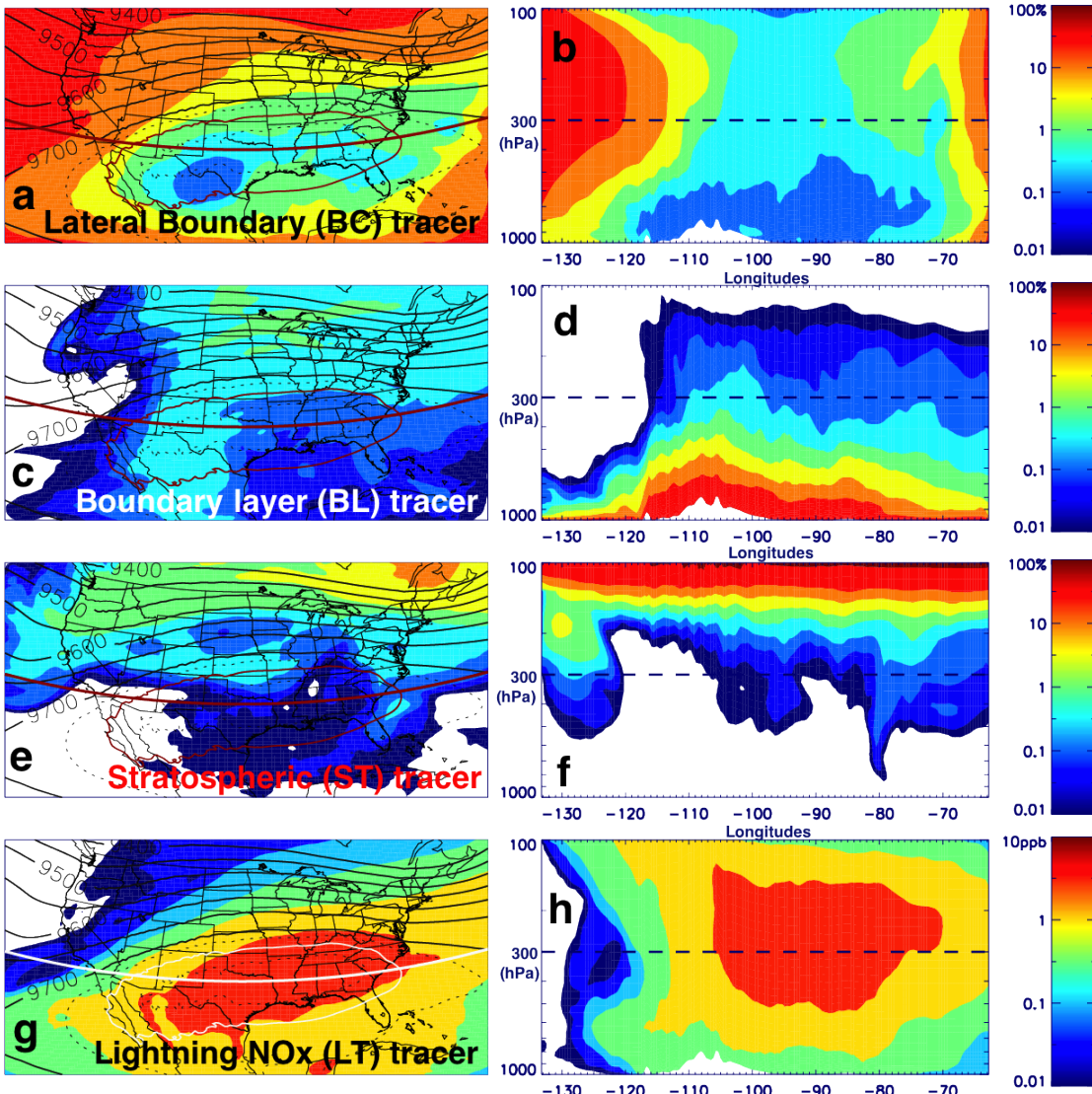


Figure 3.19: **Passive tracers** — First row (a,b) shows the August average of lateral boundary decaying tracer at 300 hPa on the left and along 33°N on the right. Values are given in percentage. Second row (c,d) shows the surface layer decaying tracer. Third row (e,f) shows the stratospheric decaying tracer. Last row (g,h) shows the lightning decaying tracer given in ppbv.

except for the influx of air with high ozone associated with mesoscale eddy eddies in the region of strong wind shear near the jet in the outflow region along the eastern seaboard.

The tracer equivalent ages, calculated according to Equation 3.11, are mapped in Figure 3.20. Similar to the decaying tracer distributions, BC and LT tracers are the only ones showing some correlations with the anticyclone boundary. The range of age for BC tracer within the anticyclone is 2.6–6.8 days while the range outside the anticyclone between 9710 m and 9730 m is 1.5–4.8 days. LT tracer age ranges from 10.9–21.8 hrs within the anticyclone and 13.1–22.5 hrs just outside. The primary contribution to the LT distribution is that the anticyclone encompasses areas with high lightning flash frequencies, and thus younger tracers are expected only on the eastern $\sim 2/3$ of the anticyclone as well as towards the outflow region along the East Coast. On the west end of the cross-section (Fig. 3.20h), the upper tropospheric presence of LT tracer (Fig. 3.19h) is shown to be of different ages from the high LT tracer core within the anticyclone.

Individually, BL and ST are dominated by orographic or large scale features. By relating the two tracers, differences emerge. Figure 3.21 shows the joint distribution between the two decaying tracers. At feature A, or absence thereof within the anticyclone, low ST-low BL data points exist only in the mid-troposphere (300–700 hPa) outside the anticyclone. Similarly, feature C (moderate ST/BL) occurs outside the anticyclone only. These two features point to higher heterogeneity of sources of air mass outside the anticyclone than within the anticyclone between 700 and slightly above 300 hPa. Such result can be attributed to the geographic diversity outside the anticyclone, primar-

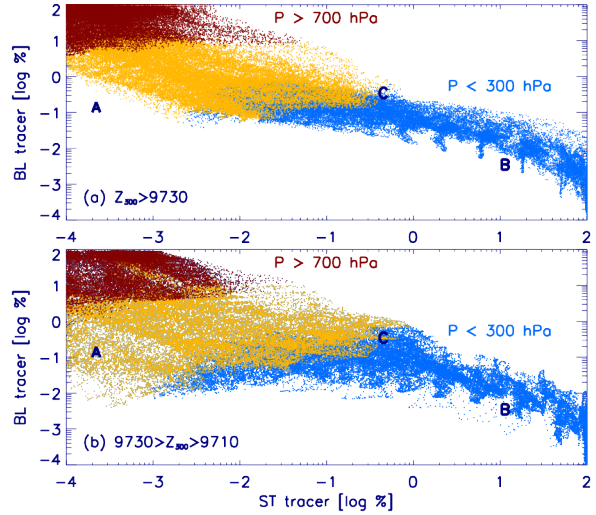


Figure 3.21: **BL-ST tracer correlation** — Same as Fig. 3.18 but for BL and ST decaying tracers in $\log_{10} \%$.

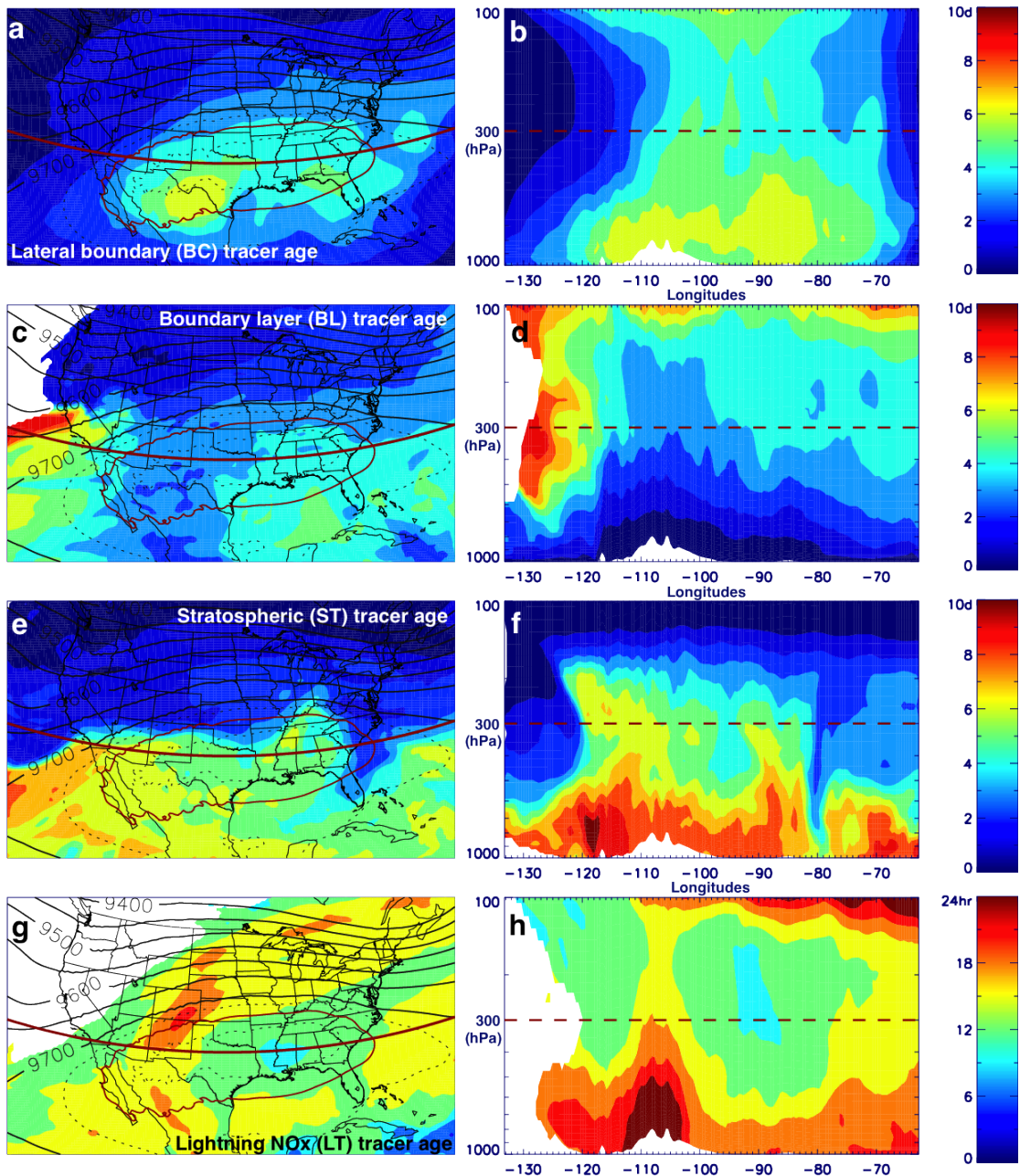


Figure 3.20: **Passive tracer age** — Same as Figure 3.19 except for tracer equivalent age. Low variance data points ($< 10^{-4}$) have been masked out.

ily the presence of ocean surfaces. Finally, both regions show very little differences close to the tropopause, where $ST \sim 1$.

The result in this section partially contradicts that of *Li et al.* (2005) and *Cooper et al.* (2007). On one hand, LNO_x is indeed shown to be accumulating within the anticyclone and roughly follows the circulation pattern. However, we do not see signs that the anticyclone is enabling higher ozone production through recirculation and entrapment of detrained BL air rich in ozone chemical precursors. The result here shows that the vertical colocation of boundary layer features as well as meteorological factors (e.g. high lightning intensity) are the key factors driving the ozone enhancement. On the other hand, the lack of model lateral boundary influence, as indicative of the BC tracer low within the anticyclone, points to low externality, i.e. small influence from outside the anticyclone, as another important factor as opposed to internal conditioning, e.g. accumulation of boundary layer air as suggested by previous studies. The only¹² factor acting from within the anticyclone is the influence from lightning emissions, which shows correlation with the transport pattern of the anticyclone.

3.3.2 Tendency diagnostics

The changes in the mixing ratio of a chemical species at a specific time and location, or tendency, can be expressed as the sum of the following components: chemistry, convection, vertical mixing, horizontal advection, vertical advection, emission, and other loss rates (Eq. 3.8). In the upper troposphere, except for NO, both emissions and other uncharacterized loss rates should be zero, and thus the total tendency can be expressed solely by the first five processes. Consequently, inference of chemical and dynamical structures of the ozone budget is possible using these diagnostics. Tendency diagnostics of these 5 components are available for O₃, CO, NO, NO₂, HO, HO₂, TOL, and HC5 in WRF-Chem.¹³

¹² Eventhough this study does not include aircraft emission, aircraft tracers, if present, are expected to act similar to LNO_x tracers (see *Hudman et al.*, 2007).

¹³ TOL=Toluene; HC5=Bulk species for alkane with moderate HO rate constants. These replace isoprene and HNO₃ in the default implementation.

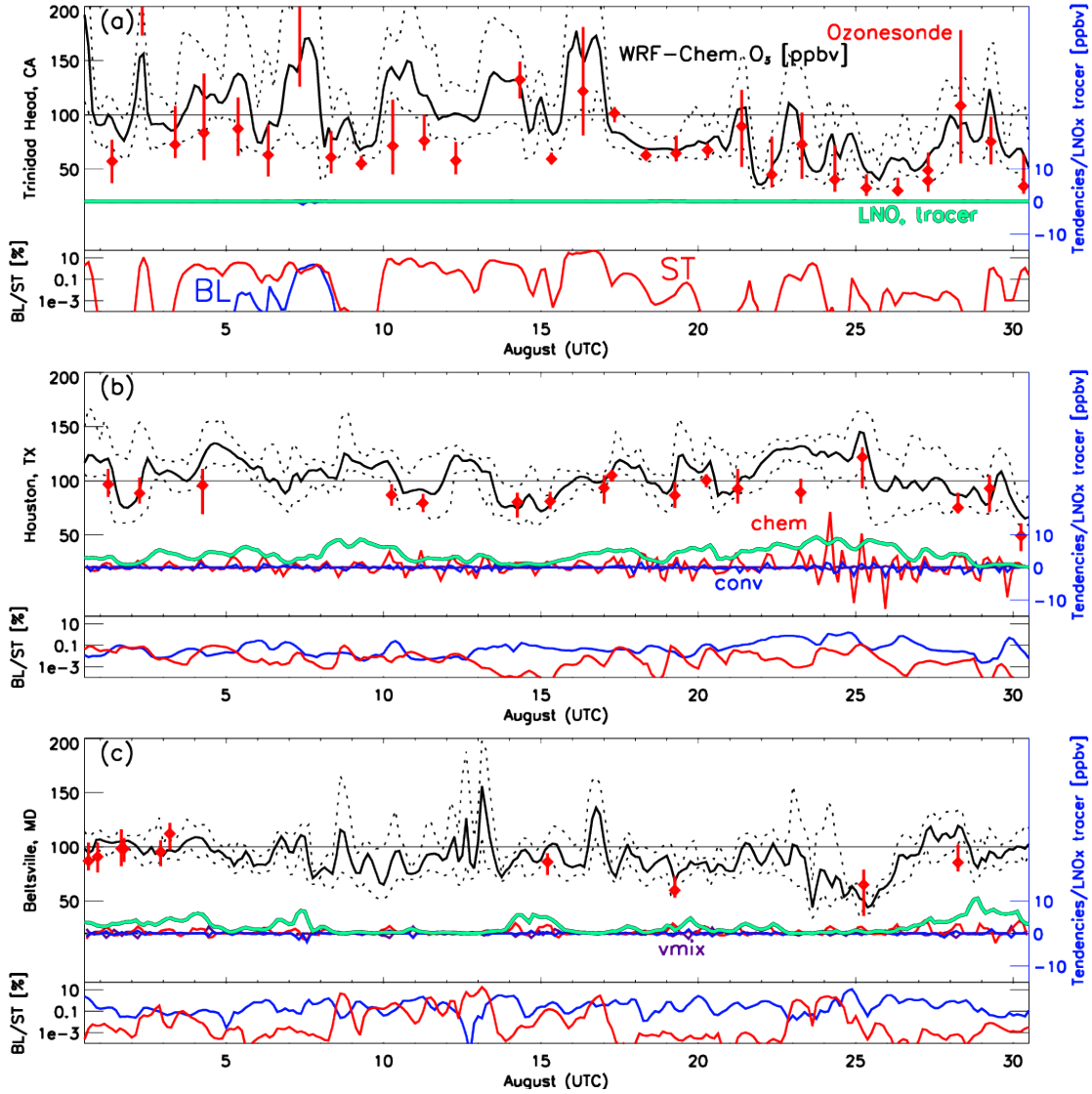


Figure 3.23: **Time series for upper tropospheric tendency diagnostics** — Time series at (a) Trinidad Head, (b) Houston, and (c) Beltsville showing the min-mean-max ozone time series (black) between 270–330 hPa overlaid with IONS-06 ozonesonde measurements represented as red vertical lines for the range and solid \diamond for the mean value. Lightning NO_x decaying tracer (cyan) and ozone chemical (red), convective (blue), and vertical mixing (purple) tendency components are given according to the blue axis labels on the right in units of ppbv/3 hr. Boundary layer (BL, blue) and stratospheric (ST, red) are also given in %.

The primary sources for local temporal variabilities are horizontal advection and vertical advection. Figure 3.3.2 shows the advective tendencies for ozone compared to the total ozone tendency sampled near Houston between 200–600 hPa. Both the horizontal and vertical components are often on the same magnitude as the total tendency. However, the combined advective tendency is frequently much smaller because the two components are often anti-correlated with opposite signs. The residual tendency, i.e. the total ozone tendency without the two advective components, can be accounted for by chemical, convective, and vertical mixing tendencies. It is useful to note that the residual is not guaranteed to be smaller than the total tendency due to the ability for advective tendencies to “cancel” out the effect of the remaining three components, as seen after August 23.

To characterize the residual tendency of the continental inflow, the anticyclone, and the continental outflow, three locations are selected to be examined further: Trinidad Head, California ($40.80^{\circ}\text{N}, 124.15^{\circ}\text{W}$), Houston, Texas ($29.72^{\circ}\text{N}, 95.30^{\circ}\text{W}$), and Beltsville, Maryland ($39.04^{\circ}\text{N}, 76.52^{\circ}\text{W}$). Figure 3.23 shows the time series of the ozone VMRs at these locations as well as the associated chemical, convective, and mixing tendencies. Values shown are the mean values for all data points between 270–330 hPa, with min/max also indicated for ozone VMR. To account for the model bias, IONS-06 ozonesonde measurements, described in Section 3.2.2, are also included. Boundary layer (BL), stratospheric (ST) and lightning (LNO_x) decaying tracers, described in Section 3.3.1, are included to provide context of the sources for the dynamical and chemical variabilities.

Trinidad Head periodically receives stratospheric ozone from the northern latitudes, which is responsible for the sharp spatiotemporal gradients of high ozone simulated for particular days (e.g.

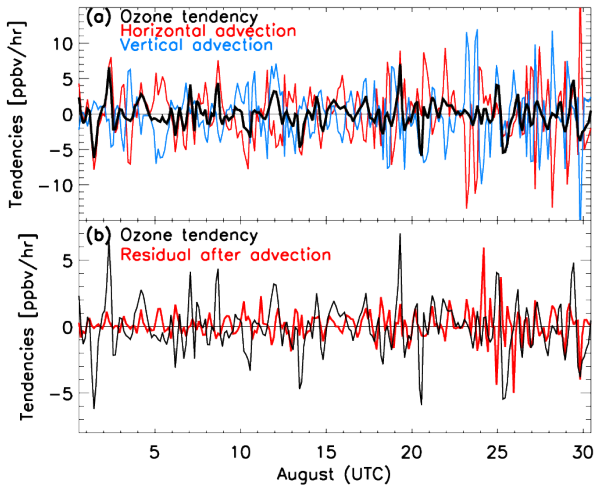


Figure 3.22: Ozone advective tendency — Ozone tendencies and (a) advective tendencies and (b) residual tendencies after removing advective tendencies between 200–600 hPa.

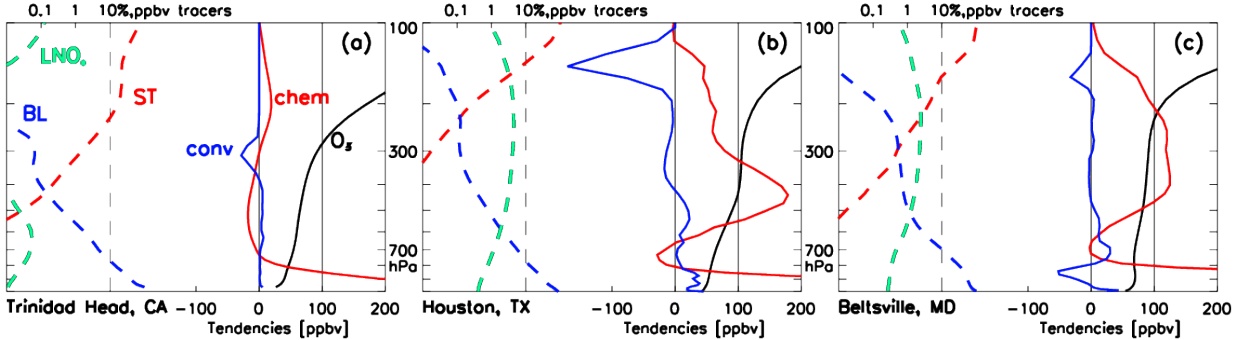


Figure 3.24: **Vertical profiles of decaying tracers and tendency diagnostics** — August vertical profiles at (a) Trinidad Head, (b) Houston, and (c) Beltsville. Dashed lines are the mean 1-d decaying tracers for BL (blue, %), ST (red, %), and LNO_x (cyan, ppbv) according to the values of the top axis. Solid lines are the accumulated chemical tendency diagnostic (red), convective tendency diagnostic (blue), and mean ozone profiles in ppbv according to the values of the bottom axis. Closest 11×11 grid points to the IONS-06 site are selected to compute these profiles.

August 2 and August 7). The largest 3-hourly chemical tendency for Trinidad Head is 0.37 ppbv per 3 hours. Similar to chemical tendency, convective and vertical mixing tendencies are also negligible, and thus advective tendencies dominate the ozone variability in this region with a mean 3-hourly absolute advective tendency of 8.28 ppbv per 3 hours. On the other hand, ozone has the highest chemical tendencies at Houston, with minimum/maximum values of $-12.8/17.1$ ppbv per 3 hours. The corresponding minimum/maximum values at Beltsville are $-2.94/3.90$ ppbv per 3 hours. However, due to less frequent negative (or loss) phases, the accumulated chemical tendency at Beltsville is higher than that at Houston, with a value of 110 ppbv compared to 69 ppbv over August.

Both convective and mixing tendency components are small at all three locations, with accumulated values (over August) of -13.4 ppbv convective and 3.6 ppbv mixing at Houston, -5.1 ppbv convective and 3.5 ppbv mixing at Beltsville, and -2.0 ppbv convective and 8.1 ppbv mixing at Trinidad Head over the entire August. The relatively larger value of vertical mixing tendency at Trinidad Head can be attributed to the jet stream, which provides large vertical gradient in ozone VMR. For convection, detrainment of ozone-poor BL air causes ozone to be diluted and thus the convective component is predominately negative.

Figure 3.3.2 shows the vertical profile of the mean decaying tracers and accumulated tendencies within 5 grids (11×11) surrounding the IONS-06 sites from August 1 00 UTC to August 31 00 UTC. The inflow region (Trinidad Head) lacks both BL air and LNO_x in the upper troposphere. Despite comparable ozone level to the other two locations, the accumulated tendency in the upper troposphere remains low with a maximum of 19.4 ± 2.5 ppbv. Because of the lack of in-situ chemical production, the ozone level remains low between stratospheric intrusion episodes, allowing the air to remain relatively “clean” until reaching Minnesota (Fig. 3.6). This influx of low-ozone, chemically-“slow” air mass when there is not a stratospheric event is therefore responsible in generating the oval-shaped ozone enhancement that trace the mean circulation in the seasonal average.

At Houston, at the center of the mean-state anticyclone, both the ozone chemical and convective tendencies are substantially higher than Trinidad Head. At 200 hPa, where Trinidad Head records the peak net upper tropospheric ozone production, Houston records 55.8 ± 18.6 ppbv, about 2.9 times higher. However, this number, as discussed earlier, has been suppressed due to large negative phases of the diurnal cycle, which are caused by large amount of BL air and LNO_x as indicated by the tracers. Ozone-poor air is transported into the upper troposphere through convection, detraining primarily at 145 hPa with a net change of -170 ppbv O₃ during August, in part caused by a nearby outlier with -1170 ppbv¹⁴ during August. However, the chemical maximum above the BL occurs in the mid-troposphere at 437 ± 2 hPa with a net production of 178 ± 51 ppbv of O₃. The position of this peak can be explained by the coincidence of the maximum level for the prescribed LNO_x emission based on Ott *et al.* (2010) and the availability of BL air. As a consequence of production at this level, the mean ozone VMR exceeds 100 ppbv at 437 hPa. In contrast, without LNO_x, ozone loss via chemistry is expected at this level as demonstrated at Trinidad Head.

In the outflow region, as represented by Beltsville, there is a higher net in-situ production of ozone in the upper troposphere despite having lower ozone mixing ratios in the mid-to-upper troposphere compared to Houston. This can be attributed to having less frequent negative phases

¹⁴ Localized high convective tendency is an indication for stationary features such as sea breeze or orographically triggered convections.

that destroy ozone at night. Despite the smaller net convective tendency, the BL tracer is higher than or comparable to the Houston column, indicating that ozone precursors are advected from elsewhere. An in-depth analysis of the ozone budget and variability at this location and New England can be found in *Thompson et al.* (2007a,b), which utilizes IONS-04, the predecessor of IONS-06. They found that tropospheric ozone in northeastern North America was composed of 10–15% BL sources, 10–15% regional sources including lightning, 20–25% stratospheric ozone, and $\sim 50\%$ recently advected or aged air from elsewhere.

3.4 Sensitivity study

There are numerous variables in the base case simulations that could have contributed to the model biases as evaluated in Section 3.2. In particular, the emission and distribution of lightning-generated NO_x (LNO_x) have been shown to be a significant component in determining the atmospheric composition in the free troposphere as represented by CTMs (*Labrador et al.*, 2005; *Cooper et al.*, 2009; *Ott et al.*, 2010). Thus it is useful to perform sensitivity simulations to determine the range of variabilities caused by the uncertainties and biases in the lightning parameterization.

Other than the lightning-generated NO emission, anthropogenic and biogenic emissions are also crucial in determining the atmospheric composition. While having a lesser degree of uncertainty and sensitivity compared to LNO_x, urban developments and policy changes can have substantial impacts on the emission inventory (Sect. 1.1.2). As such, sensitivity studies on anthropogenic and biogenic emissions are valuable in determining the calibration requirements for hypothetical scenarios that correspond to potential changes.

3.4.1 Lightning emission

The comparison to NLDN flash counts shows that the current lightning parameterization is producing an order of magnitude higher overall flash rates (Sect. 3.2.1). Two simulations are performed to account for the effect of overpredicting lightning flash rate, as well as to evaluate the sensitivity of the ozone enhancement to the LNO_x. These two simulations are identical to the

base case simulation in Section 3.2 except with lightning tuning parameter set to $0\times$ and $0.1\times$ to represent a control (no lightning) scenario and tuned-lightning scenario. The resulting spatial distributions of several species at 300 hPa are shown in Figure 3.25.

NO_x is substantially increased above background values (31.6 ± 4.5 pptv) to 135 ± 35 pptv with $0.1\times$ lightning and 1680 ± 540 pptv with $1\times$ lightning. Modeling the contribution of total NO_x mixing ratio by lightning-generated NO_x as follow:

$$\Delta[\text{NO}_x] = [\text{NO}_x] - [\text{NO}_x]_0 = (1-p)[\text{LNO}_x] \quad (3.14)$$

where p is the percentage loss of LNO_x in the atmosphere and $[\text{NO}_x]_0$ is the no-lightning NO_x VMR. For small changes in the atmospheric composition, p should be constant and thus the addition of LNO_x should linearly increase $[\text{NO}_x]$. False extrapolating this to $1\times$ flash rate, the expected $[\text{NO}_x]$ would have been 1070 pptv. However, because of the decrease in HO_x , the primary reagent converting NO_x into reservoir species, in response to LNO_x , $\partial p / \partial [\text{NO}_x] < 0$, and thus giving us the simulated 1680 pptv, higher than the linearly extrapolated value.

Unlike NO_x , HO_x is substantially decreased with increasing LNO_x emission. The initial August mean VMR at 300 hPa without lightning is 6.94 ± 0.38 pptv within the anticyclone. This is above the $\sim 4\text{--}5$ pptv in the Pacific Northwest and inflow regions. It is slightly decreased to 6.27 ± 0.37 pptv with $0.1\times$ lightning, or a 10% decrease from the $0\times$ scenario. At $1\times$ LNO_x emission, HO_x is further decreased to 1.80 ± 0.59 pptv, far below the value to the northwest, representing a 71% drop relative to the $0.1\times$ scenario, which is larger than that would have been obtained if one ($\sim 61\%$) were to extrapolate the initial 10% decrease with an exponential model. The decreasing HO_x with increasing NO_x is the results of its interactions with O_3 , NO_x , and CO after production from the $\text{O}(^1\text{D}) + \text{H}_2\text{O}$, which is presumably proportionally increasing with the increased level of O_3 . However, because the VMRs of all species have been perturbed as the result of LNO_x emission, it is challenging to describe the new mean HO_x with LNO_x relative to the control state with $0\times$ lightning.

Even though $\text{CO} + \text{OH} \rightarrow \text{CO}_2 + \text{HO}_2$ is the only chemical loss pathway for CO specified in RADM2 and that HO_x is substantially decreased by a factor of 3.8 from $0\times$ to $1\times$ lightning, CO

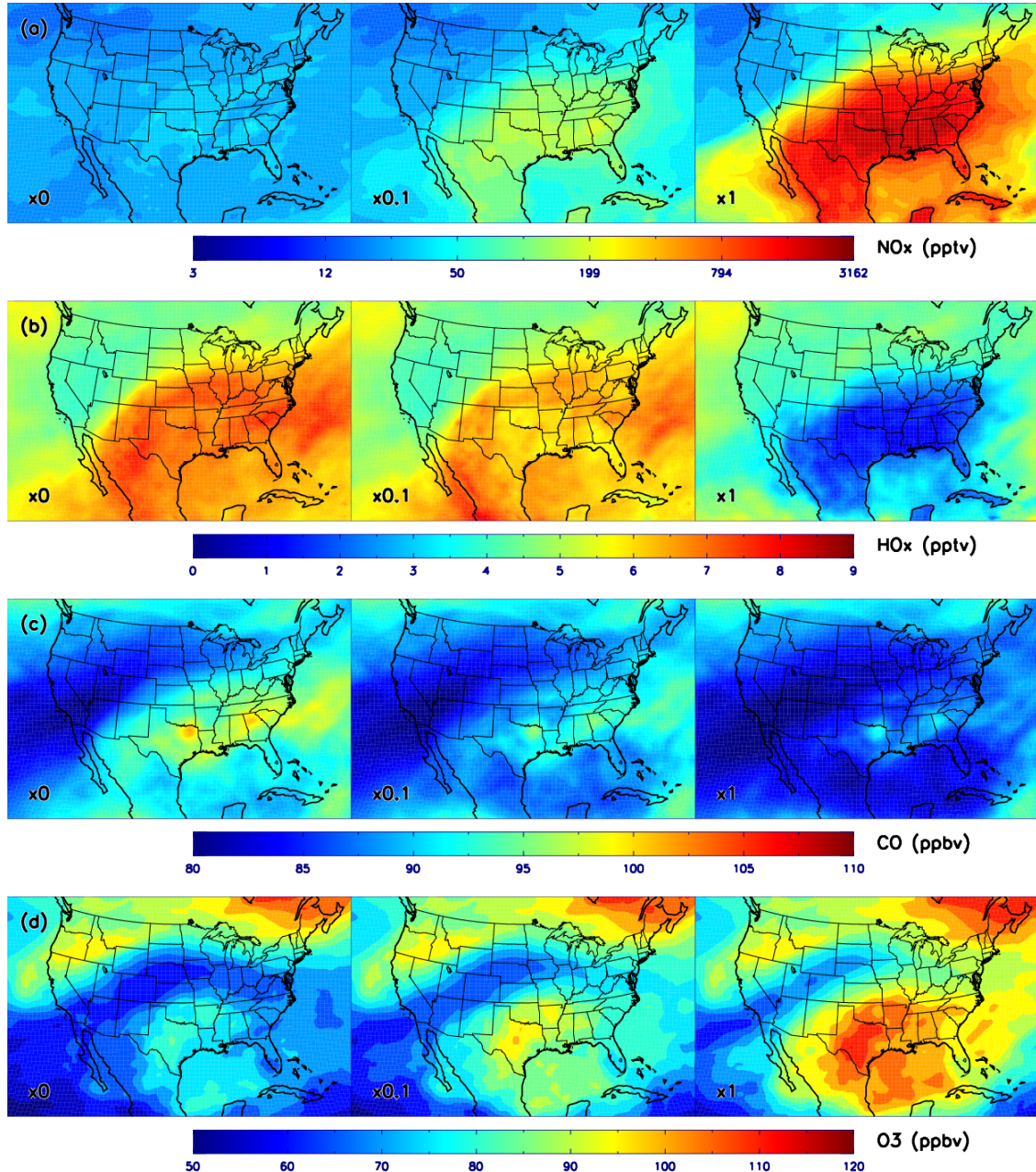


Figure 3.25: **Upper tropospheric sensitivity to lightning** — Model simulated mean (a) NO_x, (b) HO_x, (c) CO, and (d) O₃ for 0× (left column), 0.1× (center column), and 1× (right column) lightning flash rate at 300 hPa for August. Note that NO_x is contoured in the log-scale.

decreases with increasing lightning. Without lightning, the August mean anticyclone VMR for CO is 92.3 ± 2.8 ppbv. This is reduced to 89.8 ± 2.4 ppbv with $0.1\times$ lightning and 85.5 ± 2.4 ppbv with $1\times$ lightning. The anti-correlation of CO with LNO_x can be described by the dominating effect of reduced in-situ production of CO from (HCHO, GLY, MGLY) + OH over increased production from (OL2, OLT, OLI, ISO) + O₃. ¹⁵

Finally, O₃ is increased with increasing LNO_x, consistent with prior studies on this subject. Mean ozone VMR is increased from 74.5 ± 5.3 ppbv to 86.4 ± 6.7 ppbv (+16%) when adding $0.1\times$ LNO_x. At $1\times$ lightning, it is further increased to 101.1 ± 6.8 ppbv, a 26.6 ppbv or 36% increase relative to $0\times$ lightning. The reduced sensitivity to LNO_x at higher flash rate parameter is consistent with that of CO.

There is also a difference in the spin-up time for species in responding to LNO_x emission due to their respective lifetime in the atmosphere. While the differences in NO_x between simulations become apparent within the first day, HO_x requires two days, which is delayed by a separate spin-up from exchanging between HO_x and reservoir species. On the other hand, O₃ and CO begin to diverge after the fifth day of the simulation when the Z_{300} exceeded 9730 m for the first time. However, even after sufficient “spin-up,” the differences between simulations can be reduced again when air masses with minimal lightning influence are transported into the region.

Vertical structures are also affected. Figure 3.26 shows the vertical sensitivity profiles of ozone, CO, and NO_x from the base case and sensitivity simulations averaged within the anticyclone. With the exception of O₃ and NO_x in the $1\times$ lightning setting, the shapes of the mixing ratio vertical profiles are consistent across simulations. The greatest effect of the lightning-NO_x emissions on ozone occurs in the 300–500 hPa layer. The ozone mixing ratio increases by 33 ppbv in the $1\times$ lightning simulation over the 62 ppbv of ozone in the $0\times$ lightning simulation. The ozone chemical tendency also increases dramatically in this layer. Despite its LNO_x emission peak in the mid-troposphere, NO_x is enhanced most prominently at the 169 hPa level from 84 pptv to 3.09 ppbv. A more detailed discussion of this peak and its spin-up has been discussed in Section 3.2.5.

¹⁵ OL2=ethene; OLT=terminal alkenes; OLI=internal alkenes.

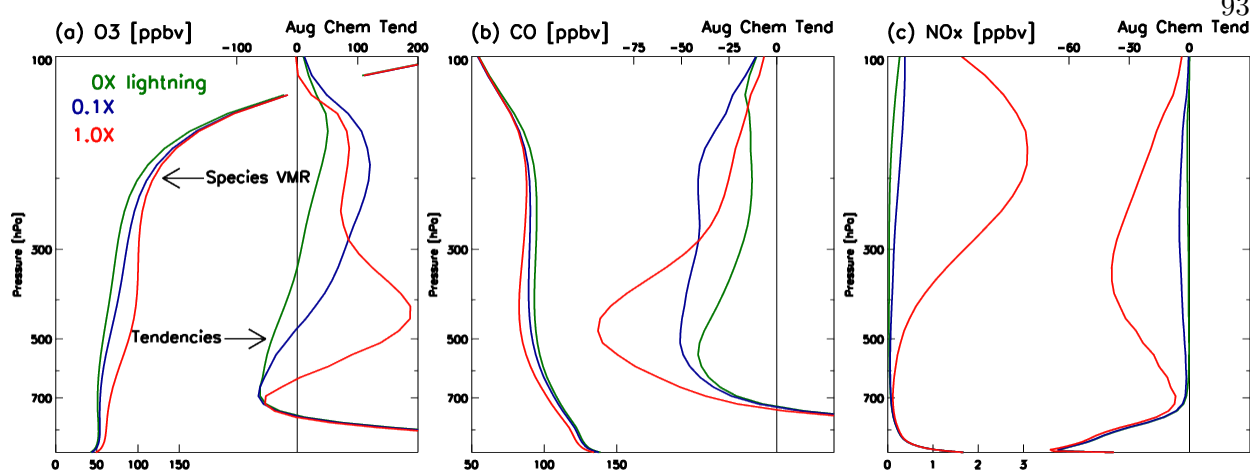


Figure 3.26: **Vertical profiles of O₃, CO, & NO_x**—August mean mixing ratios and accumulated chemical tendencies for (a) O₃, (b) CO, (c) NO_x within the anticyclone region for lightning emission factors 0× (green), 0.1× (blue), and 1× (red). Means are computed on model levels, and then gridded by the mean pressure.

In all simulations, the August mean ozone chemical tendency within the anticyclone drops below zero from the positive values in the boundary layer, then becomes positive again in the mid-to-upper troposphere. The level at which the sign of the accumulated chemical tendency changes according to the enhanced ozone production related to LNO_x emission. Without lightning, the lowest level observing positive chemical tendency in the free troposphere is ~ 340 hPa. With 0.1× LNO_x emission, the switch from negative chemical tendency to positive tendency drops to ~ 470 hPa. This is further lowered to ~ 630 hPa with 1× lightning emission. Thus, the vertical distribution of LNO_x, which impacts the vertical profile of ozone's sensitivity to the emission parameter, can directly influence the structure and vertical extent of the ozone enhancement by influencing the level at which net ozone production is attained.

In the upper troposphere, NO_x increases superlinearly due to LNO_x emissions between 0.1× and 1× lightning flash rate simulations, suggesting feedback. Consequently, the presence of high NO_x induces a decrease in the chemical production of O₃. NO_x titration has been suggested to be possible during intense thunderstorms (e.g. Cummings *et al.*, 2013). However, the persistent occurrence indicated in Figure 3.26 is in part due to overestimation of NO_x as a result of the 10× over-prediction in lightning flash rate. On the other hand, with the increased NO_x VMR,

a substantial amount of HO_x radicals are consumed by the reaction $\text{OH} + \text{NO}_2 \rightarrow \text{HNO}_3$, thus negatively affecting the efficiency of NO-to- NO_2 conversion.

Recall that the Houston time series shows significant nighttime negative tendencies (Fig. 3.23b), which partially negated the daytime accumulated production. To determine the response of ozone chemistry to lightning, it is thus necessary to take into account daytime versus nighttime chemistry. To do so, Figure 3.27 isolates daytime ozone chemical productions from its nighttime losses between 150–300 hPa within the anticyclone. The daytime tendencies are computed from 15–21 UTC and nighttime tendencies are computed from 3–9 UTC. The daytime/nighttime differences for species mixing ratios are negligible, and thus only daytime VMR distributions are shown. In conjunction with the mean values, the min-max ranges as well as the 5–95 percentiles are shown.

Due to the interconversion between O_3 and NO_2 , we examine odd oxygen $\text{O}_x \equiv \text{O}_3 + \text{NO}_2$ instead of NO_2 in the following analysis.

Changes in the ozone chemical tendencies between lightning emission scenarios are substantial. Without lightning, the mean daytime chemical tendency is 0.088 ppbv/hr and the 95-percentile is 0.259 ppbv/hr. With an additional $0.1 \times \text{LNO}_x$, the mean and 95-pct are respectively increased to 0.353 ppbv/hr and 0.904 ppbv/hr, a significantly shift away from the control ($0 \times$) scenario distribution. Further increasing LNO_x by a factor of 10 to the base case scenario ($1 \times \text{LNO}_x$), the daytime mean ozone chemical tendency is only slightly increased to 0.403 ppbv. Considering that

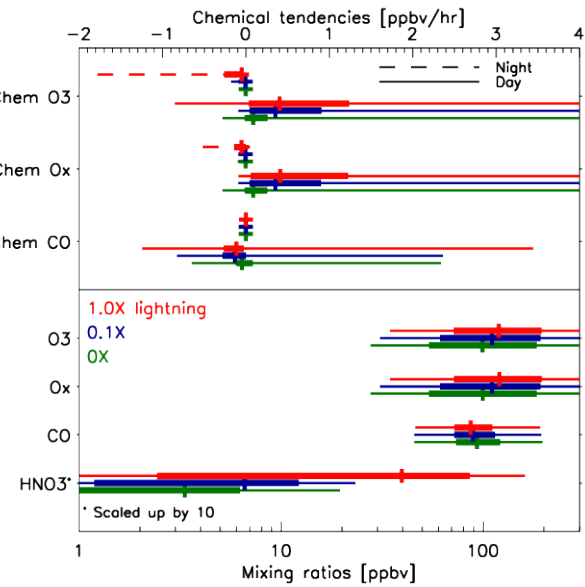


Figure 3.27: Daytime and nighttime chemical tendencies — Distributions (min-5pct-mean-95pct-max) of chemical tendencies mixing ratios for O_3 , O_x , CO and mixing ratio for HNO_3 between 150–300 hPa during August within the anticyclone. Nighttime (3–9 UTC) tendencies are represented by dashed lines while daytime (15–21 UTC) tendencies are represented by solid lines.

the combined all-day accumulated tendency, which decreased from $0.1 \times \text{LNO}_x$ to $1 \times \text{LNO}_x$, it is apparent that the nighttime loss phase plays an important role in modulating the response of ozone chemical tendency to lightning. However, the substantially lowered sensitivity still supports the conjecture that daytime NO_x -titration is occurring albeit not as severe as indicated in Figure 3.26.

By comparing the changes in the distribution of chemical tendencies of O_3 and O_x , it is apparent that the bulk of ozone losses at $1 \times$ is due to conversion to NO_2 . This argument is supported by the increase in NO_x as well as HNO_3 , which is increased from 6.6 ppbv at $0.1 \times$ lightning to 39.6 ppbv at $1 \times$ lightning emission.

The remainder of the reversal in the response of the O_3 chemical tendency to LNO_x after considering the daytime production is evidently substantial. Due to the absence of photolysis, the nighttime maximum tendencies are all near zero. Without production, we can define zero as the baseline and evaluate the sensitivities as relative changes. In the $0 \times$ scenario, the ozone loss is 0.90 pptv/hr with the 5 percentile at 2.93 pptv/hr. The mean loss is increased to 5 pptv/hr ($5.6 \times$) and the 5 percentile is increased to 25.8 pptv/hr ($8.8 \times$) with $0.1 \times \text{LNO}_x$. Increasing LNO_x to $1 \times$, the mean is now 48.2 pptv/hr, a $9.5 \times$ increase from the low(tuned)-lightning scenario, i.e. slightly sublinear compared to the increase in emission. The negative-end of the distribution, on the other hand, shows linear responses at both 5-percentile ($-0.0258 \rightarrow -0.259 \text{ ppbv/hr}$) and minimum ($-0.179 \rightarrow -1.78 \text{ ppbv/hr}$) from $0.1 \times$ to $1 \times$ emissions. However, the response is not linear for the tendency for O_x because of the potential for production (positive tendency) of NO_2 at nighttime, which is negligible with no lightning ($\max \Delta = 8 \times 10^{-2} \text{ pptv/hr}$), but increases to 79 pptv/hr with $1 \times$ lightning, which is comparable to the mean tendency (-51 pptv/hr). Despite production, response to lightning emission has became superlinear relative to a baseline of zero, wherein the O_x tendency for the two lightning scenarios are -4.3 and -51 pptv/hr . This points to loss of odd oxygens via both O_3 and NO_2 pathways at night.

Since CO precursors are generally scarce in the upper troposphere, and that OH VMR is low at night, neither production nor loss occur at appreciable rates. The nighttime CO chemical tendency ranges from -6.3 pptv/hr ($0.1 \times$) to 2.7 pptv/hr ($1 \times$). On the contrary, daytime CO chemical tendency

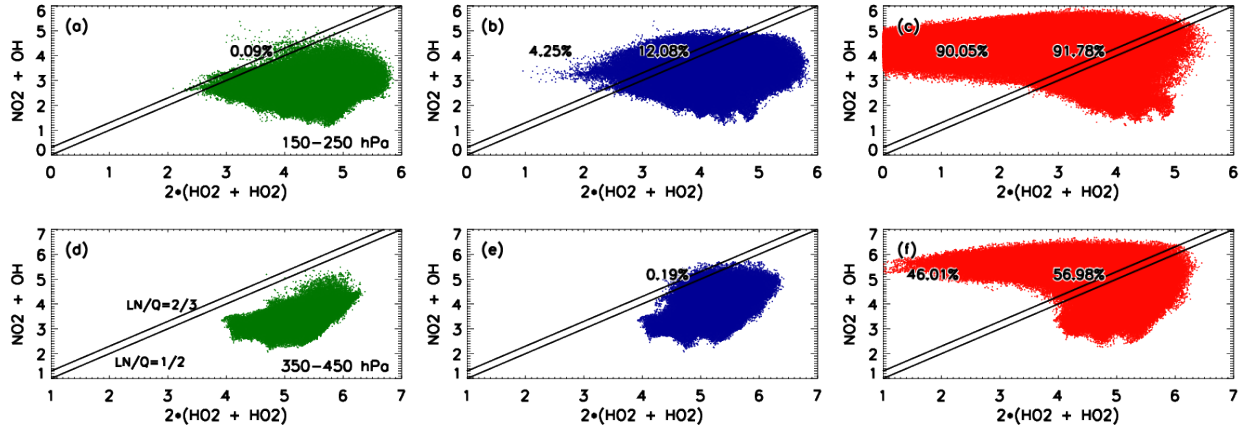


Figure 3.28: **HO_x radical termination** — Daytime reaction rates (\log_{10} molecules $\text{cm}^{-3} \text{s}^{-1}$) for $\text{NO}_2 + \text{OH}$ and $(2\times) \text{HO}_2 + \text{HO}_2$ at 150–250 hPa (a–c) and 350–450 hPa (d–f) without lightning (a,d), $0.1\times$ lightning (b,e), and $1\times$ lightning (c,f). The left percentage (if present) is the fraction of data points where $L_N/Q > 2/3$. The right percentage (if present) is that of $L_N/Q > 1/2$.

shows a substantial range relative to its mean values. The middle 90% spans $-109\text{--}80 \text{ pptv/hr}$ without lightning, with a mean of -46 pptv/hr . This indicates that sufficient CO precursors are present in the upper troposphere to counter the loss due to reaction with OH radicals. The addition of $0.1\times \text{LNO}_x$ moves this range to $-281\text{--}3 \text{ pptv/hr}$, thus doubling the net loss on the low end and essentially erasing any production. This is likely caused by losses of VOCs due to oxidation at lower levels, thus leaving less precursors available for in situ CO production in the upper troposphere after transport. At $1\times \text{LNO}_x$, however, the lower-end tendency trend is reversed and the net loss at 5-percentile is now -255 pptv/hr . These data points correspond to high-LNO_x air masses, in which OH radicals are competitively consumed by NO₂ in the production of HNO₃. At 95-percentile, the trend continues to decrease to a net 3-hourly loss of -25 pptv/hr with $1\times$ lightning emission, compared to the initial $+80 \text{ pptv/hr}$ without lightning.

To understand the source of the ozone chemical production reversal seen in the model results for high NO_x conditions, a steady-state analysis on ozone production and loss terms can be done following *Kleinman et al.* (1997). In a photostationary steady-state, the radical production rate Q is equal to the loss rates, characterized by radical-radical reactions L_R (e.g. $\text{HO}_2 + \text{HO}_2$) and radical-NO_x reactions L_N (e.g. $\text{NO}_2 + \text{OH}$). That is, $Q = L_R + L_N$. The response of ozone

production to the available NO can then be quantified as follow (*Kleinman et al.*, 1997):

$$\frac{d \ln P(O_3)}{d \ln[NO]} = \frac{(1 - 3/2 L_N/Q)}{(1 - 1/2 L_N/Q)} \quad (3.15)$$

where L_N/Q is the fraction of free radicals removed by NO_x . In the upper troposphere, L_N and L_R can be approximated by the reaction rate of $NO_2 + OH$ and twice the rate of $HO_2 + HO_2$, respectively. We conduct offline computations are performed using the rate equations and parameters from RADM2 (*Stockwell et al.*, 1990, and references therein). Using August data points at 15, 18, and 21 UTC within the anticyclone column between 150–250 hPa and 350–450 hPa, the reaction rates $L_N = k[NO_2][OH]$ and $L_R = 2k'[HO_2][HO_2]$ are plotted in Figure 3.28. *Kleinman et al.* (2001) show that conditions above $L_N/Q > 0.5$ represent a VOC-sensitive regime, compared to the NO_x -sensitive regime below this threshold. Further, $L_N/Q > 2/3$ represent NO_x -titration, i.e. more ozone is expected to be destroyed as a result of increasing NO_x , as demonstrated by Equation 3.15. Thus, if the majority of air mass lies above the 2/3 threshold, NO_x -titration is expected to occur as ozone loss caused by NO_x -titration compensated ozone production by the air mass of which $L_N/Q < 2/3$.

The percentage of data points where $L_N > L_R$, or $L_N/Q > 0.5$, and $L_N/Q > 2/3$ are computed at both levels for all 3 lightning sensitivity simulations. By suppressing lightning, almost all data points lie within $L_N/Q < 0.5$, which means that the atmosphere is NO_x -sensitive. With $0.1\times$ lightning, about 12% in the upper level exceeded this threshold, but almost all HO_x below 350 hPa continues to be terminated by radical-radical reactions. At $1\times$ lightning, 92% and 57% of the data points are within the VOC-limited regime ($L_N/Q > 0.5$)

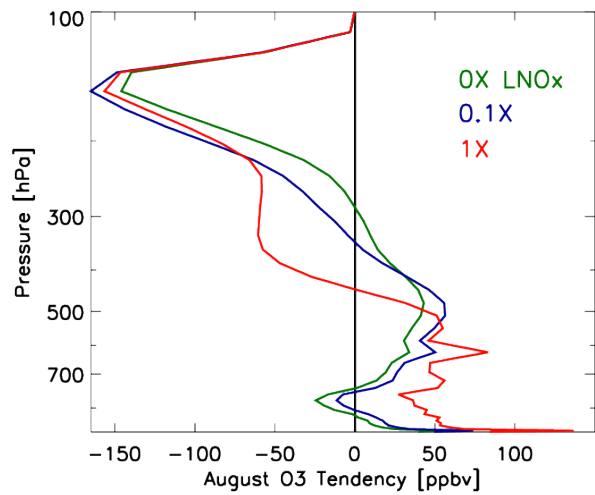


Figure 3.29: **Ozone convective tendency** — Vertical profiles of accumulated ozone convective tendency during August for the three lightning sensitivity simulations within the anticyclone column.

for the two pressure levels. The fraction of data points where the expected response of $P(O_3)$ to $[NO]$ is negative ($L_N/Q > 2/3$) are 90% for 150–250 hPa and 46% for 350–450 hPa. The observation that the majority of the data points are within the NO_x -titration regime, reversal in the ozone production trend is also expected as computed from the model.

Finally, due to changes in the vertical profiles of mixing ratios, and thus vertical gradients, convective tendencies are also affected by lightning emissions (Fig. 3.29). While it still holds true that convection dilutes upper tropospheric ozone by detraining ozone-poor air from the lower levels, changes in ozone due to convection are very different below the maximum detrainment level between emission scenarios. In particular, due to the deeper enhancement (high ozone at lower altitude), a net negative convective tendency is observed above 440 hPa with $1\times$ lightning. Lightning emission also impacts surface air quality via the mid-to-upper tropospheric ozone enhancement, as observed by the increasingly positive tendencies below 600 hPa. The accumulated ozone enhancement in the lower troposphere is increased by 40–60 ppbv from $0\times$ to $1\times$ lightning despite a much smaller in situ chemical production within the BL (Fig. 3.26a).

In conclusion, the results of the lightning sensitivity experiment can be summarized as follow:

- (1) Lightning-generated NO_x is partially but primarily responsible for the ozone enhancement observed by instruments and simulated by the model. This is consistent with all previous studies (e.g. *Li et al.*, 2005; *Cooper et al.*, 2007; *Barth et al.*, 2012);
- (2) By increasing from the tuned-lightning scenario ($0.1\times$) to the untuned scenario ($1\times$), upper tropospheric NO_x experiences super-linear increases.
- (3) Excessive NO_x in the upper troposphere causes NO_x -titration, which causes ozone loss in both the $0.1\times$ and $1\times$ lightning emission scenarios.

3.4.2 Anthropogenic emission

To evaluate how anthropogenic emission affects the ozone enhancement, a simulation is performed without the prescribed EPA emission. Lightning emission is kept at $1\times$, i.e. the untuned

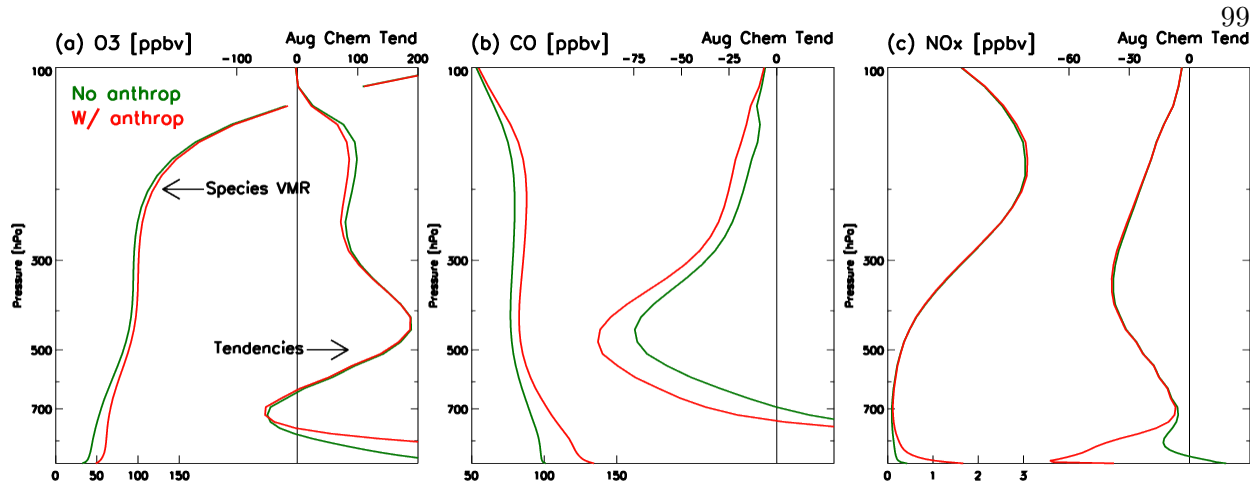


Figure 3.30: **Vertical profiles for sensitivity to anthropogenic emission** — Same as Fig. 3.26, but for anthropogenic emission.

scenario. By cutting off anthropogenic emission, both surface VOC and NO_x sources are decreased. The differences ($[X] - [X]_0$) between the base case scenario and the no-emission scenario are shown in Figure 3.31, where $[X]_0$ is the VMRs without emission, thus a positive value represents an increase due to anthropogenic emission.

Within the anticyclone column at 300 hPa (Fig. 3.31b), ozone due to anthropogenic emission is 5.9 ± 1.0 ppbv with a maximum of 7.8 ppbv with respect to a VMR ~ 100 ppbv. Similarly, sensitivity of CO at 300 hPa to anthropogenic emission is 7.2 ± 1.6 ppbv with a maximum of 11.5 ppbv (Fig. 3.31e). The upper tropospheric O₃ and CO responses positively to anthropogenic emission, while NO_x decreases with the addition of emission up to 300 hPa but reverses at 150 hPa. Response of NO_x at 150 ppbv is 54 ± 34 pptv. This is reversed to -19 ± 9 pptv at 300 hPa but decreases in magnitude to -1.3 ± 6.7 pptv, which is negligible compared to the 1–3 ppbv VMR at these levels (for the 1× lightning scenario).

At 150 hPa, all three species shown in Figure 3.31 show maximum responses over northern Huntsville and neighboring areas, Alabama. This changes at 300 hPa, where two distinct maxima are shown for O₃ and CO, corresponding to the maxima of CO over the northeast corner of Texas and along Blue Ridge Mountain as shown in Figure 3.10. On the other hand, NO_x responses neutrally (-2.3 ± 8.0 pptv) at these locations relative to the surrounding area where negative responses are

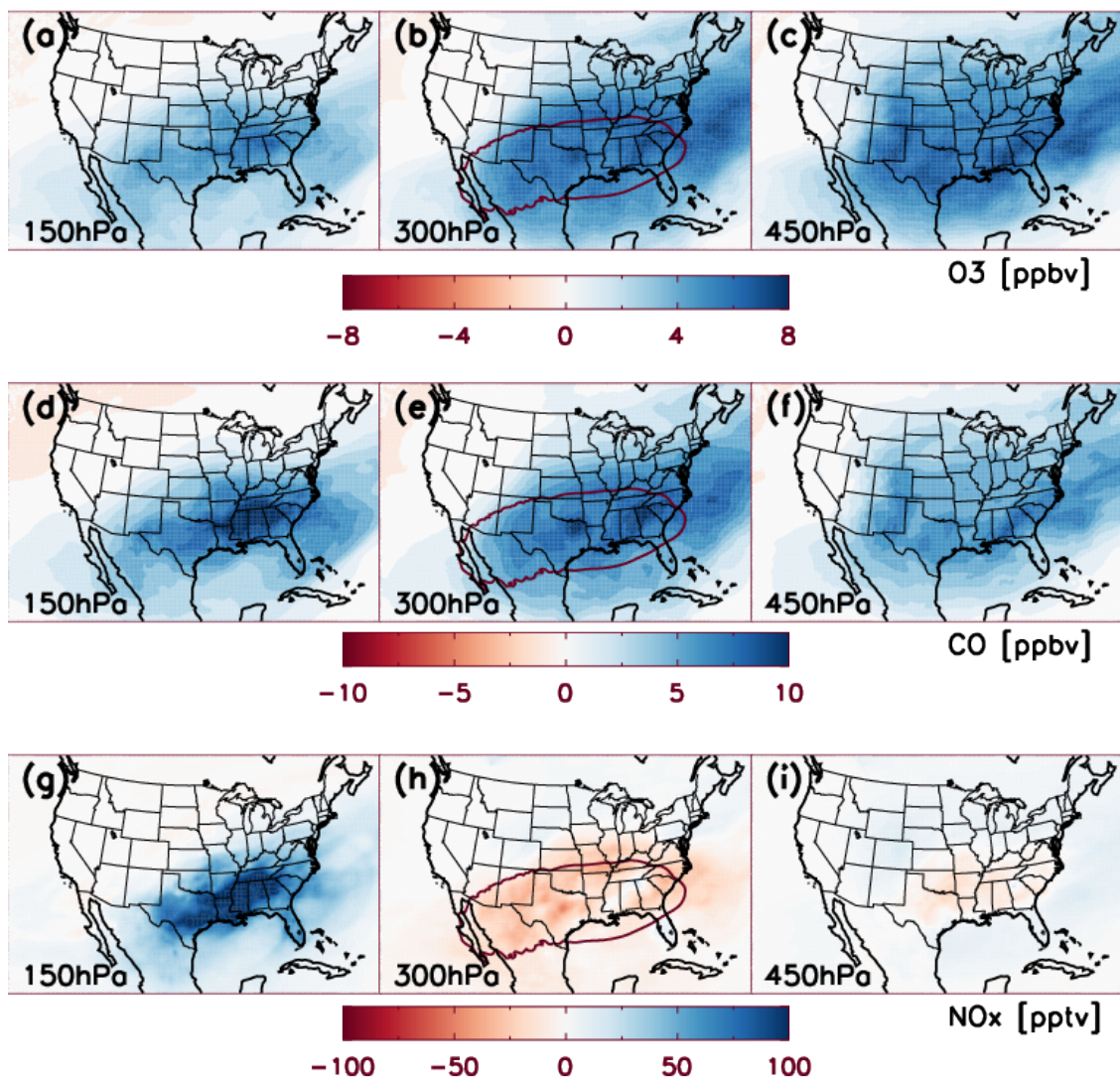


Figure 3.31: **Spatial distribution of sensitivity to anthropogenic emissions** — Base case VMRs due to anthropogenic emission during August at 150, 300, and 450 hPa for (a–c) O₃, (d–f) CO, and (g–i) NO_x. The differences are defined as VMRs without emission subtracted from VMRs with emission. Geopotential height contour $Z_{300} = 9730\text{ m}$ is shown at 300 hPa.

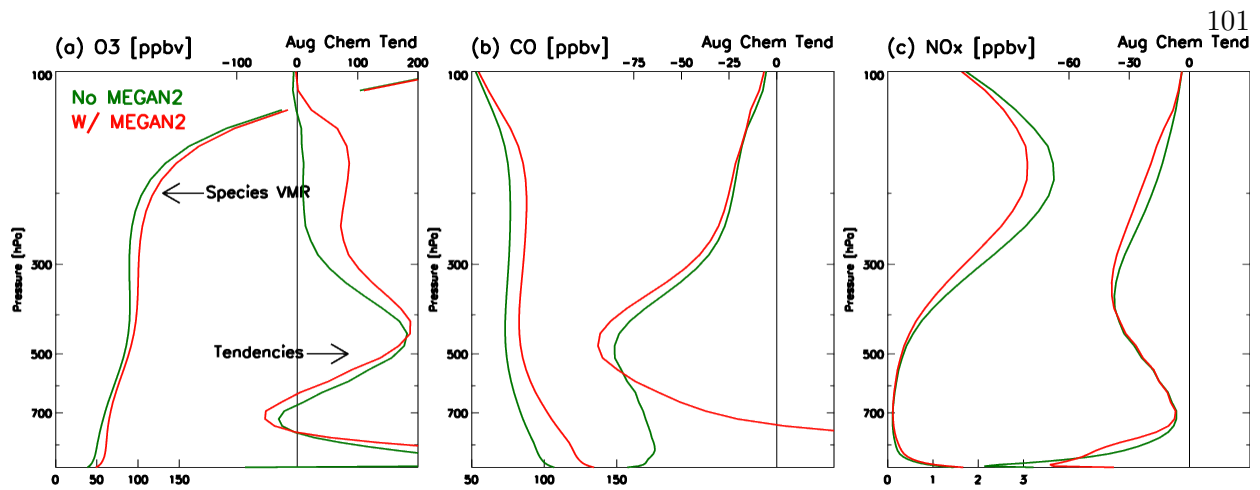


Figure 3.32: **Vertical profiles for sensitivity to biogenic emission** — Same as Fig. 3.26, but for biogenic emission.

prevalent (Fig. 3.31h). Even though $\Delta[\text{NO}_x]$ is negligible, ozone is still sensitive to changes in [CO] and thus enhancement is still possible as further discussed below.

Significant responses of chemical tendency to anthropogenic emission stops at $\sim 700 \text{ hPa}$ in the anticyclone column mean (Fig. 3.30). Changes in BL air composition allows moderate changes in the upper tropospheric ozone production through convective transport. As shown in Figure 3.30c, both NO_x mixing ratios and NO_x chemistry are negligibly sensitive to the anthropogenic emission with the prescribed level of LNO_x , thus the changes in ozone chemical tendency in Figure 3.30a is controlled by changes in CO (or VOC) and its chemistry (Fig. 3.30b).

3.4.3 Biogenic emission

Biogenic emission contributes significantly to tropospheric ozone production, emitting over $7\times$ the VOC from transportation within CONUS and dominating the budget in rural areas (Sect. 1.1.1). *Li et al.* (2005) also estimated $\sim 5 \text{ ppbv}$ contribution to the ozone enhancement by biogenic emission alone for July 2000. Similar to anthropogenic emission, biogenic emission can modify the chemical composition throughout the entire tropospheric column through convective transport and chemistry.

To quantify the impact of biogenic emission on the upper tropospheric ozone and related chemistry within the anticyclone, we conduct a sensitivity simulation that excludes biogenic emissions. Ozone chemical tendency at 200 hPa show significant sensitivity to the absence/presence of biogenic emissions. At this level, the biogenic emissions enhance ozone by 13 ± 3 ppbv as a result of $+70 \pm 38$ ppbv accumulated ozone chemical tendency over August. CO has a similar change in VMR ($+11 \pm 3$ ppbv) from the addition of biogenic emissions, but the enhancement is not due to local chemical production ($\Delta_{chem} = -2 \pm 5$ ppbv). Rather, most of the enhancement in CO in the upper troposphere is due to convective transport of enhanced CO from the lower troposphere. On the other hand, NO_x experiences a decrease of 0.60 ± 0.17 ppbv due to an increased accumulated loss of 6.2 ± 4.0 ppbv. These values can be compared to results by *Li et al.* (2005), who showed > 30 ppbv CO and ~ 5 ppbv O₃ enhancement due to biogenic emission.

Despite sharing the same originating level (BL) and transport pathways with anthropogenic emission sources, differences in the emitted species composition and density are sufficient in producing different vertical profiles in the response. In particular, ozone chemical tendency in the upper troposphere shows significant reduction when biogenic emission is turned off. As opposed to being driven by VOCs as it is for anthropogenic emission, this change is due to the increased NO_x in the absence of biogenic emission (Fig. 3.32). In other words, the emission of biogenic species such as isoprene and formaldehyde causes ozone to increase in the upper troposphere by decreasing NO_x within the NO_x-titration regime (see Sect. 3.4.1).

3.5 Conclusions

WRF-Chem simulations are performed with the goals of understanding the structure and chemical pathways of the 2006 upper tropospheric ozone enhancement during the North American Monsoon. Using an untuned ($1\times$) lightning flash rate parameterization based on a modified *Price and Rind* (1992) lightning flash rate parameterization, the predicted flash rate is about an order of magnitude higher compared to the scaled NLDN history. This overestimation is shown to cause overly strong ozone enhancement compared to TES and IONS-06 observation. On the other hand, CO is shown to be either biased high (against TES) or biased low (against MOPITT). However, both validation exercises show that the simulated CO distribution is more homogeneous than observed by either instruments.

Under the base case condition, the simulated NO_x mixing ratio is seen rapidly increasing during the first 5 days of the simulation by almost a factor of 10. Validation against SCIAMACHY NO_2 retrieval shows that the model is simulating too much high NO_x events while properly predicting the mode of the distribution.

Tracer-tracer correlation using O_3 and CO shows that the conditions within and outside of the anticyclone are similar but differ in specific features. Using passive tracers, it is shown that the anticyclone region distinguishes itself by lateral boundary tracers and lightning tracers, and that boundary layer and stratospheric tracers are dominated by orographic features instead of the upper air circulation. This result differs from those of *Cooper et al.* (2007) and *Barth et al.* (2012), who showed enhanced residence time and presence of boundary layer air/tracers within the anticyclone. Instead, we conclude that the lack of externality, i.e. lack of influence of air mixing in from “clean” regions, and presence of both surface and lightning emissions are the key ingredients for the observed enhancement.

Other than the enhanced ozone mixing ratio, chemical and convective tendencies within the anticyclone region also show different structures compared to the continental inflow (Trinidad Head, CA) and outflow (Beltsville, MD) regions. In particular, while a mid-tropospheric net chemical

loss (or minimal production) is observed outside the anticyclone, a maximum ozone production is simulated for this level, which subsequently lowers the level at which the net in situ ozone production is positive and thus enhancing ozone mixing ratio.

To quantify the impact of the uncertainties and biases of LNO_x emission on the observed atmospheric composition within the anticyclone, sensitivity simulations are performed by disabling (0×) and tuning (0.1×) the emission factor. Using the three simulations, it is concluded that the decreases in HO_x radicals as a result of increasing NO_x cause the response of NO_x to be superlinear to LNO_x. By evaluating the radical termination pathways, it is also concluded that NO_x-titration is indeed occurring at the level of maximum NO_x enhancement and thus reducing the potential ozone enhancement with increasing LNO_x. Moreover, the modified vertical distribution responding to the changing LNO_x emission, convective tendencies are also affected.

Finally, control simulations for anthropogenic and biogenic emissions are performed to evaluate the contributions to the ozone enhancement by boundary layer emissions relative to the base case (1×) scenario. While anthropogenic emission leads to VOC-controlled changes, biogenic emission leads to major changes via perturbation of upper tropospheric NO_x. Since the upper tropospheric chemistry is experiencing NO_x-titration, the reduction of NO_x (as a result of biogenic emission) leads to a 70 ppbv increase in the August accumulated chemical tendency at the detrainment level. Comparing the three emission sources, lightning is the highest contributing factor to the ozone enhancement, followed by biogenic emission, and finally anthropogenic emission. However, because of the over-prediction of lightning-generated NO_x in the base case scenario, our result does not necessarily contradict with *Li et al.* (2005), who showed that anthropogenic (NO_x) emission is the dominant source of the ozone enhancement under a LNO_x emission scenario perhaps comparable to our 0.1× lightning scenario.

Table 3.1: Examples of how species are mapped from EPA NEI to RADM2 for anthropogenic emission in the case study.

NEI species	RADM2 species	Weight factor	Description
CO	co	1.00	Carbon monoxide
NOX	no	1.00	nitrogen oxides
SO2	so2	1.00	Sulfur dioxide
HC02	eth	1.00	Ethane $kOH < 500 \text{ ppm}^{-1} \text{ min}^{-1}$
HC03	hc3	1.00	Alkane $500 < kOH < 2500$ ^a
HC04	hc3	1.11	Alkane $2500 < kOH < 5000$ ^b
HC05	hc5	0.97	Alkane $5000 < kOH < 1e4$ ^c
HC06	hc8	1.00	Alkane $kOH > 1e4$
HC07	ol2	1.00	Ethylene
...			
HC18	ket	0.33	Acetone
HC19	ket	1.61	Methylethyl ketone
HC20	ket	1.61	PRD2 SAPRAC species (ketone)
...			
PM01	pm25i	0.20	Unspeciated nuclei mode PM2.5
PM01	pm25j	0.80	Unspeciated accumulation mode PM2.5
...			

^a Excluding C₃H₈, C₂H₂, organic acids.

^b Excluding butanes.

^c Excluding pentanes.

Table 3.2: Locations and sample sizes of IONS-06 ozonesonde August data used in this study. N_{launches} is the number of days during August with launches performed. N_{levels} is the number of vertical levels/measurements recorded during each launch.

Location	Coordinates	N_{launches}	N_{levels}	Comments
Beltsville, MD	39.0N, 76.5W	7	3017–5196	^a
Boulder, CO	40.0N, 105.2W	30	2451–6142	^b
Bratts Lake, Sask.	50.2N, 104.7W	29	619–1108	
Egbert, Ont	44.2N, 79.8W	15	598–870	
Holtville, CA	32.8N, 115.4W	13	2857–6394	^b
Houston, TX	29.7N, 95.3W	17	1350–4273	^{a, b}
Huntsville, AL	34.7N, 86.6W	29	4716–6622	
Kelowna, B.C.	49.9N, 119.4W	27	208–787	
Narragansett, RI	41.5N, 71.4W	28	3358–6187	
Paradox, NY	43.9N, 73.6W	5	1979–3980	
R/V R.H. Brown	—	23	5158–9802	^{a, b, c}
Socorro, NM	34.6N, 106.9W	25	2944–6684	
Table Mountain, CA	34.4N, 117.7W	31	138–4726	^b
Trinidad Head, CA	40.8N, 124.2W	30	3752–6257	^b
Valparaiso, IN	41.5N, 87.0W	5	2103–4129	^b
Wallops Is, VA	37.9N, 75.7W	11	406–703	
Walsingham, Ont	42.6N, 80.6W	12	365–1108	^a
Yarmouth, N.S.	43.9N, 66.1W	13	504–734	

^a Launched twice on certain days, only first launches (L1's) are used.

^b Since model terminates on August 31 at 00 UTC, launches on August 31 are omitted.

^c Launches from the Ronald H. Brown research vessel (R/V) on the Gulf of Mexico.

Table 3.3: Using $VCD = 4.39 \times 10^{15} \text{ molec. cm}^{-2}$ as a threshold, the following statistics summarize the two partitions.

Partition	$n(\%)$	Regression	r^2	χ^2_{reduced}	$P(> \chi^2_{\text{reduced}})$ [†]
$VCD > 4.39$	29997 (58.1%)	$y = 2.76 + 2.21x$	0.09	51.76	~ 0
$VCD < 4.39$	21641 (41.9%)	$y = 0.49 + 0.42x$	0.332	0.911	~ 1

[†] Probability that a fit has a reduced- χ^2 higher than the given fit. High P 's correspond to “good” fits.

Chapter 4

Summary

Ozone in the troposphere acts as a greenhouse gas and causes harm to the ecosystem. The recurring upper tropospheric ozone enhancement during the North American Monsoon has been shown to perturb upper tropospheric ozone by more than 20 ppbv above background values, which leads to a radiative forcing up to 0.50 W m^{-2} (*Li et al.*, 2005; *Cooper et al.*, 2007; *Choi et al.*, 2009). Of all the meteorological and chemical processes that contributes to the ozone enhancement, lightning-generated nitrogen oxides (lightning NO_x, or LNO_x), is shown to be the most prominent factor, which contributes 25–30 ppbv of the ozone maximum at 250 hPa (*Cooper et al.*, 2007). It is important to note that LNO_x emission is largely unconstrained with a global annual estimate of $5 \pm 3 \text{ Tg a}^{-1}$ (*Schumann and Huntrieser*, 2007). Despite the uncertainty, only a few studies have investigated LNO_x or lightning flash rate parameterization at the regional scale (e.g. *Allen et al.*, 2010, 2012; *Barth et al.*, 2012; *Wong et al.*, 2013). Despite advancements in the physical formulations for the parameterization (*Barthe et al.*, 2010, and references therein), the *Price and Rind* (PR92; 1992) method based on cloud top height continues to show merits despite its own limitations (*Boccippio*, 2002).

To apply PR92 to the 2006 case study, we have implemented PR92 into WRF-Chem (Apdx C). The performance of this implementation has been evaluated (*Wong et al.*, 2013, and Ch. 2) and the results are summarized as follow. It is found that the statistics generated by a 3-month meteorological simulation are comparable ($\sim 2.4 \times$ for 2006, $\sim 1 \times$ for 2011) to observations from NLDN and ENTLN with a 2- km cloud-top reduction, which is included to reconcile the differences between the

level of neutral buoyancy (LNB) cloud-top proxy and radar reflectivity cloud-top. This reduction is selected to be an appropriate adjustment given a sufficiently large number of convective events. Thus, it does not guarantee applicability for individual storm. However, the IC : CG ratio produced by the *Price and Rind* (1993, PR93) method is shown to generate a erroneous drop-off in the histogram and is thus deemed unreliable. Finally, it is shown that the resolution dependency factor from *Price and Rind* (1994, PR94) is not applicable for a convective parameterized model due to the interpretation of cloud-top heights within a grid. To reconcile differences in model resolution, we suggest scaling by areal ratio to 36 km, at which convective core density (number of core per grid) is expected to be close to unity. However, it should be noted that the base resolution (36 km) may vary spatially or dependent or storm scale.

Due to differences in the simulated meteorology, flash rate is overestimated by a factor 10 in the 2006 case study, compared to the factor of 2 from the simulation evaluated in Chapter 2. The overpredicted LNO_x emission subsequently leads to a more severe upper tropospheric ozone enhancement. The ozone mixing ratio is simulated to be about 21% higher than that observed by TES. Similarly, CO is shown to be high compared to TES due to lower OH as the result of excessive O₃ and NO_x, but validation against MOPITT shows negligibly low biases in the upper troposphere. Formaldehyde is validated against SCIAMACHY retrievals from KNMI TEMIS. Because of the high uncertainties (σ_N) in the retrieved values, majority of the data points lie within $\pm 1\sigma$ despite low apparent correlations. On the other hand, NO₂ is shown to be over-predicted for events $> 2 \times 10^{15} \text{ molec. cm}^{-2}$, which is expected due to excessive LNO_x.

The differences between the chemistry within the anticyclone and that outside are evaluated based on tracer-tracer correlations, passive tracer diagnostics, and tendency diagnostics. It is concluded that contrary to previous studies, the NAM anticyclonic circulation does not sufficiently increase the amount of boundary layer air detrained into the upper troposphere above that in the surrounding area. On the other hand, the lack of influence from the air outside the anticyclone on the air inside, as quantified by the tracer-tracer correlations and lateral boundary tracers, sufficiently distinguishes the composition within the anticyclone from that outside.

To quantify the impact of model biases as well as the sensitivity of ozone to LNO_x emissions, additional simulations are performed without lightning and with reduced lightning tuned according to the flash rate validation. It is shown that as a result of the super-linear response of upper tropospheric NO_x mixing ratios to LNO_x, ozone production crosses the threshold beyond which NO_x-titration occurs, thus reducing and eventually reversing the sensitivity at the detrainment level (150–250 hPa). Furthermore, changes in the ozone vertical profile due to lightning emission also sufficiently modified the vertical gradients, which subsequently affected the resulting convective tendencies, thus forming a nonlinear feedback between convective transport and chemistry.

The contributions to the ozone enhancement from anthropogenic and biogenic emissions are also examined through sensitivity experiments, wherein the respective emission sources are suppressed. In the experiment pertaining anthropogenic emission, VOC, with CO as the proxy, is observed to be the controlling factor in the sensitivity. Due to NO_x-titration, upper tropospheric ozone production responds negatively to the increase in anthropogenic emission. On the other hand, biogenic emission is responsible for NO_x-losses in the upper troposphere (within the NO_x-titration regime), which subsequently allows higher net ozone production (again, within the NO_x-titration regime). It should be noted that this result is partially a consequence of excessive LNO_x within the model, which pushes the upper tropospheric chemistry into the NO_x-titration regime. A similar experiment is conducted by *Li et al.* (2005) and found that enhancements in CO as a result of these emissions are the primary pathway of how these chemical sources contribute to the ozone enhancement.

In conclusion, and directly responding to the questions raised in Chapter 1:

- (1) WRF-Chem is able to simulate the occurrence of the ozone enhancement despite an order of magnitude bias in NO_x as the result of parameterizing lightning based on parameterized convection;
- (2) In situ chemical production is the dominating tendency for the long term variability of the ozone enhancement after filtering out the advective component. However, contrary to

results from previous studies (e.g. *Li et al.*, 2005; *Cooper et al.*, 2007; *Barth et al.*, 2012), the anticyclone does not create a distinctive region wherein boundary layer air is aged above levels in the surrounding area;

- (3) Lightning-generated NO_x emission is responsible for 16% increase in upper tropospheric ozone at 0.1× lightning and 36% at 1× lightning at 300 hPa. On the other hand, anthropogenic emission is responsible for ∼ 6% and biogenic emission is responsible for ∼ 13% with 1× LNO_x emission.

4.1 Perspectives and outlook

Despite the ozone enhancement being a relatively self-contained feature, its spatial structures and chemical pathways are highly non-uniform and its response to perturbations in the emission scenarios are often not monotonic. Thus, to obtain more definitive results, studies focusing on specific scenarios and conditions are required to narrow down on specific chemical or meteorological regimes. In order words, it is insufficient to simply define a process such as convective transport and examine its link to the ozone enhancement. Furthermore, the initially super-linear sensitivity to lightning-generated NO_x also demands a finely tuned lightning parameterization or one that is less sensitive to biases in the convective parameterization, which is further complicated by the feedbacks between chemistry and convective transport. Several potential improvements to this study and remaining questions follow.

First and foremost, flash rate assimilation, as done by *Cooper et al.* (2009), can potentially increase the fidelity of lightning NO_x emission in the model and thus the ozone chemistry. As total lightning monitoring instruments are being expanded or deployed (e.g. NLDN, ENTLN, GOES-R), and the data becoming available, it is possible to revisit this approach again. However, because the vertical distribution of LNO_x emission has significant impacts on the resulting ozone chemistry (*Pickering et al.*, 1998), it is also important to guarantee that convection and lightning collocate. Thus, short simulations that re-initialize frequently may be the preferred mode of simulation as

opposed to season-long simulations for the flash-rate-assimilated approach to avoid model drift in meteorology.

Second, as the “base case” simulation in this study ($1\times$ lightning) is considered a high-LNO_x scenario, the anthropogenic emission and biogenic emission sensitivity experiments require additional scenarios using the tuned parameter ($0.1\times$ lightning) as the base case. However, in doing so, a full validation-diagnostic study is required to evaluate the $0.1\times$ scenario, much like what has been done in Section 3.2 and 3.3 for the $1\times$ lightning scenario. Furthermore, as emphasized earlier, nonlinearity is a key feature in the sensitivity of ozone to these emission sources, thus the two data points presented in this study are insufficient in fully characterizing the response curve. On the other hand, as these two sources are relatively constrained compared to lightning, it is probably more useful to perform perturbations based on realistic projections instead of order of magnitude changes to explore extreme scenarios.

Finally, while it has been shown that anthropogenic and biogenic emissions affect the ozone enhancement through different mechanisms, the precise chemical pathways are yet to be determined. Therefore, to complete this part of the study, analyses aiming to understand the differences in chemistry are recommended. Examples of the suggested analyses have already been done for the sensitivity of ozone to LNO_x emission (see Sect. 3.4.1) as well as for peroxy radical formation by *Barth et al.* (2012). However, the large number of emitted species from anthropogenic and biogenic sources, and subsequently the number of reactions involved, will undoubtedly complicate the analysis. Hence, it is recommended that these studies be performed with minimal scope to maximize focus.

References

- Allen, D., K. Pickering, G. Stenchikov, A. Thompson, and Y. Kondo (2000), A three-dimensional total odd nitrogen (NO_y) simulation during SONEX using a stretched-grid chemical transport model, *J. Geophys. Res.*, 105(D3), 3851–3876, doi:10.1029/1999JD901029.
- Allen, D., K. Pickering, B. Duncan, and M. Damon (2010), Impact of lightning NO emissions on North American photochemistry as determined using the Global Modeling Initiative (GMI) model, *J. Geophys. Res.*, 115(D22), doi:10.1029/2010JD014062.
- Allen, D. J., and K. E. Pickering (2002), Evaluation of lightning flash rate parameterizations for use in a global chemical transport model, *J. Geophys. Res.*, 107(D23).
- Allen, D. J., K. E. Pickering, R. W. Pinder, B. H. Henderson, K. W. Appel, and A. Prados (2012), Impact of lightning-NO on eastern United States photochemistry during the summer of 2006 as determined using the CMAQ model, *Atmos. Chem. Phys.*, 12(4), 1737–1758, doi: 10.5194/acp-12-1737-2012.
- Baker, M. B., H. J. Christian, and J. Latham (1995), A computational study of the relationships linking lightning frequency and other thundercloud parameters, *Quarterly Journal of the Royal Meteorological Society*, 121(527), 1525–1548, doi:10.1002/qj.49712152703.
- Barth, M. C., J. Lee, A. Hodzic, G. Pfister, W. C. Skamarock, J. Worden, J. Wong, and D. Noone (2012), Thunderstorms and upper troposphere chemistry during the early stages of the 2006 North American Monsoon, *Atmos. Chem. Phys.*, 12(22), 11,003–11,026, doi: 10.5194/acp-12-11003-2012.
- Barthe, C., and J.-P. Pinty (2007), Simulation of a supercellular storm using a three-dimensional mesoscale model with an explicit lightning flash scheme, *J. Geophys. Res.*, 112(D6).
- Barthe, C., G. Molinié, and J.-P. Pinty (2005), Description and first results of an explicit electrical scheme in a 3D cloud resolving model, *Atmospheric Research*, 76(1–4), 95–113, doi:<http://dx.doi.org/10.1016/j.atmosres.2004.11.021>.
- Barthe, C., W. Deierling, and M. C. Barth (2010), Estimation of total lightning from various storm parameters: A cloud-resolving model study, *J. Geophys. Res.*, 115(D24), doi:10.1029/2010JD014405.
- Beer, R. (2006), TES on the aura mission: scientific objectives, measurements, and analysis overview, *Geoscience and Remote Sensing, IEEE Transactions on*, 44(5), 1102–1105.

- Boccippio, D. J. (2002), Lightning Scaling Relations Revisited, *Journal of the Atmospheric Sciences*, 59(6), 1086–1104, doi:10.1175/1520-0469(2002)059\$(\$1086:LSRR\$)\$2.0.CO;2.
- Boccippio, D. J., W. Koshak, R. Blakeslee, K. Driscoll, D. Mach, D. Buechler, W. Boeck, H. J. Christian, and S. J. Goodman (2000), The Optical Transient Detector (OTD): Instrument Characteristics and Cross-Sensor Validation, *Journal of Atmospheric and Oceanic Technology*, 17(4), 441–458, doi:10.1175/1520-0426(2000)017<0441:TOTDOI>2.0.CO;2.
- Boccippio, D. J., K. L. Cummins, H. J. Christian, and S. J. Goodman (2001), Combined Satellite- and Surface-Based Estimation of the Intracloud–Cloud-to-Ground Lightning Ratio over the Continental United States, *Monthly Weather Review*, 129(1), 108–122.
- Boersma, K. F., H. J. Eskes, and E. J. Brinksma (2004), Error analysis for tropospheric NO₂ retrieval from space, *J. Geophys. Res.*, 109(D4), doi:10.1029/2003JD003962.
- Borucki, W. J., and W. L. Chameides (1984), Lightning: Estimates of the rates of energy dissipation and nitrogen fixation, *Reviews of Geophysics*, 22(4), 363–372, doi:10.1029/RG022i004p00363.
- Bouarar, I., et al. (2011), Emission sources contributing to tropospheric ozone over Equatorial Africa during the summer monsoon, *Atmos. Chem. Phys.*, 11(24), 13,395–13,419, doi:10.5194/acp-11-13395-2011.
- Bovensmann, H., J. P. Burrows, M. Buchwitz, J. Frerick, S. Noël, V. V. Rozanov, K. V. Chance, and A. P. H. Goede (1999), SCIAMACHY: Mission Objectives and Measurement Modes, *Journal of the Atmospheric Sciences*, 56(2), 127–150, doi:10.1175/1520-0469(1999)056\$(\$0127:SMOAMM\$)\$2.0.CO;2.
- Brown, D., J. Worden, and D. Noone (2008), Comparison of atmospheric hydrology over convective continental regions using water vapor isotope measurements from space, *J. Geophys. Res.*, 113(D15), doi:10.1029/2007JD009676.
- Burrows, J. P., E. Hlzel, A. P. H. Goede, H. Visser, and W. Fricke (1995), SCIAMACHY—scanning imaging absorption spectrometer for atmospheric chartography, *Acta Astronautica*, 35(7), 445–451.
- Chen, F., and J. Dudhia (2001), Coupling an Advanced Land Surface–Hydrology Model with the Penn State–NCAR MM5 Modeling System. Part II: Preliminary Model Validation, *Monthly Weather Review*, 129(4), 587–604, doi:10.1175/1520-0493(2001)129<0587:CAALSH>2.0.CO;2.
- Chin, M., D. J. Jacob, J. W. Munger, D. D. Parrish, and B. G. Doddridge (1994), Relationship of ozone and carbon monoxide over North America, *Journal of Geophysical Research: Atmospheres*, 99(D7), 14,565–14,573, doi:10.1029/94JD00907.
- Choi, Y., Y. Wang, T. Zeng, R. V. Martin, T. P. Kurosu, and K. Chance (2005), Evidence of lightning NO_x and convective transport of pollutants in satellite observations over North America, *Geophysical Research Letters*, 32(2), L02,805, doi:10.1029/2004GL021436.
- Choi, Y., J. Kim, A. Eldering, G. Osterman, Y. L. Yung, Y. Gu, and K. N. Liou (2009), Lightning and anthropogenic NO_x sources over the United States and the western North Atlantic Ocean: Impact on OLR and radiative effects, *Geophys. Res. Lett.*, 36(17).

- Chou, M.-D., M. J. Suarez, C.-H. Ho, M. M.-H. Yan, and K.-T. Lee (1998), Parameterizations for Cloud Overlapping and Shortwave Single-Scattering Properties for Use in General Circulation and Cloud Ensemble Models, *Journal of Climate*, 11(2), 202–214, doi:10.1175/1520-0442(1998)011<0202:PFCOAS>2.0.CO;2.
- Christian, H. J., et al. (2003), Global frequency and distribution of lightning as observed from space by the Optical Transient Detector, *Journal of Geophysical Research: Atmospheres*, 108(D1), 4005, doi:10.1029/2002JD002347.
- Cooper, O. R., et al. (2006), Large upper tropospheric ozone enhancements above midlatitude North America during summer: In situ evidence from the IONS and MOZAIC ozone measurement network, *J. Geophys. Res.*, 111(D24).
- Cooper, O. R., et al. (2007), Evidence for a recurring eastern North America upper tropospheric ozone maximum during summer, *J. Geophys. Res.*, 112(D23).
- Cooper, O. R., et al. (2009), Summertime buildup and decay of lightning NO_x and aged thunderstorm outflow above North America, *J. Geophys. Res.*, 114(D1).
- Cristofanelli, P., et al. (2013), Influence of biomass burning and anthropogenic emissions on ozone, carbon monoxide and black carbon at the Mt. Cimone GAW-WMO global station (Italy, 2165 m a.s.l.), *Atmos. Chem. Phys.*, 13(1), 15–30, doi:10.5194/acp-13-15-2013.
- Cummings, K. A., T. L. Huntemann, K. E. Pickering, M. C. Barth, W. C. Skamarock, H. Höller, H. D. Betz, A. Volz-Thomas, and H. Schlager (2013), Cloud-resolving chemistry simulation of a Hector thunderstorm, *Atmos. Chem. Phys.*, 13(5), 2757–2777, doi:10.5194/acp-13-2757-2013.
- Cummins, K., and M. Murphy (2009), An Overview of Lightning Locating Systems: History, Techniques, and Data Uses, With an In-Depth Look at the U.S. NLDN, *Electromagnetic Compatibility, IEEE Transactions on*, 51(3), 499 –518, doi:10.1109/TEMC.2009.2023450.
- De Smedt, I., J. F. Müller, T. Stavrakou, R. van der A, H. Eskes, and M. Van Roozendael (2008), Twelve years of global observations of formaldehyde in the troposphere using GOME and SCIAMACHY sensors, *Atmos. Chem. Phys.*, 8(16), 4947–4963, doi:10.5194/acp-8-4947-2008.
- De Smedt, I., T. Stavrakou, J. F. Müller, R. J. van der A, and M. Van Roozendael (2010), Trend detection in satellite observations of formaldehyde tropospheric columns, *Geophys. Res. Lett.*, 37(18), doi:10.1029/2010GL044245.
- DeCaria, A. J., K. E. Pickering, G. L. Stenchikov, J. R. Scala, J. L. Stith, J. E. Dye, B. A. Ridley, and P. Laroche (2000), A cloud-scale model study of lightning-generated NO_x in an individual thunderstorm during STERAO-A, *J. Geophys. Res.*, 105(D9), 11,601–11,616.
- DeCaria, A. J., K. E. Pickering, G. L. Stenchikov, and L. E. Ott (2005), Lightning-generated NO_x and its impact on tropospheric ozone production: A three-dimensional modeling study of a Stratosphere-Troposphere Experiment: Radiation, Aerosols and Ozone (STERAO-A) thunderstorm, *J. Geophys. Res.*, 110(D14).
- Deeter, M. N., et al. (2003), Operational carbon monoxide retrieval algorithm and selected results for the MOPITT instrument, *J. Geophys. Res.*, 108(D14), doi:10.1029/2002JD003186.

- Deeter, M. N., et al. (2010), The MOPITT version 4 CO product: Algorithm enhancements, validation, and long-term stability, *J. Geophys. Res.*, 115(D7), doi:10.1029/2009JD013005.
- Deeter, M. N., S. Martínez-Alonso, D. P. Edwards, L. K. Emmons, J. C. Gille, H. M. Worden, J. V. Pittman, B. C. Daube, and S. C. Wofsy (2013), Validation of MOPITT Version 5 Thermal-Infrared, Near-Infrared, and Multispectral Carbon Monoxide Profile Retrievals for 2000-2011, *Journal of Geophysical Research: Atmospheres*, pp. n/a–n/a, doi:10.1002/jgrd.50272.
- Deierling, W., and W. A. Petersen (2008), Total lightning activity as an indicator of updraft characteristics, *J. Geophys. Res.*, 113(D16), doi:10.1029/2007JD009598.
- Dickerson, R. R., et al. (1987), Thunderstorms: An Important Mechanism in the Transport of Air Pollutants, *Science*, 235(4787), 460–465.
- Drummond, J. R., and G. S. Mand (1996), The Measurements of Pollution in the Troposphere (MOPITT) Instrument: Overall Performance and Calibration Requirements, *Journal of Atmospheric and Oceanic Technology*, 13(2), 314–320, doi:10.1175/1520-0426(1996)013\$(\$0314: TMOPIT\$)2.0.CO;2.
- Dufour, G., F. Wittrock, M. Camredon, M. Beekmann, A. Richter, B. Aumont, and J. P. Burrows (2009), SCIAMACHY formaldehyde observations: constraint for isoprene emission estimates over Europe?, *Atmos. Chem. Phys.*, 9(5), 1647–1664, doi:10.5194/acp-9-1647-2009.
- Emmons, L. K., et al. (2010), Description and evaluation of the Model for Ozone and Related chemical Tracers, version 4 (MOZART-4), *Geosci. Model Dev.*, 3(1), 43–67.
- EPA (2012), 40 CFR 51.100(s), Code of Federal Regulations.
- Futyan, J. M., and A. D. Del Genio (2007), Relationships between lightning and properties of convective cloud clusters, *Geophys. Res. Lett.*, 34(15).
- Gauss, M., et al. (2006), Radiative forcing since preindustrial times due to ozone change in the troposphere and the lower stratosphere, *Atmos. Chem. Phys.*, 6(3), 575–599, doi:10.5194/acp-6-575-2006.
- Grell, G. A. (1993), Prognostic Evaluation of Assumptions Used by Cumulus Parameterizations, *Monthly Weather Review*, 121(3), 764–787.
- Grell, G. A., and D. Devenyi (2002), A generalized approach to parameterizing convection combining ensemble and data assimilation techniques, *Geophys. Res. Lett.*, 29(14).
- Grell, G. A., S. E. Peckham, R. Schmitz, S. A. McKeen, G. Frost, W. C. Skamarock, and B. Eder (2005), Fully coupled "online" chemistry within the WRF model, *Atmospheric Environment*, 39(37), 6957–6975.
- Guenther, A., T. Karl, P. Harley, C. Wiedinmyer, P. I. Palmer, and C. Geron (2006), Estimates of global terrestrial isoprene emissions using MEGAN (Model of Emissions of Gases and Aerosols from Nature), *Atmos. Chem. Phys.*, 6(11), 3181–3210.
- Hairer, E., S. S. P. Nrsett, and G. Wanner (1993), *Solving Ordinary Differential Equations II: Stiff and Differential-Algebraic Problems*, Springer.

- Hansen, A. E., H. E. Fuelberg, and K. E. Pickering (2010), Vertical distributions of lightning sources and flashes over Kennedy Space Center, Florida, *J. Geophys. Res.*, 115(D14), doi:10.1029/2009JD013143.
- Hansen, A. E., H. E. Fuelberg, K. E. Pickering, S. E. Peckham, and R. E. Hart (2012), Lightning NO_x Parameterization for WRF-Chem At the Regional Scale, in *92nd Amer. Meteor. Soc. Annual Meeting*, New Orleans, Louisiana.
- Hauglustaine, D., et al. (2001), On the Role of Lightning NO_x in the Formation of Tropospheric Ozone Plumes: A Global Model Perspective, *Journal of Atmospheric Chemistry*, 38(3), 277–294–294.
- Hegarty, J., H. Mao, and R. Talbot (2010), Winter- and summertime continental influences on tropospheric O₃ and CO observed by TES over the western North Atlantic Ocean, *Atmos. Chem. Phys.*, 10(8), 3723–3741, doi:10.5194/acp-10-3723-2010.
- Hegglin, M. I., C. D. Boone, G. L. Manney, and K. A. Walker (2009), A global view of the extratropical tropopause transition layer from Atmospheric Chemistry Experiment Fourier Transform Spectrometer O₃, H₂O, and CO, *Journal of Geophysical Research: Atmospheres*, 114(D7), D00B11, doi:10.1029/2008JD009984.
- Ho, S.-P., D. P. Edwards, J. C. Gille, M. Luo, G. B. Osterman, S. S. Kulawik, and H. Worden (2009), A global comparison of carbon monoxide profiles and column amounts from Tropospheric Emission Spectrometer (TES) and Measurements of Pollution in the Troposphere (MOPITT), *J. Geophys. Res.*, 114(D21).
- Hong, S.-Y., Y. Noh, and J. Dudhia (2006), A New Vertical Diffusion Package with an Explicit Treatment of Entrainment Processes, *Monthly Weather Review*, 134(9), 2318–2341.
- Hudman, R. C., et al. (2007), Surface and lightning sources of nitrogen oxides over the United States: Magnitudes, chemical evolution, and outflow, *J. Geophys. Res.*, 112(D12).
- Janjić, Z. I. (1994), The Step-Mountain Eta Coordinate Model: Further Developments of the Convection, Viscous Sublayer, and Turbulence Closure Schemes, *Monthly Weather Review*, 122(5), 927–945, doi:10.1175/1520-0493(1994)122<0927:TSMECM>2.0.CO;2.
- Jayaratne, E. R., and C. P. R. Saunders (1985), Thunderstorm electrification: The effect of cloud droplets, *Journal of Geophysical Research: Atmospheres*, 90(D7), 13,063–13,066, doi:10.1029/JD090iD07p13063.
- Jourdain, L., S. S. Kulawik, H. M. Worden, K. E. Pickering, J. Worden, and A. M. Thompson (2010), Lightning NO_x emissions over the USA constrained by TES ozone observations and the GEOS-Chem model, *Atmos. Chem. Phys.*, 10(1), 107–119.
- Justice, C. O., et al. (2002), The MODIS fire products, *Remote Sensing of Environment*, 83(1–2), 244–262, doi:[http://dx.doi.org/10.1016/S0034-4257\(02\)00076-7](http://dx.doi.org/10.1016/S0034-4257(02)00076-7).
- Kar, J., et al. (2004), Evidence of vertical transport of carbon monoxide from Measurements of Pollution in the Troposphere (MOPITT), *Geophysical Research Letters*, 31(23), L23,105, doi:10.1029/2004GL021128.

- Kiehl, J. T., T. L. Schneider, R. W. Portmann, and S. Solomon (1999), Climate forcing due to tropospheric and stratospheric ozone, *Journal of Geophysical Research: Atmospheres*, 104(D24), 31,239–31,254, doi:10.1029/1999JD900991.
- Kim, S. W., et al. (2009), NO₂ columns in the western United States observed from space and simulated by a regional chemistry model and their implications for NO_x emissions, *Journal of Geophysical Research: Atmospheres*, 114(D11), D11,301, doi:10.1029/2008JD011343.
- Kim, S. W., et al. (2011), Evaluations of NO_x and highly reactive VOC emission inventories in Texas and their implications for ozone plume simulations during the Texas Air Quality Study 2006, *Atmos. Chem. Phys.*, 11(22), 11,361–11,386, doi:10.5194/acp-11-11361-2011.
- Kleinman, L. I., P. H. Daum, J. H. Lee, Y.-N. Lee, L. J. Nunnermacker, S. R. Springston, L. Newman, J. Weinstein-Lloyd, and S. Sillman (1997), Dependence of ozone production on NO and hydrocarbons in the troposphere, *Geophysical Research Letters*, 24(18), 2299–2302, doi:10.1029/97GL02279.
- Kleinman, L. I., P. H. Daum, Y.-N. Lee, L. J. Nunnermacker, S. R. Springston, J. Weinstein-Lloyd, and J. Rudolph (2001), Sensitivity of ozone production rate to ozone precursors, *Geophysical Research Letters*, 28(15), 2903–2906, doi:10.1029/2000GL012597.
- Labrador, L. J., R. von Kuhlmann, and M. G. Lawrence (2005), The effects of lightning-produced NO_x and its vertical distribution on atmospheric chemistry: sensitivity simulations with MATCH-MPIC, *Atmos. Chem. Phys.*, 5(7), 1815–1834, doi:10.5194/acp-5-1815-2005.
- Lacis, A. A., D. J. Wuebbles, and J. A. Logan (1990), Radiative forcing of climate by changes in the vertical distribution of ozone, *Journal of Geophysical Research: Atmospheres*, 95(D7), 9971–9981, doi:10.1029/JD095iD07p09971.
- Lamarque, J. F., G. P. Brasseur, P. G. Hess, and J. F. Müller (1996), Three-dimensional study of the relative contributions of the different nitrogen sources in the troposphere, *Journal of Geophysical Research: Atmospheres*, 101(D17), 22,955–22,968, doi:10.1029/96JD02160.
- Lamarque, J. F., P. Hess, L. Emmons, L. Buja, W. Washington, and C. Granier (2005), Tropospheric ozone evolution between 1890 and 1990, *J. Geophys. Res.*, 110(D8).
- Lamarque, J. F., et al. (2010), Historical (1850–2000) gridded anthropogenic and biomass burning emissions of reactive gases and aerosols: methodology and application, *Atmos. Chem. Phys.*, 10(15), 7017–7039, doi:10.5194/acp-10-7017-2010.
- Lamarque, J. F., et al. (2012), CAM-chem: description and evaluation of interactive atmospheric chemistry in the Community Earth System Model, *Geosci. Model Dev.*, 5(2), 369–411, doi:10.5194/gmd-5-369-2012.
- Lambert, J.-C., et al. (2004), Geophysical Validation of SCIAMACHY NO₂ vertical columns: overview of early 2004 results, in *Proceedings of the Second Workshop on the Atmospheric Chemistry Validation of ENVISAT (ACVE-2)*, ESC01JL2, ESA-ESRIN, Frascati, Italy.
- Langford, A. O., C. J. Senff, R. M. Banta, R. M. Hardesty, I. Alvarez, R. J., S. P. Sandberg, and L. S. Darby (2009), Regional and local background ozone in Houston during Texas Air Quality Study 2006, *J. Geophys. Res.*, 114.

- Levelt, P. F., G. H. J. Van den Oord, M. R. Dobber, A. Malkki, H. Visser, J. de Vries, P. Stammes, J. O. V. Lundell, and H. Saari (May 2006), The ozone monitoring instrument, *Geoscience and Remote Sensing, IEEE Transactions on*, 44(5), 1093–1101, doi:10.1109/TGRS.2006.872333.
- Li, Q., D. J. Jacob, R. Park, Y. Wang, C. L. Heald, R. Hudman, R. M. Yantosca, R. V. Martin, and M. Evans (2005), North American pollution outflow and the trapping of convectively lifted pollution by upper-level anticyclone, *J. Geophys. Res.*, 110(D10).
- Lin, Y.-L., R. D. Farley, and H. D. Orville (1983), Bulk Parameterization of the Snow Field in a Cloud Model, *Journal of Climate and Applied Meteorology*, 22(6), 1065–1092, doi:10.1175/1520-0450(1983)022<1065:BPOTSF>2.0.CO;2.
- Liu, C., and S. Heckman (2011), Using total lightning data in severe storm prediction: Global case study analysis from north America, Brazil and Australia, in *Lightning Protection (XI SIPDA), 2011 International Symposium on*, pp. 20–24.
- Logan, J. A., I. Megretskaya, R. Nassar, L. T. Murray, L. Zhang, K. W. Bowman, H. M. Worden, and M. Luo (2008), Effects of the 2006 El Niño on tropospheric composition as revealed by data from the Tropospheric Emission Spectrometer (TES), *Geophysical Research Letters*, 35(3), L03,816, doi:10.1029/2007GL031698.
- Lopez, J. P., M. Luo, L. E. Christensen, M. Loewenstein, H. Jost, C. R. Webster, and G. Osterman (2008), TES carbon monoxide validation during two AVE campaigns using the Argus and ALIAS instruments on NASA's WB-57F, *Journal of Geophysical Research: Atmospheres*, 113(D16), D16S47, doi:10.1029/2007JD008811.
- Luo, M., et al. (2007a), Comparison of carbon monoxide measurements by TES and MOPITT: Influence of a priori data and instrument characteristics on nadir atmospheric species retrievals, *Journal of Geophysical Research: Atmospheres*, 112(D9), doi:10.1029/2006JD007663.
- Luo, M., et al. (2007b), TES carbon monoxide validation with DACOM aircraft measurements during INTEX-B 2006, *J. Geophys. Res.*, 112(D24), D24S48, doi:10.1029/2007JD008803.
- MacGorman, D. R., and W. D. Rust (1998), *The electrical nature of storms*, Oxford University Press, Incorporated.
- Madronich, S. (1987), Photodissociation in the atmosphere: 1. Actinic flux and the effects of ground reflections and clouds, *Journal of Geophysical Research: Atmospheres*, 92(D8), 9740–9752, doi:10.1029/JD092iD08p09740.
- Mansell, E. R., D. R. MacGorman, C. L. Ziegler, and J. M. Straka (2002), Simulated three-dimensional branched lightning in a numerical thunderstorm model, *J. Geophys. Res.*, 107(D9), doi:10.1029/2000JD000244.
- Marais, E. A., et al. (2012), Isoprene emissions in Africa inferred from OMI observations of formaldehyde columns, *Atmos. Chem. Phys.*, 12(14), 6219–6235, doi:10.5194/acp-12-6219-2012.
- Martini, M., D. J. Allen, K. E. Pickering, G. L. Stenchikov, A. Richter, E. J. Hyer, and C. P. Loughner (2011), The impact of North American anthropogenic emissions and lightning on long-range transport of trace gases and their export from the continent during summers 2002 and 2004, *J. Geophys. Res.*, 116(D7), doi:10.1029/2010JD014305.

- McMillan, W. W., et al. (2010), An observational and modeling strategy to investigate the impact of remote sources on local air quality: A Houston, Texas, case study from the Second Texas Air Quality Study (TexAQS II), *J. Geophys. Res.*, *115*(D1), doi:10.1029/2009JD011973.
- Michalon, N., A. Nassif, T. Saouri, J. F. Royer, and C. A. Pontikis (1999), Contribution to the climatological study of lightning, *Geophys. Res. Lett.*, *26*(20), 3097–3100.
- Millet, D. B., D. J. Jacob, K. F. Boersma, T.-M. Fu, T. P. Kurosu, K. Chance, C. L. Heald, and A. Guenther (2008), Spatial distribution of isoprene emissions from North America derived from formaldehyde column measurements by the OMI satellite sensor, *Journal of Geophysical Research: Atmospheres*, *113*(D2), D02307, doi:10.1029/2007JD008950.
- Mlawer, E. J., S. J. Taubman, P. D. Brown, M. J. Iacono, and S. A. Clough (1997), Radiative transfer for inhomogeneous atmospheres: RRTM, a validated correlated-k model for the longwave, *Journal of Geophysical Research: Atmospheres*, *102*(D14), 16,663–16,682, doi:10.1029/97JD00237.
- Müller, J.-F. (1992), Geographical distribution and seasonal variation of surface emissions and deposition velocities of atmospheric trace gases, *Journal of Geophysical Research: Atmospheres*, *97*(D4), 3787–3804, doi:10.1029/91JD02757.
- Nassar, R., et al. (2008), Validation of Tropospheric Emission Spectrometer (TES) nadir ozone profiles using ozonesonde measurements, *J. Geophys. Res.*, *113*(D15).
- Niemeyer, L., L. Pietronero, and H. J. Wiesmann (1984), Fractal Dimension of Dielectric Breakdown, *Physical Review Letters*, *52*(12), 1033–1036.
- Oltmans, S. J., et al. (2006), Long-term changes in tropospheric ozone, *Atmospheric Environment*, *40*(17), 3156–3173.
- Orville, R. E., G. R. Huffines, W. R. Burrows, R. L. Holle, and K. L. Cummins (2002), The North American Lightning Detection Network (NALDN)—First Results: 1998–2000, *Monthly Weather Review*, *130*(8), 2098–2109.
- Orville, R. E., G. R. Huffines, W. R. Burrows, and K. L. Cummins (2010), The North American Lightning Detection Network (NALDN)—Analysis of Flash Data: 2001–09, *Monthly Weather Review*, *139*(5), 1305–1322, doi:10.1175/2010MWR3452.1.
- Ott, L. E., K. E. Pickering, G. L. Stenchikov, D. J. Allen, A. J. DeCaria, B. Ridley, R.-F. Lin, S. Lang, and W.-K. Tao (2010), Production of lightning NO_x and its vertical distribution calculated from three-dimensional cloud-scale chemical transport model simulations, *J. Geophys. Res.*, *115*(D4).
- Palmer, P. I., et al. (2001), Air mass factor formulation for spectroscopic measurements from satellites: Application to formaldehyde retrievals from the Global Ozone Monitoring Experiment, *Journal of Geophysical Research: Atmospheres*, *106*(D13), 14,539–14,550, doi:10.1029/2000JD900772.
- Palmer, P. I., D. J. Jacob, A. M. Fiore, R. V. Martin, K. Chance, and T. P. Kurosu (2003), Mapping isoprene emissions over North America using formaldehyde column observations from space, *Journal of Geophysical Research: Atmospheres*, *108*(D6), 4180, doi:10.1029/2002JD002153.

- Palmer, P. I., et al. (2006), Quantifying the seasonal and interannual variability of North American isoprene emissions using satellite observations of the formaldehyde column, *Journal of Geophysical Research: Atmospheres*, 111(D12), D12,315, doi:10.1029/2005JD006689.
- Pan, L. L., J. C. Wei, D. E. Kinnison, R. R. Garcia, D. J. Wuebbles, and G. P. Brasseur (2007), A set of diagnostics for evaluating chemistry-climate models in the extratropical tropopause region, *J. Geophys. Res.*, 112(D9).
- Park, M., W. J. Randel, A. Gettelman, S. T. Massie, and J. H. Jiang (2007), Transport above the Asian summer monsoon anticyclone inferred from Aura Microwave Limb Sounder tracers, *Journal of Geophysical Research: Atmospheres*, 112(D16), D16,309, doi:10.1029/2006JD008294.
- Petersen, W. A., H. J. Christian, and S. A. Rutledge (2005), TRMM observations of the global relationship between ice water content and lightning, *Geophys. Res. Lett.*, 32(14), doi:10.1029/2005GL023236.
- Pickering, K. E., Y. Wang, W.-K. Tao, C. Price, and J.-F. Müller (1998), Vertical distributions of lightning NO_x for use in regional and global chemical transport models, *J. Geophys. Res.*, 103(D23), 31,203–31,216.
- Price, C., and D. Rind (1992), A Simple Lightning Parameterization for Calculating Global Lightning Distributions, *J. Geophys. Res.*, 97(D9), 9919–9933.
- Price, C., and D. Rind (1993), What determines the cloud-to-ground lightning fraction in thunderstorms?, *Geophys. Res. Lett.*, 20(6), 463–466, doi:10.1029/93GL00226.
- Price, C., and D. Rind (1994), Modeling Global Lightning Distributions in a General Circulation Model, *Monthly Weather Review*, 122(8), 1930–1939.
- Price, C., J. Penner, and M. Prather (1997), NO_x from lightning 1. Global distribution based on lightning physics, *J. Geophys. Res.*, 102(D5), 5929–5941, doi:10.1029/96JD03504.
- Reynolds, S. E., M. Brook, and M. F. Gourley (1957), Thunderstorm chare separation, *Journal of Meteorology*, 14(5), 426–436, doi:10.1175/1520-0469(1957)014(0426:TCS)2.0.CO;2.
- Risi, C., S. Bony, F. Vimeux, C. Frankenberg, D. Noone, and J. Worden (2010), Understanding the Sahelian water budget through the isotopic composition of water vapor and precipitation, *J. Geophys. Res.*, 115(D24), doi:10.1029/2010JD014690.
- Rossow, W., and R. Schiffler (1991), ISCCP cloud data products, *Bull. Amer. Meteorol. Soc.*, 71, 2–20.
- Sandu, A., and R. Sander (2006), Technical note: Simulating chemical systems in Fortran90 and Matlab with the Kinetic PreProcessor KPP-2.1, *Atmos. Chem. Phys.*, 6(1), 187–195.
- Saunders, C. P. R., H. Bax-norman, C. Emersic, E. E. Avila, and N. E. Castellano (2006), Laboratory studies of the effect of cloud conditions on graupel/crystal charge transfer in thunderstorm electrification, *Quarterly Journal of the Royal Meteorological Society*, 132(621), 2653–2673, doi:10.1256/qj.05.218.
- Schumann, U., and H. Huntrieser (2007), The global lightning-induced nitrogen oxides source, *Atmos. Chem. Phys.*, 7(14), 3823–3907, doi:10.5194/acp-7-3823-2007.

- Shim, C., et al. (2007), Characterizing mega-city pollution with TES O₃ and CO measurements, *Atmos. Chem. Phys. Discuss.*, 7(5), 15,189–15,212, doi:10.5194/acpd-7-15189-2007.
- Skamarock, W. C. (2006), Positive-Definite and Monotonic Limiters for Unrestricted-Time-Step Transport Schemes, *Monthly Weather Review*, 134(8), 2241–2250.
- Skamarock, W. C., J. E. Dye, E. Defer, M. C. Barth, J. L. Stith, B. A. Ridley, and K. Baumann (2003), Observational- and modeling-based budget of lightning-produced NO_x in a continental thunderstorm, *J. Geophys. Res.*, 108(D10).
- Skamarock, W. C., J. B. Klemp, J. Dudhia, D. O. Gill, D. M. Barker, M. G. Duda, X.-Y. Huang, W. Wang, and J. G. Powers (2008), *A description of the Advanced Research WRF Version 3*, NCAR Tech. Note, NCAR/TN-475+STR.
- Skamarock, W. C., J. B. Klemp, M. G. Duda, L. D. Fowler, S.-H. Park, and T. D. Ringler (2012), A Multiscale Nonhydrostatic Atmospheric Model Using Centroidal Voronoi Tesselations and C-Grid Staggering, *Monthly Weather Review*, 140(9), 3090–3105, doi:10.1175/MWR-D-11-00215.1.
- Smit, H. G. J., et al. (2007), Assessment of the performance of ECC-ozonesondes under quasi-flight conditions in the environmental simulation chamber: Insights from the Juelich Ozone Sonde Intercomparison Experiment (JOSIE), *J. Geophys. Res.*, 112(D19).
- Smith, P. L., C. G. Myers, and H. D. Orville (1975), Radar Reflectivity Factor Calculations in Numerical Cloud Models Using Bulk Parameterization of Precipitation, *Journal of Applied Meteorology*, 14(6), 1156–1165, doi:10.1175/1520-0450(1975)014<1156:RRFCIN>2.0.CO;2.
- Stark, M. S., J. T. H. Harrison, and C. Anastasi (1996), Formation of nitrogen oxides by electrical discharges and implications for atmospheric lightning, *Journal of Geophysical Research: Atmospheres*, 101(D3), 6963–6969, doi:10.1029/95JD03008.
- Stevenson, D. S., C. E. Johnson, W. J. Collins, R. G. Derwent, K. P. Shine, and J. M. Edwards (1998), Evolution of tropospheric ozone radiative forcing, *Geophysical Research Letters*, 25(20), 3819–3822, doi:10.1029/1998GL900037.
- Stevenson, D. S., et al. (2006), Multimodel ensemble simulations of present-day and near-future tropospheric ozone, *J. Geophys. Res.*, 111(D8).
- Stockwell, W. R., P. Middleton, J. S. Chang, and X. Tang (1990), The Second Generation Regional Acid Deposition Model Chemical Mechanism for Regional Air Quality Modeling, *J. Geophys. Res.*, 95(D10), 16,343–16,367.
- Stohl, A., C. Forster, A. Frank, P. Seibert, and G. Wotawa (2005), Technical note: The Lagrangian particle dispersion model FLEXPART version 6.2, *Atmos. Chem. Phys.*, 5(9), 2461–2474, doi:10.5194/acp-5-2461-2005.
- Stolzenburg, M., W. D. Rust, and T. C. Marshall (1998), Electrical structure in thunderstorm convective regions: 3. Synthesis, *Journal of Geophysical Research: Atmospheres*, 103(D12), 14,097–14,108, doi:10.1029/97JD03545.
- Takahashi, H., and Z. Luo (2012), Where is the level of neutral buoyancy for deep convection?, *Geophysical Research Letters*, 39(15), L15,809, doi:10.1029/2012GL052638.

- Tarasick, D. W., et al. (2007), Comparison of Canadian air quality forecast models with tropospheric ozone profile measurements above midlatitude North America during the IONS/ICARTT campaign: Evidence for stratospheric input, *J. Geophys. Res.*, 112(D12).
- Thompson, A. M., et al. (2007a), Intercontinental Chemical Transport Experiment Ozonesonde Network Study (IONS) 2004: 1. Summertime upper troposphere/lower stratosphere ozone over northeastern North America, *J. Geophys. Res.*, 112(D12).
- Thompson, A. M., et al. (2007b), Intercontinental Chemical Transport Experiment Ozonesonde Network Study (IONS) 2004: 2. Tropospheric ozone budgets and variability over northeastern North America, *J. Geophys. Res.*, 112(D12).
- Thompson, A. M., J. E. Yorks, S. K. Miller, J. C. Witte, K. M. Dougherty, G. A. Morris, D. Baumgardner, L. Ladino, and B. Rappenglück (2008a), Tropospheric ozone sources and wave activity over Mexico City and Houston during MILAGRO/Intercontinental Transport Experiment (INTEX-B) Ozonesonde Network Study, 2006 (IONS-06), *Atmos. Chem. Phys.*, 8(17), 5113–5125.
- Thompson, G., P. R. Field, R. M. Rasmussen, and W. D. Hall (2008b), Explicit Forecasts of Winter Precipitation Using an Improved Bulk Microphysics Scheme. Part II: Implementation of a New Snow Parameterization, *Monthly Weather Review*, 136(12), 5095–5115.
- Tie, X., S. Madronich, S. Walters, R. Zhang, P. Rasch, and W. Collins (2003), Effect of clouds on photolysis and oxidants in the troposphere, *J. Geophys. Res.*, 108(D20).
- Tost, H., P. Jöckel, and J. Lelieveld (2007), Lightning and convection parameterisations – uncertainties in global modelling, *Atmos. Chem. Phys.*, 7(17), 4553–4568.
- Uman, M. A., and E. P. Krider (1989), Natural and Artificially Initiated Lightning, *Science*, 246(4929), 457–464, doi:10.1126/science.246.4929.457.
- Ushio, T., S. J. Heckman, D. J. Boccippio, H. J. Christian, and Z.-I. Kawasaki (2001), A survey of thunderstorm flash rates compared to cloud top height using TRMM satellite data, *J. Geophys. Res.*, 106(D20), 24,089–24,095, doi:10.1029/2001JD900233.
- van der A, R. J., H. J. Eskes, M. Van Roozendael, I. De Smedt, N. Blond, F. Boersma, A. Weiss, and J. C. A. van Peet (2010), Tropospheric NO₂, *Algorithm Document TEM/AD1/001*, TEMIS.
- Vonnegut, B. (1963), Some facts and speculation concerning the origin and role of thunderstorm electricity, *Meteor. Monogr.*, (27), 224–241.
- Voulgarakis, A., P. J. Telford, A. M. Aghedo, P. Braesicke, G. Faluvegi, N. L. Abraham, K. W. Bowman, J. A. Pyle, and D. T. Shindell (2011), Global multi-year O₃-CO correlation patterns from models and TES satellite observations, *Atmos. Chem. Phys.*, 11(12), 5819–5838, doi:10.5194/acp-11-5819-2011.
- Wang, Y., A. W. DeSilva, G. C. Goldenbaum, and R. R. Dickerson (1998), Nitric oxide production by simulated lightning: Dependence on current, energy, and pressure, *Journal of Geophysical Research: Atmospheres*, 103(D15), 19,149–19,159, doi:10.1029/98JD01356.

- Wang, Y., Y. Zhang, J. Hao, and M. Luo (2011), Seasonal and spatial variability of surface ozone over China: contributions from background and domestic pollution, *Atmos. Chem. Phys.*, 11(7), 3511–3525, doi:10.5194/acp-11-3511-2011.
- Weinstock, E. M., et al. (2007), Quantifying the impact of the North American monsoon and deep midlatitude convection on the subtropical lowermost stratosphere using in situ measurements, *J. Geophys. Res.*, 112(D18).
- Wiesmann, H. J., and H. R. Zeller (1986), A fractal model of dielectric breakdown and prebreakdown in solid dielectrics, *Journal of Applied Physics*, 60(5), 1770–1773, doi:10.1063/1.337219.
- Williams, E. R. (1985), Large-Scale Charge Separation in Thunderclouds, *J. Geophys. Res.*, 90(D4), 6013–6025.
- Williams, E. R. (1989), The Tripole Structure of Thunderstorms, *J. Geophys. Res.*, 94(D11), 13,151–13,167, doi:10.1029/JD094iD11p13151.
- Wilson, C. T. R. (1916), On Some Determinations of the Sign and Magnitude of Electric Discharges in Lightning Flashes, *Royal Society of London Proceedings Series A*, 92, 555–574, doi:10.1098/rspa.1916.0040.
- Wong, J., M. C. Barth, and D. Noone (2013), Evaluating a lightning parameterization based on cloud-top height for mesoscale numerical model simulations, *Geosci. Model Dev.*, 6(2), 429–443, doi:10.5194/gmd-6-429-2013.
- Worden, J., et al. (2009), Observed vertical distribution of tropospheric ozone during the Asian summertime monsoon, *Journal of Geophysical Research: Atmospheres*, 114(D13), D13,304, doi:10.1029/2008JD010560.
- Yoshida, S., T. Morimoto, T. Ushio, and Z. Kawasaki (2009), A fifth-power relationship for lightning activity from Tropical Rainfall Measuring Mission satellite observations, *J. Geophys. Res.*, 114(D9), doi:10.1029/2008JD010370.
- Zeldovich, I. A. B. (1966), *Physics of Shock Waves and High-temperature Hydrodynamic Phenomena*, Dover Publications, Incorporated.
- Zhang, L., et al. (2006), Ozone-CO correlations determined by the TES satellite instrument in continental outflow regions, *Geophysical Research Letters*, 33(18), L18,804, doi:10.1029/2006GL026399.
- Zhang, L., D. J. Jacob, X. Liu, J. A. Logan, K. Chance, A. Eldering, and B. R. Bojkov (2010), Intercomparison methods for satellite measurements of atmospheric composition: application to tropospheric ozone from TES and OMI, *Atmos. Chem. Phys.*, 10(10), 4725–4739, doi:10.5194/acp-10-4725-2010.
- Zhang, X., J. Helsdon, John H., and R. D. Farley (2003), Numerical modeling of lightning-produced NO_x using an explicit lightning scheme: 1. Two-dimensional simulation as a “proof of concept”, *J. Geophys. Res.*, 108(D18).
- Zhao, C., Y. Wang, Y. Choi, and T. Zeng (2009), Summertime impact of convective transport and lightning NO_x production over North America: modeling dependence on meteorological simulations, *Atmos. Chem. Phys.*, 9(13), 4315–4327, doi:10.5194/acp-9-4315-2009.

Appendix A

Acronyms and Abbreviations

AHPS	Advanced Hydrological Prediction Service
AMF	air mass factor
ANOx	Anthropogenic nitrogen oxides
BVOCs	biogenic volatile organic compounds
CAPE	convective available potential energy
CCN	cloud condensation nuclei
CFCs	Chlorofluorocarbons
CLDN	Canadian Lightning Detection Network
CONUS	Contiguous United States
CTM	chemical-transport model
DE	detection efficiency
DF	direction finding (lightning detection)
DFS	degrees of freedom of signal
DOAS	Differential Optical Absorption Spectroscopy
ECC	electrochemical concentration cell
ECMWF	European Centre for Medium-Range Weather Forecasts model
ENTLN	Earth Networks Total Lightning Network
ENVISAT	Environmental Satellite
EOS	Earth Observing System

EPA	Environmental Protection Agency
ERS-2	European Remote-Sensing satellite
ESRL	Earth System Research Laboratory
FLEXPART	a Lagrangian particle dispersion model
FTUV	fast Tropospheric Ultraviolet-Visible
GFS	Global Forecast System
GOME	Global Ozone Monitoring Experiment
HCFCs	Hydrochlorofluorocarbons
HFCs	Hydrofluorocarbons
IC:CG	Intro-cloud:Cloud-to-ground
IMPACT	Improved Accuracy through Combined Technology (lightning detection)
INTEX-B	Intercontinental Chemical Transport Experiment - phase B
IONS-06	INTEX-B Ozonesonde Network Study of 2006
IPCC	Intergovernmental Panel on Climate Change
ISCCP	International Satellite Cloud Climatology Project
IWP	ice water path
JPL	Jet Propulsion Laboratory
KNMI	Royal Netherlands Meteorological Institute (Koninklijk Nederlands Meteorologisch Instituut)
KPP	Kinetic Pre-processor
LAI	leaf area index
LIS	Lightning Imaging Sensor
LNB	level of neutral buoyancy
LNOx	Lightning-generated nitrogen oxides
LPATS	Lightning Position and Tracking System
MAP	maximum a posteriori
MEGAN	Model of Emissions of Gases and Aerosols from Nature

MOPITT	Measurements Of Pollution In The Troposphere
MPE	Multi-sensor Precipitation Estimator
NALDN	North American Lightning Detection Network
NAM	North American Monsoon
NASA	National Aeronautics and Space Administration
NCAR	National Center for Atmospheric Research
NCEP	National Center for Environmental Prediction
NDSC	Network for the Detection of Stratospheric Change
NEI	National Emission Inventory
NLDN	National Lightning Detection Network
NOAA	National Oceanic and Atmospheric Administration
NO_x	nitrogen oxides ($\equiv\text{NO}+\text{NO}_2$)
NWS	National Weather Service
OMI	Ozone Monitoring Instrument satellite
OTD	Optical Transient Detector
PBL	planetary boundary layer
PCA	principal component analysis
PCEEA	parameterized canopy enviornmet emission activity
PM_{2.5}	particulate matter < 2.5 microns in diameter
PPFD	photosynthetic photon flux density
PR92	<i>Price and Rind</i> (1992)
PR93	<i>Price and Rind</i> (1993)
PR94	<i>Price and Rind</i> (1994)
RADM2	second-generation Regional Acid Deposition Model
RFC	River Forecast Center
SCIAMACHY	SCanning Imaging Absorption SpectroMeter for Atmospheric CHartographY
TEMIS	Tropospheric Emission Monitoring Internet Service

TES	Tropospheric Emission Spectrometer
TOA	time-of-arrival
TRMM	Tropical Rainfall Measuring Mission
VCD	vertical column density
VOCs	volatile organic compounds
WLS	Weatherbug Lightning Sensor
WPS	WRF Preprocessing System
WRF	Weather Research and Forecasting model

Appendix B

WRF-Chem v3.4.1 Namelist

Option(s)	Value(s)	Comment
&time_control		
(start end)_year	2006	
(start end)_month	(07 08)	
(start end)_day	(01-31)	end_day = start_day + 1
(start end)_hour	06	Always start at 6 UTC
interval_seconds	21600	Boundary condition input intervals (6 hours)
history_interval	180	History output interval (3 hours)
frame_per_outfile	1	
restart	.true.	Only .false. for July 1
restart_interval	1440	Daily restart
&domains		
time_step	90 + 0/1	Time-step in seconds
e_we	180	West-east domain dimension
e_sn	120	South-north domain dimension
e_vert	51	Vertical domain dimension
dx,dy	36000	Grid size (m)
p_top_requested	1000	Model top pressure (Pa)
num_metgrid_levels	27	
num_metgrid_soil_levels	4	
grid_id	1	No nesting
eta_levels	1.0, 0.99381, : 0.00560, 0.0	51 non-uniform fixed vertical resolution
&physics		
mp_physics	8	“New” Thompson microphysics scheme
progn	0	No prognostic cloud droplet number
ra_lw_physics	1	Rapid Radiative Transfer Model (RRTM)
ra_sw_physics	2	Goddard two-stream shortwave scheme

radt	30	Minutes between radiative physics call
sf_sfclay_physics	1	Surface layer physics
sf_surface_physics	2	Noah Land Surface Model
bl_pbl_physics	1	Yonsei University (YSU) scheme
cu_physics	5	Grell-3D (G3) cumulus scheme
cudt	0	Call convective parameterization every time step
prec_acc_dt	180	Bucket for precipitation (min)
isfflx	1	Turn on sensible and latent surface heat flux
ifsnow	0	Turn off snow effect on optical depth
icloud	1	Turn on cloud
surface_input_source	1	WPS/geogrid default surface category
num_soil_layers	4	
sf_urban_physics	0	Turn off urban physics
maxiens	1	(not used?)
maxens, maxens2, maxens3	3, 3, 16	G3 ensemble dimensions
ensdim	144	G3 ensemble dimension
cu_rad_feedback	.true.	Cumulus radiative feedback
ishallow	1	Turn on shallow convection
cu_diag	1	Turn on cumulus diagnostics
&fdda		
grid_fdda	1	Turn on grid 4D data assimilation (GFDDA)
gfdda_inname	"wrffdda_d<domain>"	
gfdda_end_h	10000	End hour ("never")
gfdda_interval_m	360	Interval of GFDDA inputs
fgdt	0	Nudge every time step
if_no_pbl_nudging_(uv,t,q)	0,1,1	Only do nudging for wind in PBL.
(if,k)_zfac_uv	1,10	Limit nudging of wind to above level 10
if_zfac_(t q)	0	
guv, gt	0.0024	Nudging coefficients (s^{-1})
gq	9.26e-5	Nudging coefficient (s^{-1})
if_ramping	1	Ramp down nudging at the end of period
dtramp_min	60.0	Ramp down time (min)
io_form_gfdda	2	NetCDF format for GFDDA data
&dynamics		
rk_ord	3	Runge-Kutta 3rd order
w_damping	1	Damping for vertical velocity
diff_opt	1	Evaluates 2nd order diffusion term on coordinate surfaces
km_opt	4	Horizontal Smagorinsky first order closure
base_temp	290	Base-state temperature (K)
zdamp	5000	Damping depth (m) from model top
damp_opt	3	Rayleigh damping
dampcoef	0.2	Rayleigh damping coefficient (s^{-1})
non_hydrostatic	.true.	

*_adv_opt	2	Positive definite and monotonic advection for moist , scalar , chem , and tracer
time_step_sound	4	Number of sound steps per time step
h_(mon sca)_adv_order	5	Horizontal orders for momentum and scalar advects
v_(mon sca)_adv_order	3	Vertical orders for advects
tracer_opt	4	8 twin tracers + 2 lightning tracers
 &bdy_control		
spec_bdy_width	5	Number of rows for specified boundary value nudging
spec_zone	1	Specified zone
relax_zone	4	Relaxation zone
specified	.true.	Specified boundary condition
nested	.false.	
 &chem		
kemit	19	Number of levels in emission files
chem_opt	101	RADM2-KPP option, no aerosol
bioemdt	1.5	Update time (min) for biogenic emissions
chemdt	1.5	Update time (min) for chemistry
io_style_emissions	1	Two 12-hr emission files
emiss_inpt_opt	1	Speciate emission for RADM2/SORGAM
emiss_opt	2	RADM2-speciated anthropogenic emission
chem_in_opt	0	Use chemistry from wrfinput_d*
phot_opt	3	FTUV photolysis (see Appendix D.1)
photdt	30	Update time (min) for photolysis
(gas aer)_drydep_opt	1	Include dry deposition
bio_emiss_opt	3	MEGAN2 biogenic emission
(dust dmsemis seas)_opt	0	Turn off dust, DMS, and sea salt options
gas_(bc ic)_opt	1	Use BC and IC for gas species
aer_(bc ic)_opt	0	No BC and IC for aerosols
gaschem_onoff	1	Turn on gas-phase chemistry
(aer cld)chem)_onoff	0	Turn off aerosol and cloud chemistry
wetscov_onoff	0	Turn off wet scavenging
vertmix_onoff	1	Turn on vertical mixing
chem_conv_tr	1	Turn on convective transport for chemical species
biomass_burn_opt	0	No biomass burning
aer_ra_feedback	0	No aerosol radiative feedback
have_bcs_chem	.true.	
lightning_opt	101	Cloud-parameterized PR92.
lightning_start_seconds	900	
lightning_time_step	90	In seconds, i.e. every time step
N_IC	350	Moles of NO per flash (independent of IC or CG)
flash_factor	1.0	Master flash rate tuning factor
passive_ltng	1	Emit passive LNO _x twin tracers
chem_diag	1	Produce tendency diagnostics for 8 species

Appendix C

User documentation for LNO_x in WRF-Chem 3.5

This is a short guide for using the lightning flash rate and lightning-generated nitrogen oxides (LNO_x) parameterizations in WRF and WRF-Chem after version 3.5.0. Significant changes have been made since 3.4.1, primarily in refactoring the model to allow flash rate predictions without chemistry. Currently, only implementations for the *Price and Rind* (1992, hereafter PR92) schemes are released with modifications based on *Barth et al.* (2012) and *Wong et al.* (2013).

To turn on lightning flash rate parameterization in WRF, set the `physics` namelist option `lightning_option` to one of the following values:

<code>lightning_option</code>	Description
1 [†]	PR92 based on maximum w , redistributes flashes within dBZ > 20
2 [†]	PR92 based on 20 dBZ top, redistributes flashes within dBZ > 20
11*	PR92 based on level of neutral buoyancy from convective parameterization

1 [†]	PR92 based on maximum w , redistributes flashes within dBZ > 20
2 [†]	PR92 based on 20 dBZ top, redistributes flashes within dBZ > 20
11*	PR92 based on level of neutral buoyancy from convective parameterization

[†] For convection-resolved resolutions with microphysics turned on for reflectivity calculations.

* For convection-parameterized resolution using either GD or G3 `cu_physics` options. Adjusted by areal ratio relative to `dx`=36 km (*Wong et al.*, 2013), intended for use at $10 < dx < 50$ km.

Setting `lightning_option` will produce four new 2D arrays: `(ic|cg)_flash(count|rate)` with units number (per seconds), where `ic` and `cg` represent intra-cloud and cloud-to-ground respectively.

Set the `physics` namelist option `iccg_method` to control the IC:CG ratio:

iccg_method Description

- 0 Default method depending on `lightning_option`, currently all options use `iccg_method=2` by default.
- 1 Constant everywhere, set with namelist options `iccg_prescribed_(num|den)`[†], default is 0./1. (all CG).
- 2 Coarsely prescribed 1995–1999 NLDN/OTD climatology based on *Boccippio et al.* (2001).
- 3 Parameterization by *Price and Rind* (1993) based on cold-cloud depth.
- 4 Gridded input via arrays `iccg_in_(num|den)` from wrfinput for monthly mapped ratios. Points with 0/0 values use ratio defined by `iccg_prescribed_(num|den)`.

[†] This is a shorthand for “`iccg_prescribed_num` and `iccg_prescribed_den`.” Similar notation is used throughout this guide when namelist options or arrays have long but similar names.

To emit LNO_x, in the form of nitrogen oxide (NO), set the `chem` namelist option `lnox_opt` to one of the following values:

lnox_opt Description

- 1 Combined IC+CG single-mode vertical distributions (*Ott et al.*, 2010). Outputs passive tracer array `lnox_total`.
- 2 Separate IC, CG distributions after *DeCaria et al.* (2000). Outputs two passive tracer arrays `lnox_(ic|cg)`.

Additional namelist settings are available for more detailed controls of the parameterizations:

Namelist option	Description
<code>&physics</code>	
<code>lightning_dt</code>	Time interval (seconds) for calling lightning parameterization. Default uses model time step.
<code>lightning_start_seconds</code>	Start time for calling lightning parameterization. Recommends at least 10 minutes for spin-up.
<code>flashrate_factor</code>	Factor to adjust the predicted number of flashes. Recommends 1.0 for <code>lightning_option=11</code> between <code>dx=10</code> and 50 km. Manual tuning recommended for all other options independently for each nest.
<code>cellcount_method</code>	Method for counting storm cells. Used by CRM options (<code>lightning_options=1,2</code>). !! Note that this option used to take values 1, 2, and 3 in version 3.4.1. 0 = model determines method used. 1 = tile-wide, appropriate for large domains 2 = domain-wide, appropriate for single-storm domains
<code>cldtop_adjustment</code>	Adjustment from LNB in km. Used by <code>lightning_option=11</code> . Default is 0, but recommends -2 km.
<code>iccg_prescribed_(num den)</code>	User prescribed <u>numerator</u> and <u>denominator</u> for IC:CG ratio. Used by <code>iccg_method=1,4</code> . Defaults are 0.0/1.0
<code>&chem</code>	
<code>N_(IC CG)</code>	Moles of NO emitted per IC and CG flashes. For total LNO_x option (<code>lnox_opt=1</code>), a weighted average based on the calculated IC:CG ratio is used. Default is 500 moles. Recommends 300–500 moles.
<code>lnox_passive</code>	Set to <code>.true.</code> to emit passive tracers only.
<code>ltng_temp_(upper lower)</code>	Temperatures ($^{\circ}\text{C}$) of <code>upper</code> and <code>lower</code> peaks of LNO_x vertical distributions (used by <code>lnox_opt=2</code>).

Appendix D

WRF-Chem bug fixes

Numerous bugs in WRF-Chem surfaced recently and caused the model to crash or produce undesirable results. This appendix details the bugs discovered and their corresponding fixes.

D.1 Fast TUV

The fast Tropospheric Ultraviolet-Visible (fast TUV, or FTUV) photolysis scheme is a simplified version of the widely used TUV scheme by *Madronich* (1987). Details of FTUV parameterization of TUV can be found in *Tie et al.* (2003). Since the use of MOZART chemistry options triggers an alternative method for computing model top ozone column, this bug only concerns WRF-Chem simulations using non-MOZART chemistry options.

D.1.1 Bug description

To simulate the radiative transfer of the full atmosphere, model column ozone is supplemented with exo-model ozone column density, or “exocolden.” This is done during the call to the subroutine `photo_inti` within `ftuv_init`. One of the intended functions of `photo_inti` is to add exocolden data every 2 km on top of the model top up to 50 km using reference data (`o3ref`). However, the model top input for this function has been hard-coded to 20 km regardless of the actual model top level height. The model set-up used in this study has a model top of 10 hPa, or ~ 30 km. Therefore, the effect height profile becomes $0, \dots, 30, 22, 24, 26, \dots, 48, 50$ km plus 2.9745×10^{16} molecules cm $^{-2}$ above 50 km. Furthermore, before the calculation of slant column density, the total column ozone

is also scaled to a fixed value (265 DU). However, this value is grossly under-representing the standard ozone column for the United States, which has a recommended value of 349 DU instead (*S. Madronich*, personal communication, 2013). These bugs have two primary consequences¹ :

- (1) Since ozone is typically highest between 20–30 km, two ozone maxima are introduced, one located outside the model physical levels. Because of an extra ozone maximum above model top, older simulations with a similar model top (30 km) may see significantly lower photolysis rates above 20 km.
- (2) When calculating the slant column density, the logarithm of `o2col` (depends on `dz`) is calculated in the subroutine `schu`. This effectively produces a NaN (Not-a-Number) at the model top when the heights drop from 30 km back down to 20 km. This is later used to index a look-up table. Since no index is initialized for the model top due to NaN value, it may either crash the model or produce unpredictable result depending on what the pre-existing value in the corresponding memory location was. Older runs may see missing photolysis rates at their model tops as a result.

D.1.2 Changes made

The model top input for `photo_inti` has now been changed to 30 km, the mean cloud top for the model setup used in this study. The ozone column scaling has also been changed to 349 DU. Due to an overall low bias in stratospheric ozone in WRF-Chem, the ozone profile between 20–30 km (model levels) internal of FTUV has also been replaced by that from `o3ref`. With these changes, the FTUV-TUV comparison² is shown in Table D.1 for

Table D.1: Comparison of photolysis rates from FTUV and TUV.

z (km)	(FTUV-TUV)/TUV	
	$J(O_3)$	$J(NO_2)$
0	+2.74%	-11.8%
2	+4.51%	-9.88%
5	+10.5%	-9.63%
7	+13.7%	-5.47%
10	+14.9%	-3.00%
20	-8.64%	-1.39%
29	-7.68%	-1.90%

¹ The expected low bias caused by the 265 DU is largely offset by the larger distribution of ozone above the model top due to the extra 20–30 km layer.

² The TUV code used here is an independent utility developed and implemented by Dr. Sasha Madronich at NCAR-ACD.

clear-sky condition with a solar zenith angle of 8.428° with a surface albedo of 10%. The remaining biases may be attributed to differences in actual ozone profiles used between WRF-Chem FTUV and the TUV code. It should also be noted that $J(\text{NO}_2)$ has slightly different cross-section in the two implementations, so differences are expected.

D.1.3 Other problems

- (1) Diagnostic outputs recently added (v3.4.0+) for photolysis spectral and rate information (`radfld`, `adjcoe`, `prate`) are copied through `nz`, which is the number of FTUV model levels including exocolden levels (59 in this study). However, these variables were only defined for `nref`(:= 51) levels. Thus for simulations where $\text{nz} > 51$, this statement is a guaranteed crash or out-of-bound access. This problem is patched for this study by removing the respective copy statements since the diagnostics are not used.
- (2) The surface albedo over sea water uses different data sets for MOZART and non-MOZART options. The concerning factor here is that the prescribed albedos is about an order of magnitude apart (e.g. 0.0747 for MOZART and 0.8228 for non-MOZART for the first spectral bin). Moreover, all grids are identified as land (`lu=1`) when non-MOZART options are used. No fix has been performed for this particular inconsistency due to lack of knowledge for the intention of the original programmer.
- (3) Photolysis cross sections and top-of-atmosphere solar flux have not been updated to more recent recommendations since FTUV's initial implementation in 2003. No direct changes have been made to these values, but constant scaling factors (α) have been applied to several photolysis reactions that have been shown to have significant biases during CALNEX 2010 flight measurements (*C. Knote*, personal communication, 2013). These reactions include $J(\text{HNO}_4)$ and $J(\text{MGLY}^3)$ with $\alpha = 0.35$ and 0.20 respectively.

³ Methylglyoxal, $\text{C}_3\text{H}_4\text{O}_2$

D.2 Passive tracer-convective transport

Passive tracer diagnostics have been added to WRF-Chem to facilitate air sourcing analyses from predefined sources. These tracers are held constant at 1.0 at their respective sourcing regions (e.g. stratosphere) or emitted by replicating a specified source (e.g. biomass burning, lightning). They are then allowed to be transported through advection and convection. However, because the original implementation of convective transport, performed by the subroutine `grelldrvct`, is designed to operate on the `chem` array, some changes have to be made.

D.2.1 Bug description

The subroutine handling downdraft (`cup_dd_tracer`) in version 3.4.1 iterates over the tracer array, but it uses the global value of `num_chem`, which is the number of chemical species. It works as designed for the `chem` array but since the `tracer` array is typically smaller, out-of-bound memory access occurs. This becomes problematic when the array `tr_pwd(:, :, :, num_chem)` is initialized at the beginning of `cup_dd_tracer`, which overwrites neighboring memory addresses with zeroes, including `ierr`, which identifies if convection has the necessary conditions to happen.

D.2.2 Changes made

An extra parameter is added to the definition of the subroutine `cup_dd_tracer` so that the proper array dimension is used for allocating the “tracer” array instead of the global value of `num_chem`, which is always associated with the `chem` array. Alternative naming convention has been suggested, but it will not be implemented until the next WRF-Chem update.

D.2.3 Other problems

- (1) The array `tr_dd` in the subroutine `CUP_ct`, which is accumulated in `cup_dd_tracer` through the column top-down, is not initialized properly. This bug is introduced in 3.4 when wet scavenging is added. Older runs may see tracers disappearing when convective transport

is used. It is now properly initialized to 0.0 in CUP_ct. For consistency, the same is done for `tr_up`.

- (2) Wet deposition for NO_3 and SO_4 are accumulated at the end of the main subroutine `grelldrvct`. However, since the same subroutine is used for convective transport for both `chem` and `tracer` arrays, wet deposition is effectively performed twice. Older runs may see higher ($2\times$) than expected wet deposition. This is fixed by testing for `chemopt` ($= 0$ if transporting tracer), this is not to be confused with `chem_opt`, which is the global chemistry option. Alternative naming convention has been suggested.